Aerosol-Cloud-Precipitation Interactions in Marine Stratocumulus Clouds

Thesis by
Yi-Chun Chen

In Partial Fulfillment of the Requirements for the degree
of
Doctor of Philosophy

CALIFORNIA INSTITUTE OF TECHNOLOGY
Pasadena, California
2013
(Defended 30 May, 2013)

To my parents, Li-Huei Chen and Ya-Ping Chuang.

ACKNOWLEDGEMENTS

First of all, I greatly thank my advisor, Prof. John Seinfeld, for offering me the opportunity to explore the fascinating aerosol-cloud interactions using various tools, from modeling, airborne based field observations, to satellite measurements. I thank him for all the guidance and for being so available for students. In addition, I appreciate his sharp perspectives and superb knowledge of science, as well as his patience when things did not work out as expected. I also thank my committee members, Simona Bordoni, Andy Ingersoll, Tapio Schneider, and Graeme Stephens, for their scientific feedback during these years.

The projects in this dissertation were carried out with tremendous assistance from many colleagues and peers. It is my great pleasure to collaborate with Dr. Graeme Stephens and Dr. Matt Christensen from JPL. I thank them for the time and effort of coming to Caltech for discussions with me on a regular basis. Their suggestions, excellent ideas, and knowledge on satellite data were extremely helpful. The two projects related to satellites could not be accomplished without them. Special thanks go to Matt Christensen for preparing the satellite data and answering my tons of questions. I must also thank Dr. Lulin Xue from NCAR for the assistance in running the large-eddy simulations and very helpful discussion on the analysis. I also thank him and NCAR for giving me the opportunity to be a visiting graduate student in the NCAR Advance Study Program (ASP). During the four months visiting NCAR in 2011, I was exposed to various fields of research, and my field of vision became broader. I also thank Dr. Roy Rasmussen, Prof. Armin Sorooshian, Dr. Hailong Wang, Dr. Frank Li, and Dr. Kentaro Suzuki for all the scientific comments and suggestions. Also, during my first year in Caltech, I worked with Prof. Yuk Yung and Dr. Danie Liang; I appreciate their instruction.

I would like to thank everyone in the Seinfeld research group. I received technical assistance from other modelers, and very much enjoyed the modelers' coffee time with them, including Wei-Ting Anne Chen, Andi Zuend, Zach Lebo, Joseph Ensberg, and Renee Mcvay. Also, I am grateful for the friendship during the field campaign with Jill Craven, Matt Coggon, and Andrew Metcalf. It was an awesome field campaign and I enjoyed our time doing research as well as having fun together. I thank Kate Schilling and Xuan Zhang for their friendship; it is great to share the research and life experiences with them. In addition, I appreciate the GPS computing staff, Naveed Near-Ansari and John Lilley, as well as secretaries, Elizabeth Miura Boyd and Yvette Grant, for all the trouble shooting and assistance.

The support from my undergraduate study at National Taiwan University meant a lot to me. I thank Prof. I-I Lin, Prof. Ho Lin, Prof. Jen-Ping Chen, and Prof. Chun-Chieh Wu for the caring and encouragement before and during my graduate study at Caltech. I thank my old friends Chia-Jung Pi, Yi-Hsuan Huang, Wei-Ting Fang, Eunice Jiang, and Grace Lee for the mentally support overseas.

Outside the research lab, I thank the members of the Association of Caltech Taiwanese for organizing various events, including softball games, volleyball games, and gatherings on special holidays. These enriched my life in Pasadena. I also appreciate my previous and current roommates Tiffany Wang and Pei Shih for the great company and friendship. They are the best roommates ever. I would like to give thanks to Kevin Yang for being my companion for over four years and I love the awesome dishes he made. His sense of humor makes daily life full of fun. Also, I sincerely appreciate my church friends for the constant support, both physically and spiritually.

Most importantly, I am extremely grateful for the everlasting love and support from my dear families in Taiwan. I thank my parents for all the caring, trust, and encouragement during these six years. I love chatting with my sister about life, work, interesting and sad things, etc. I am really happy that I did not miss her important moments in life – her wedding, as well as the birth of my lovely nephew. Yet I am sorrowful for my dear grandfather's death. I will remember his warm and gentle smile always. I would also like to give thanks to my brother, grandmother, aunts, uncles, and cousins for all their love.

ABSTRACT

Marine stratocumulus clouds are generally optically thick and shallow, exerting a net cooling influence on climate. Changes in atmospheric aerosol levels alter cloud microphysics (e.g., droplet size) and cloud macrophysics (e.g., liquid water path, cloud thickness), thereby affecting cloud albedo and Earth's radiative balance. To understand the aerosol-cloud-precipitation interactions and to explore the dynamical effects, three-dimensional large-eddy simulations (LES) with detailed bin-resolved microphysics are performed to explore the diurnal variation of marine stratocumulus clouds under different aerosol levels and environmental conditions. It is shown that the marine stratocumulus cloud albedo is sensitive to aerosol perturbation under clean background conditions, and to environmental conditions such as large-scale divergence rate and free tropospheric humidity.

Based on the in-situ Eastern Pacific Emitted Aerosol Cloud Experiment (E-PEACE) during Jul. and Aug. 2011, and A-Train satellite observation of 589 individual ship tracks during Jun. 2006-Dec. 2009, an analysis of cloud albedo responses in ship tracks is presented. It is found that the albedo response in ship tracks depends on the mesoscale cloud structure, the free tropospheric humidity, and cloud top height. Under closed cell structure (i.e., cloud cells ringed by a perimeter of clear air), with sufficiently dry air above cloud tops and/or higher cloud top heights, the cloud albedo can become lower in ship tracks. Based on the satellite data, nearly 25% of ship tracks exhibited a decreased albedo. The cloud macrophysical responses are crucial in determining both the strength and the sign of the cloud albedo response to aerosols.

To understand the aerosol indirect effects on global marine warm clouds, multisensory satellite observations, including CloudSat, MODIS, CALIPSO, AMSR-E, ECMWF, CERES, and NCEP, have been applied to study the sensitivity of cloud properties to aerosol levels and to large scale environmental conditions. With an estimate of anthropogenic aerosol fraction, the global aerosol indirect radiative forcing has been assessed.

As the coupling among aerosol, cloud, precipitation, and meteorological conditions in the marine boundary layer is complex, the integration of LES modeling, in-situ aircraft measurements, and global multisensory satellite data analyses improves our understanding of this complex system.

TABLE OF CONTENTS

LIST OF TABLES

Number *Page*

LIST OF FIGURES

Number *Page*

Chapter 1

Introduction and Motivation

Aerosols influence the microphysical properties of clouds and hence affect their radiative properties, amount and lifetime (IPCC, 2007). This influence, termed the aerosol indirect effect on climate, is identified as one of the major uncertainties in a quantitative assessment of the anthropogenic radiative forcing of climate. Marine stratocumulus clouds (MSc) play a significant role in the Earth's radiation budget. Covering about one-third of the world's oceans (Warren et al., 1988), MSc are particularly susceptible to the effect of aerosol perturbations. These clouds are generally optically thick and exist at a low altitude, making them more effective at reflecting solar radiation (albedo is about 30–40%, Randall et al., 1984) than at trapping terrestrial radiation. It has been estimated that a 6% increase of the albedo in MSc regions (equivalent to about a 0.2 g kg^{-1} moistening of the marine boundary layer (MBL), or an increase in cloud droplet number concentration N_d from 75 to 150 cm^{-3}) could result in a 1 W m^{-2} change in the net solar radiation at the top of the atmosphere (Stevens and Brenguier, 2009).

The complex interactions of the cloud system involve aerosol and cloud microphysics, atmospheric dynamics, radiation, and chemistry. A number of effects of aerosol perturbations on cloud LWP, cloud lifetime, and precipitation have been predicted by numerical studies and, in some cases, identified by measurements. Overall, the causality that has been proposed for aerosol-cloud-precipitation interactions can be summarized as follows:

(a) Twomey effect (assumes constant LWP): aerosol number concentration (N_a) increase → smaller, more numerous droplets → higher albedo (Twomey, 1977)

(b) Albrecht effect (drizzling cloud): N_a increase → smaller, more numerous droplets → reduced collision-coalescence → less precipitation → LWP increase → higher albedo (Albrecht et al., 1989)

(c) Drizzle-entrainment effect (drizzling cloud): N_a increase → smaller, more numerous droplets → reduced collision-coalescence → less precipitation → reduced below-cloud evaporative cooling and in-cloud latent heat release → higher turbulent kinetic energy (TKE) → stronger entrainment → LWP decrease → lower albedo (e.g., Lu and Seinfeld, 2005; Wood, 2007)

(d) Sedimentation-entrainment effect (non-drizzling cloud): N_a increase → smaller, more numerous droplets → reduced in-cloud sedimentation → increase of cloud water and evaporation in entrainment regions → stronger entrainment → LWP decrease → lower albedo (Ackerman et al., 2004; Bretherton et al., 2007; Hill et al., 2009)

(e) Evaporation-entrainment effect (non-drizzling cloud): N_a increase → smaller, more numerous droplets → more efficient evaporation → higher TKE stronger entrainment → LWP decrease → lower albedo (Wang et al., 2003; Xue and Feingold, 2006; Hill et al., 2008)

Drizzle formation leads to release of latent heat in the cloud and to stabilization of the sub-cloud layer through evaporative cooling and moistening. Thus the existence of drizzle reduces the buoyancy, stabilizes the MBL, decreases the TKE, and reduces the entrainment strength. As a result, precipitation suppression due to increased N_a increases the buoyancy fluxes and TKE, destabilizes the MBL, and enhances the cloud-top entrainment (as shown in pathway (c)) (e.g., Stevens et al., 1998; Ackerman et al., 2004; Lu and Seinfeld, 2005; Wood, 2007).

Aerosol-cloud interactions in non-drizzling MSc can be influenced by two kinds of entrainment effects (Hill et al., 2009): (d) Sedimentation-entrainment effect: increasing N_a in nondrizzling MSc reduces in-cloud sedimentation, and thus increases the cloud liquid water content and evaporation in the entrainment region, leading to stronger entrainment and LWP reduction (Bretherton et al., 2007); (e) Evaporation-entrainment effect: increase in N_a results in smaller, more numerous cloud droplets, and thus stronger evaporation, which enhances in-cloud turbulence and cloud-top entrainment. The entrained warm, dry air leads to cloud thinning and LWP reduction (Wang et al. 2003; Xue and Feingold 2006). For both effects an increase in N_a leads to LWP reduction, counteracting (b).

The common premise that clouds and precipitation are strongly sensitive to aerosol perturbations neglects the mechanisms that buffer the effects of aerosol perturbations (Stevens and Feingold, 2009). As both aerosol and meteorology (i.e., large-scale dynamic and thermodynamic state) govern the cloudiness, the intertwining of these two factors complicates the interpretation of data (Stevens and Brenguier, 2009).

To represent both MSc microphysics and dynamics, large-eddy simulations (LES) have become a powerful tool because of the ability to realistically represent the larger eddy turbulence field and the interactions of turbulence, cloud microphysics and radiation at an appropriate grid resolution. In order to obtain a comprehensive view of these interactions, high-resolution LES simulations are carried out in Chapter 2 of this thesis. The aerosol-cloud responses under different meteorological factors (include SST, free-tropospheric humidity, large scale subsidence rate, and wind speed) are investigated.

Based on the assumption that increasing aerosol number concentration leads to higher cloud droplet number concentration and an increase in cloud albedo, a marine geo-engineering scheme was proposed (Salter et al., 2008): using wind-driven spray-vessels that pump sub-micrometer sea-salt particles into the air beneath MSc. However, cloud macrophysical responses to increased aerosol levels can lead to either enhancement or diminution of cloud brightening. One of the challenges in understanding the cloud macrophysical responses lies in untangling the aerosol effects from others such as meteorological conditions. In Chapter 3, by utilizing both in situ aircraft measurements E-PEACE (Eastern Pacific Emitted Aerosol Cloud Experiment) and A-Train satellite data, we present an analysis of the factors that control the sign and magnitude of the aerosol indirect effect in ship tracks.

After applying LES study and ship track observations to investigate the aerosol-cloud relationships in regional scale, it is of great interest to understand whether these responses have a global impact. In Chapter 4, to understand the aerosol indirect effects on global marine warm clouds, multisensory satellite observations, including CloudSat, MODIS, CALIPSO, AMSR-E, ECMWF, CERES, and NCEP, have been applied to study the sensitivity of cloud properties to aerosol levels and to large scale environmental conditions. Over the world's oceans for the period August 2006 to December 2009, over 130 million pixels are comprised, of which ~ 3.7 million pixels pass screening for single-layer marine warm clouds. With an estimate of anthropogenic aerosol fraction, the global aerosol indirect radiative forcing has been assessed.

As the coupling among aerosol, cloud, precipitation, and meteorological conditions in the marine boundary layer is complex, the integration of LES modeling, in-situ aircraft

measurements, and global multisensory satellite data analyses improves our understanding of this complex system.

Bibliography

Ackerman, A. S., Kirkpatrick, M. P., Stevens, D. E., and Toon, O. B.: The impact of humidity above stratiform clouds on indirect aerosol climate forcing, Nature, 432, 1014-1017, 2004.

Albrecht, B.: Aerosols, cloud microphysics, and fractional cloudiness, Science, 245, 1227-1230, 1989.

Bretherton, C. S., Blossey, P. N., and Uchida, J.: Cloud droplet sedimentation, entrainment efficiency, and subtropical stratocumulus albedo. Geophys. Res. Lett., 34, L03813, doi:10.1029/2006GL027648, 2007.

Hill, A. A., Dobbie, S., and Yin, Y.: The impact of aerosols on non-precipitating marine stratocumulus: Part 1. Model description and prediction of the indirect effect, Q. J. Roy. Meteor. Soc., 134, 1143-1154, 2008.

Hill, A. A., Feingold, G., and Jiang, H.: The influence of entrainment and mixing assumption on aerosol-cloud interactions in marine stratocumulus, J. Atmos. Sci., 66, 1450-1464, 2009.

IPCC: Summary for policymakers, in: Climate Change 2007: The Physical Science Basis, Contribution of Working Group I to the Fourth Assessment Report of the Intergovernmental Panel on Climate Change, edited by: Solomon, S., Qin, D., Manning, M., Chen, Z., Marquis, M., Averyt, K. B., Tignor, M., and Miller, H. L., Cambridge University Press, 2007.

Lu, M.-L. and Seinfeld, J. H.: Study of the aerosol indirect effect by Large-Eddy Simulation of marine stratocumulus, J. Atmos. Sci., 62, 3909-3932, 2005.

Randall, D. A.: Stratocumulus cloud deepening through entrainment, Tellus, 36, 446–457, 1984.

Salter, S., Sortino, G., and Latham, J.: Sea-going hardware for the cloud albedo method of reversing global warming, Philos. Trans. Roy. Soc. London, 366, 3989–4006, doi:10.1098/rsta.2008.0136, 2008.

Stevens, B., Cotton, W. R., Feingold, G., and Moeng, C.-H.: Large-eddy simulations of strongly precipitating, shallow, stratocumulus-toped boundary layers, J. Atmos. Sci., 55, 3616-3638, 1998.

Stevens, B. and Brenguier, J.-L.: Cloud controlling factors: low clouds. Clouds in the perturbed climate system, Heintzenberg, J. and Charlson, R. J., The MIT Press, Cambridge, Massachusetts, 173-196, 2009.

Stevens, B. and Feingold, G.: Untangling aerosol effects on clouds and precipitation in a buffered system, Nature, 461, 607-613, 2009.

Twomey, S.: The influence of pollution on the shortwave albedo of clouds, J. Atmos. Sci., 34, 1149-1152, 1977.

Wang, S., Wang, Q., and Feingold, G.: Turbulence, condensation, and liquid water transport in numerically simulated nonprecipitating stratocumulus clouds. J. Atmos. Sci., 60, 262-278, 2003.

Warren, S. G., Hahn, C. J., London, J., Chervin, R. M., and Jenne, R. L.: Global distribution of total cloud cover and cloud type amounts over the ocean. NCAR Tech. Note NCAR/TN-317+STR, 42 pp., 1988.

Wood, R.: Cancellation of aerosol indirect effects in marine stratocumulus through cloud thinning, J. Atmos. Sci., 64, 2657-2669, 2007.

Xue, H., and Feingold, G.: Large-eddy simulations of trade wind cumuli: Investigation of aerosol indirect effects. J. Atmos. Sci., 63, 1605-1622, 2006.

Chapter 2

Large Eddy Simulation

on Marine Stratocumulus Clouds

Published in *Atmospheric Chemistry and Physics*: Chen, Y.-C., Xue, L., Lebo, Z. J., Wang, H., Rasmussen, R. M., and Seinfeld, J. H.: A comprehensive numerical study of aerosol-cloud-precipitation interactions in marine stratocumulus, Atmos. Chem. Phys., 11, 9749–9769, doi:10.5194/acp-11-9749-2011, 2011.

2.1 Abstract

Three-dimensional large-eddy simulations (LES) with detailed bin-resolved microphysics are performed to explore the diurnal variation of marine stratocumulus (MSc) clouds under clean and polluted conditions. The sensitivity of the aerosol-cloud-precipitation interactions to variation of sea surface temperature, free tropospheric humidity, large scale divergence rate, and wind speed is assessed. The comprehensive set of simulations corroborates previous studies that (1) with moderate/heavy drizzle, an increase in aerosol leads to an increase in cloud thickness; and (2) with non/light drizzle, an increase in aerosol results in a thinner cloud, due to the pronounced effect on entrainment. It is shown that for higher SST, stronger large-scale divergence, drier free troposphere, or lower wind speed, the cloud thins and precipitation decreases. The sign and magnitude of the Twomey effect, droplet dispersion effect, cloud thickness effect, and cloud optical depth susceptibility to aerosol perturbations (i.e., change in cloud optical depth to change in aerosol number concentration) are evaluated by LES experiments and compared with analytical formulations. The Twomey effect emerges as dominant in total cloud optical depth susceptibility to aerosol perturbations. The dispersion effect, that of aerosol perturbations on the cloud droplet size spectrum, is positive (i.e., increase in aerosol leads to spectral narrowing) and accounts for 3% to 10% of the total cloud optical depth susceptibility at nighttime, with greater influence in heavier drizzling clouds. The cloud thickness effect is negative (i.e., increase in aerosol leads to thinner cloud) for non/light drizzling cloud and positive for a moderate/heavy drizzling clouds; the cloud thickness effect contributes 5% to 22% of the nighttime total cloud susceptibility. Overall, the total cloud optical depth susceptibility ranges from ~0.28 to 0.53 at night; an increase in aerosol concentration enhances cloud optical depth, especially with heavier precipitation and in a more pristine environment. During the daytime, the range of magnitude for each effect is more variable owing to cloud thinning and decoupling. The good agreement between LES experiments and analytical formulations suggests that the latter may be useful in evaluations of the total cloud susceptibility. The ratio of the magnitude of the cloud thickness effect to that of the Twomey effect depends on cloud base height and cloud thickness in unperturbed (clean) clouds.

2.2 Introduction

Aerosols influence the microphysical properties of clouds and hence affect their radiative properties, amount and lifetime (IPCC, 2007). This influence, termed the aerosol indirect effect on climate, is identified as one of the major uncertainties in a quantitative assessment of the anthropogenic radiative forcing of climate. Marine stratocumulus clouds (MSc) play a significant role in the Earth's radiation budget. Covering about one-third of the world's oceans (Warren et al., 1988), MSc are particularly susceptible to the effect of aerosol perturbations. These clouds are generally optically thick and exist at a low altitude, making them more effective at reflecting solar radiation (albedo is about 30–40%, Randall et al., 1984) than at trapping terrestrial radiation. It has been estimated that a 6% increase of the albedo in MSc regions (equivalent to about a 0.2 g kg-1 moistening of the marine boundary layer (MBL), or an increase in cloud droplet number concentration N_d from 75 to 150 cm^{-3}) could result in a 1 W m^{-2} change in the net solar radiation at the top of the atmosphere (Stevens and Brenguier, 2009).

The complex interactions of the cloud system involve aerosol and cloud microphysics, atmospheric dynamics, radiation, and chemistry. The dynamics of MSc have been the subject of numerous modeling studies. Mixed-layer models (MLMs, Lilly, 1968) couple cloud, radiation, and turbulence to describe the cloud-topped marine boundary layer (MBL) (e.g., Turton and Nicholls, 1987; Bretherton and Wyant, 1997; Lilly, 2002; Wood, 2007; Sandu et al., 2009; Caldwell and Bretherton, 2009a; Uchida et al., 2010). Given surface and free-tropospheric thermodynamic conditions, bulk cloud properties, such as thickness, cloud liquid water path (LWP), and the MBL steady-state, can be determined by an MLM. The MLM framework represents a well-mixed MBL. Departures from well-mixed conditions are, however, common in situations of precipitation and during daytime.

To represent both MSc microphysics and dynamics, large-eddy simulations (LES) have become a powerful tool because of the ability to realistically represent the larger eddy turbulence field and the interactions of turbulence, cloud microphysics and radiation at an appropriate grid resolution. LES has been applied in many previous studies of MSc (e.g., Stevens et al., 1998; 2003; 2005; Stevens and Bretherton, 1999; Bretherton et al., 1999; Chlond and Wolkau, 2000; Jiang et al., 2002; Wang et al., 2003; Duynkerke et al., 2004; Lu

and Seinfeld, 2005, 2006; Bretherton et al., 2007; Sandu et al., 2008; Savic-jovcic and Stevens, 2008; Yamaguchi and Randall, 2008; Hill et al., 2008; 2009; Ackerman et al., 2009; Caldwell and Bretherton, 2009b; Wang and Feingold, 2009a,b; Wang et al., 2010; Uchida et al., 2010). Table 2.1 summarizes a number of studies that focus mainly on aerosol-cloud interactions in MSc; these address the LWP responses to changes in aerosol number and ambient environmental conditions, including sea surface temperature (SST), large scale divergence rate (D), and free tropospheric humidity (q_{ft}). Atmospheric aerosols and meteorology each exert controls on cloudiness; the former governs the cloud micro-structure, while the latter provides the dynamic and thermodynamic state that controls cloud macro-structure (Stevens and Brenguier, 2009).

A number of effects of aerosol perturbations on cloud LWP, cloud lifetime, and precipitation have been predicted by numerical studies and, in some cases, identified by measurements. Overall, the causality that has been proposed for aerosol-cloud-precipitation interactions can be summarized as follows:

(a) Twomey effect (assumes constant LWP): aerosol number concentration (N_a) increase → smaller, more numerous droplets → higher albedo (Twomey, 1977)

(b) Albrecht effect (drizzling cloud): N_a increase → smaller, more numerous droplets → reduced collision-coalescence → less precipitation → LWP increase à higher albedo (Albrecht et al., 1989)

(c) Drizzle-entrainment effect (drizzling cloud): N_a increase → smaller, more numerous droplets → reduced collision-coalescence → less precipitation → reduced below-cloud evaporative cooling and in-cloud latent heat release → higher turbulent kinetic energy (TKE) → stronger entrainment → LWP decrease → lower albedo (e.g., Lu and Seinfeld, 2005; Wood, 2007)

(d) Sedimentation-entrainment effect (non-drizzling cloud): N_a increase → smaller, more numerous droplets → reduced in-cloud sedimentation → increase of cloud water and evaporation in entrainment regions → stronger entrainment → LWP decrease → lower albedo (Ackerman et al., 2004; Bretherton et al., 2007; Hill et al., 2009)

(e) Evaporation-entrainment effect (non-drizzling cloud): N_a increase → smaller, more numerous droplets → more efficient evaporation → higher TKE stronger entrainment → LWP decrease → lower albedo (Wang et al., 2003; Xue and Feingold, 2006; Hill et al., 2008)

Drizzle formation leads to release of latent heat in the cloud and to stabilization of the sub-cloud layer through evaporative cooling and moistening. Thus the existence of drizzle reduces the buoyancy, stabilizes the MBL, decreases the TKE, and reduces the entrainment strength. As a result, precipitation suppression due to increased N_a increases the buoyancy fluxes and TKE, destabilizes the MBL, and enhances the cloud-top entrainment (as shown in pathway (c)) (e.g., Stevens et al., 1998; Ackerman et al., 2004; Lu and Seinfeld, 2005; Wood, 2007).

Aerosol-cloud interactions in non-drizzling MSc can be influenced by two kinds of entrainment effects (Hill et al., 2009): (d) Sedimentation-entrainment effect: increasing N_a in nondrizzling MSc reduces in-cloud sedimentation, and thus increases the cloud liquid water content and evaporation in the entrainment region, leading to stronger entrainment and LWP reduction (Bretherton et al., 2007); (e) Evaporation-entrainment effect: increase in N_a results in smaller, more numerous cloud droplets, and thus stronger evaporation, which enhances in-cloud turbulence and cloud-top entrainment. The entrained warm, dry air leads to cloud thinning and LWP reduction (Wang et al. 2003; Xue and Feingold 2006). For both effects an increase in N_a leads to LWP reduction, counteracting (b).

In simulations of MSc, Ackerman et al. (2004) showed that for moderate/heavy surface precipitation rates the LWP increases with N_d (following effect (b)). On the other hand, under non/light drizzling conditions the LWP decreases with increasing N_d (as explained by pathways (d) and (e)). Similar trends have also been found in other nocturnal studies (Table 2.1), in which opposite responses of LWP to an increase in N_a for heavy/moderate and light/non- drizzling conditions occur. The free troposphere moisture (q_{ft}) exerts a strong control on the precipitation rate through cloud-top entrainment, thus altering the balance between the competing effects of precipitation on LWP. The effects of the free tropospheric moisture can be summarized (Ackerman et al., 2004) as: (i) moist entrained air →does not

dry MBL effectively → cloud thickening, versus (ii) dry entrained air → dry the MBL □ cloud thinning. Similar results were also obtained by Sandu et al. (2008) for a diurnal cycle.

The effect of changes in the large scale divergence, D, is consistent among the studies listed in Table 2.1, showing that under higher (lower) D, the cloud top is driven down (higher), resulting in thinner (thicker) cloud, lower (higher) LWP. Since D is difficult to measure, its value is usually estimated.

The effect of changes in SST on MSc has been addressed in several studies. Lu and Seinfeld (2005) and Wood (2007) found that with higher SST, the MBL deepens and cloud base rises, resulting in a thinner cloud with lower LWP. In the LES study of Lu and Seinfeld (2005), the initial temperature in the entire MBL was assumed to increase systematically with SST, and the MBL relative humidity was adjusted as well; the MSc becomes less cloudy because of gradual dissipation. In the MLM study of Caldwell and Bretherton (2009a), however, as SST increases, the equilibrium cloud base and cloud top heights both increase due to increased entrainment through a weaker inversion, resulting in a thicker cloud with higher LWP. Therefore in response to a higher SST, shorter time scale and equilibrium responses have different effects on MSc.

Diurnal variation is the result of competition between cloud top longwave (LW) radiative cooling occurring both day and night, and daytime solar heating (Hill et al., 2008). During nighttime, cloud top LW cooling enhances TKE, couples the cloud and the surface fluxes, well mix the MBL, and the cloud tends to become thicker. While under daytime conditions, absorption of solar radiation offsets the cloud top LW cooling, stabilizing the MBL, causing the cloud to thin; some clouds may even become decoupled. Predicted daytime LWP is consistently smaller than that in nighttime (Table 2.1). Also, daytime MBL is less sensitive to changing N_a than under nighttime conditions (e.g., Ackerman et al., 2004; Lu and Seinfeld, 2005), suggesting cloud-radiation interactions are important in controlling the diurnal variation.

From a summary of the studies cited in Table 2.1, overall, non/light drizzling MSc and moderate/heavy drizzling MSc respond differently to changes in aerosol level since the dominant physical/dynamical mechanisms differ. Also, distinct diurnal responses are

shown in day and nighttime conditions as a result of cloud-radiation interactions. And MSc is found to be sensitive to changes in ambient conditions, e.g., SST, D, or q_{ft}.

Aerosol-cloud-precipitation interactions in MSc are tightly intertwined and often subtle. In order to obtain a comprehensive view of these interactions, high-resolution LES simulations are carried out in the present study. The meteorological factors investigated include SST, free-tropospheric humidity, large scale subsidence rate, and wind speed. Diurnal variation is considered as well as non/light drizzling and moderate/heavy drizzling MSc. We begin with an analytical formulation of cloud susceptibility to aerosol perturbation in terms of the Twomey, cloud droplet dispersion, cloud thickness, and diabaticity effects. The sign and magnitude of each effect are evaluated from LES simulations to compare with the analytical formulations. While each of the studies cited in Table 2.1 addresses one or more aspects of aerosol-MSc interactions, the present study is intended to be a comprehensive, consistent evaluation of these interactions covering the range of the important variables.

2.3 Cloud Susceptibility to Aerosol Perturbations

Before proceeding to the numerical study, it is useful to address MSc aerosol-cloud relationship from a simplified analytical point of view, providing a consistent basis on which to connect aerosol-cloud-precipitation interactions. Considering the change of cloud radiative properties in response to a change in aerosol number concentration, $N_{a,}$ the relationship between adiabatic cloud optical thickness τ_{ad} and adiabatic cloud droplet number concentration, N_{ad}, can be expressed (Brenguier et al., 2000):

$$\tau_{ad} = \frac{9}{10}\left(\frac{4}{3}\pi\right)^{1/3} {l_0}^{2/3} (k\, N_{ad})^{1/3}\; H^{5/3} \tag{2.1}$$

where $l_0 = \frac{C_w}{\rho_w}$, ρ_w is the density of water, C_w is the moist adiabatic condensation coefficient, k is a parameter related to the droplet spectrum shape, which is inversely proportional to the droplet distribution breadth, and H is cloud thickness. The range of k is 1 in the limit of a monodisperse size distribution and approaches 0 for a very wide distribution. In the presence of cloud top entrainment and water loss through precipitation, the cloud droplet profile tends to be diabatic. A sub-adiabaticity parameter f can be defined

to include the effects of entrainment and precipitation in drying out the cloud relative to the adiabatic case. Equation (2.1) can be generalized (W. Conant, personal communication) as

$$\tau = \frac{9}{10}\left(\frac{4}{3}\pi\right)^{1/3} {l_0}^{2/3} f^{(2+m)/3} (k\, N_{ad})^{1/3}\; H^{5/3} \tag{2.2}$$

where f is 1 under adiabatic conditions, and approaches 0 as the degree to which the profile is sub-adiabatic increases. The parameter m describes the microphysical impacts of mixing between the cloudy air and the relatively dry/warm free tropospheric air. m = 1 corresponds to the limit of inhomogeneous mixing, in which the turbulent mixing is relatively slow and all droplets in the entrained air evaporate, resulting in reduction of N_d and broadening of the droplet spectrum. m = 0 corresponds to the limit of homogeneous mixing, in which the timescale of turbulent mixing is much shorter than that at which droplets respond to the fresh ambient air. In this limit, all droplets experience the same degree of sub-saturation and evaporate together; thus N_d remains constant as all droplets shift to smaller sizes.

From equation (2.2), the impact of changes in aerosol number concentration on cloud optical depth (the cloud susceptibility) can be expressed as follows:

$$\frac{dln\tau}{dlnN_a} = \frac{1}{3}\left(\frac{dlnN_{ad}}{dlnN_a} + \frac{dlnk}{dlnN_a} + 5\frac{dlnH}{dlnN_a} + (2+m)\frac{dlnf}{dlnN_a}\right) \tag{2.3}$$

2.3.1 Twomey effect

From the above equation, $dlnN_{ad}/dlnN_a$ represents the so-called Twomey effect. An analytical relationship between N_{ad} and N_a, modified from that derived by Twomey (1959), is

$$N_{ad} = N_a^{\frac{2}{k_s+2}}\left[\frac{cw^{\frac{3}{2}}}{k_s B\left(\frac{k_s}{2},\frac{3}{2}\right)}\right]^{\frac{k_s}{k_s+2}} \tag{2.4}$$

where B is the beta function, w is updraft velocity at cloud base, k_s is a parameter related to the exponent in an assumed power-law aerosol size distribution, and c is a composition-

dependent parameter that relates the aerosol size distribution to the supersaturation spectrum. From equation (2.4),

$$\frac{dlnN_{ad}}{dlnN_a} = \frac{2}{k_s + 2} \tag{5}$$

Values of k_s range from 0.3 to 1.4 (empirical constants for cloud condensation nuclei, CCN, at 1 % supersaturation, from Pruppacher and Klett (1997)). For that range, $dlnN_{ad}/dlnN_a$ varies from about 0.6~0.9 under adiabatic conditions. Shao and Liu (2009) compared $dlnN_{ad}/dlnN_a$ predicted by equation (2.5) with in-situ measurements (values of 0.25~0.85). Differences in the value of $dlnN_{ad}/dlnN_a$ between the analytical expression and ambient measurements can be attributed to (i) activation effect: adding aerosols, for example, into a marine aerosol background reduces the ability of aerosols to act as CCN, and (ii) adiabaticity influence: the variability of the adiabaticity (cloud dilution state) from different meteorological conditions between clean and polluted clouds.

2.3.2 Dispersion effect

The second term $dlnk/dlnN_a$ expresses the effect of changes in N_a on the cloud droplet size distribution. Dispersion in the droplet distribution is related to aerosol composition (e.g., Feingold and Chuang, 2002), microphysics (e.g., collision-coalescence), and dynamics (e.g., entrainment mixing, updraft velocity) (Wood et al., 2002; Lu and Seinfeld, 2006). It is noted from observational data (Martin et al., 1994; Ackerman et al., 2000; Liu and Daum, 2002) that the dispersion forcing would lead to an indirect warming effect, opposing the Twomey effect. Accounting for the parameterization of dispersion effect in GCMs leads to a reduction in the magnitude of the predicted Twomey effect (Rotstayn and Liu, 2003, 2009). By contrast, an opposite trend is found in the LES study of Lu and Seinfeld (2006). For a drizzling cloud, increasing N_a leads to spectrum narrowing (larger k) because smaller droplets suppress precipitation formation by limiting the collision-coalescence process and enhance droplet condensational growth in the presence of higher updraft velocities, due to stronger TKE (Lu and Seinfeld, 2006). In that case, the dispersion effect enhances the Twomey effect. This trend is evident in in-situ measurements by Miles et al. (2000) and individual ship tracks in Lu et al. (2007).

2.3.3 Cloud thickness effect

The third term in equation (2.3), $dlnH/dlnN_a$, expresses the sensitivity of cloud thickness to changes in N_a, for which Wood (2007) derived an analytical formulation and applied a MLM to quantify the response of cloud thickness to perturbed N_d under different environmental conditions. Wood (2007) showed that the MSc cloud thickness response is determined by a balance between the moistening/cooling of the MBL resulting from precipitation suppression and drying/warming resulting from enhanced entrainment due to increased TKE. The drying and warming effect (cloud thinning) counteracts the moistening/cooling effect (cloud thickening). Also using the MLM model, Pincus and Baker (1994) predicted that cloud thickness (H) increases with N_d, especially at lower droplet concentration. Unlike the Pincus and Baker (1994) result that H is determined primarily by cloud top height, Wood (2007) found the cloud base height to be the single most important determinant in affecting cloud thickness. If the cloud base height is lower (higher) than 400 m, increasing N_d leads to cloud thickening (thinning), which corresponds to LWP increase (decrease). The argument is that for an elevated cloud base, more evaporation occurs before precipitation reaches the surface, leading to two effects (Wood, 2007): (i) more sub-cloud evaporation limits the moistening/cooling of the MBL resulting from precipitation suppression, while allowing suppressed precipitation to increase the entrainment with increasing N_d, and (ii) sub-cloud evaporation has a stronger effect on turbulence than in-cloud latent heating; therefore enhanced sub-cloud evaporation increases the leverage of changes in cloud base precipitation on entrainment.

2.3.4 Adiabaticity effect

The term, $dlnf/dlnN_a$, can be termed the diabaticity effect, accounting for the effect of liquid water depletion due to entrainment mixing and precipitation on cloud optical depth. This term cannot be evaluated separately from the other terms; the effect of diabaticity is intertwined with all the previous effects discussed. The qualitative effect of entrainment mixing on cloud behavior has been discussed in Section 1 (effects (c), (d), and (e)).

Some of these individual effects have been estimated in several previous studies (Table 2.2), including analytical solutions, in-situ measurements, satellite data, and LES. We will subsequently estimate the magnitudes for each effect from LES simulation.

2.4 Model Description

2.4.1 Numerical model

In this study we employ the Weather Research and Forecasting (WRF) model V3.1.1 as a 3D LES model. A detailed bin-resolved microphysical scheme (Geresdi, 1998; Rasmussen et al., 2002; Xue et al., 2010) is employed. In the bin microphysical scheme, aerosol number, cloud drop mass, and cloud drop number are computed over a size-resolved spectrum, predicting both cloud drop mass and number concentration following the moment-conserving technique (Tzivion et al., 1987, 1989; Reisin et al., 1996). Cloud drops are divided into 36 size bins with radii ranging from 1.56 μm to 6.4 mm and with mass doubling between bin. The masses for the first bin and the 36th bin are 1.5979×10^{-14} and 1.098×10^{-3} kg, respectively. In this study, the cutoff radius between cloud drop and rain drop size is taken to be 40 μm. The aerosols are divided into 40 size bins between 0.006 to 66.2 μm.

2.4.2 Microphysical processes

The microphysical processes include aerosol activation, drop condensation/evaporation, collision-coalescence, collisional breakup, and sedimentation. The aerosol size distribution is taken to be a single mode lognormal size distribution. Aerosol activation (or cloud droplet activation) occurs when the ambient supersaturation exceeds the critical supersaturation (S_c) for the given particle size. A hygroscopicity parameter κ, which describes the relationship between dry particle diameter and cloud condensation nuclei activity, is used to represent the composition-dependence of the solution water activity (Petters and Kreidenweis, 2006),

$$S_c(D) = \frac{D^3 - D_d^3}{D^3 - D_d^3(1-\kappa)} \exp\left(\frac{4\sigma_{\frac{s}{a}} M_w}{RT\rho_w D}\right) - 1 \tag{2.6}$$

where D is droplet diameter, D_d is aerosol dry diameter, σ is the surface tension of the solution/air interface, M_w is the molecular weight of water, and ρ_w is the density of water. For the present study, the aerosol is assumed to be ammonium sulfate, for which κ is set to the constant value 0.615 (Petters and Kreidenweis, 2006).

The aerosol number concentration is held constant in the present study. Thus we neglect below-cloud precipitation scavenging of aerosol. The activated droplet number at each time is calculated by the difference between the particle number that would be activated at the diagnosed supersaturation and the pre-existing droplet number. Diffusional growth and evaporation of water drops are described following the vapor diffusion equation (Pruppacher and Klett, 1997). The Best and Bond number approach is used to calculate the terminal velocity of water drops (Pruppacher and Klett, 1997). The efficiencies of collision-coalescence between drops are derived using the data of Hall (1980) to calculate the kernel function. The collisional breakup of water drops is included following Feingold et al. (1988).

2.4.3 Other processes

Surface latent and sensible heat fluxes are calculated from local wind speed and the difference in specific humidity/temperature between the ocean and the air just above the ocean surface, following the Monin-Obukhov scheme. A 3D turbulence scheme with 1.5-order turbulent kinetic energy (TKE) closure (Deardorff, 1980) is applied to prognose TKE. The Rapid Radiative Transfer Model (RRTM; Mlawer et al., 1997) with 16 LW band is utilized to calculate LW radiative fluxes. The correlated-k method is used to simulate the cloud top radiative cooling and heating rates. Shortwave radiation is represented using the Dudhia scheme (1989) to include solar flux, shortwave absorption and scattering in clear air, and reflection and absorption in cloud layers. A damping layer of 300m thickness is employed in the upper boundary of domain for absorbing gravity wave energy to minimize the unphysical wave reflection off the upper boundary of the domain. Periodic boundary conditions in both x- and y- directions are assumed in the simulations. The monotonic flux limiter is applied to the basic advection scheme for scalar transport, as suggested by Wang et al. (2009) to avoid overestimates of cloud water and precipitation in cloud-scale simulations.

2.5 Experimental Design

The WRF model with detailed bin microphysics is used to simulate an idealized MSc case through a 30 hr diurnal cycle. The aerosol is assumed to be fully soluble ammonium sulfate with lognormal distribution mean radius 0.1 μm and geometric standard deviation 1.5. The

initial sounding profile for the control case (Fig. 2.1) is loosely based on the First International Satellite Cloud Climatology Project Regional Experiment (FIRE I; Duynkerke et al., 2004) in July 1987, with the total water mixing ratio decreased by 0.5 g kg^{-1} for a moderately drizzling (0.1–1 mm day^{-1}) cloud. The case simulated is a shallow boundary layer with a depth of ~600 m and topped with a 12 K and -3 g kg^{-1} temperature and moisture inversion, respectively. The Coriolis parameter is 8×10^{-5} s^{-1} (33.5 N, 119.5 W). Other initial conditions are similar to those in Hill et al. (2009). The nominal sea surface temperature (SST) is set to 288 K, and surface pressure is assumed to be constant at 1012.5 mb. The wind field is -1 m s^{-1} in the x-direction and 6 m s^{-1} in the y-direction. The nominal large-scale divergence rate (D), 5.5×10^{-6} s^{-1}, is given to prescribe the subsidence rate W_{sub}=-Dz, where z is the height above surface. The initial temperature field is perturbed pseudo-randomly by an amplitude of 0.1 K to accelerate the spinup of convection. Results are not sensitive to this amplitude. Both LW and SW radiation are considered. Radiative forcing is computed every time step. In order to avoid MSc dissipation due to strong solar radiation in summer, winter conditions are chosen for SW radiation.

The simulations are performed within a 3 km × 3 km × 1.6 km domain for 30 hr. The grid resolution is 20 m vertically and 50 m horizontally, with a 0.5 s time stop. Aerosol number concentrations (N_a) of 100, 200, and 1000 cm^{-3} are taken to correspond to clean, semi-polluted, and polluted cases, respectively. For computational efficiency, sensitivity studies are performed over a smaller horizontal domain size, 1 km in x- and y- directions. Fig. 2.2 shows that the cloud bulk properties of larger (3 km × 3 km) and smaller (1 km × 1 km) domain sizes are similar. Since our focus is on the directional changes of cloud properties in response to different ambient conditions, the smaller domain is sufficient for sensitivity studies. Four significant environmental variables that control the structure of the MSc are considered: SST, free tropospheric water vapor mixing ratio (q_{ft}), large-scale divergence rate (D), and wind speed (U and V). The lower BL stability is controlled mainly by SST (Klein and Hartmann, 1993). The humidity above the BL determines the drying/warming effect through entrainment. The large-scale divergence D affects the subsidence rate. The wind speed is considered, as it affects the surface fluxes and the updraft velocity.

The simulations performed are listed in Table 2.3. In cases SST290 and SST292, SST is increased by 2K and 4K, respectively. In cases QFT3 and QFT1, the free tropospheric

water vapor mixing ratio is decreased to 3.1 and 1.1 g/kg, respectively; the temperature profile remains unchanged. In cases DIV3 and DIV8, the large scale divergence rate is set to 3.0×10^{-6} and 8.0×10^{-6} s^{-1}, respectively, with all else unchanged. In WIND case, the wind speed is set to -4 m/s in the x-direction and 10 in the y-direction, stronger than the Control case. Both clean and polluted scenarios are simulated for each condition.

2.6 Results

2.6.1 Control case

The simulations start at 00:00 h local time. During nighttime, cloud top LW radiative cooling generates positive buoyancy in the cloud layer (Fig. 2.4a), which enhances TKE and mixing, destabilizing the MBL and increasing the cloud top entrainment. Cloud-top entrainment tends to raise the cloud base by diluting the cloud with warm and dry air, but it also tends to lift cloud top height (e.g., Randall, 1984). With stronger mixing, water vapor from the surface is transported to upper layers more efficiently, causing the difference between water vapor mixing ratio at the reference level and saturation mixing ratio at the surface to increase, and thus leading to a higher surface moisture flux. This results in a moister cloud layer, increased cloud thickness and LWP at nighttime (Fig. 2.5a, 2.5b). For the clean case (N_a = 100 cm^{-3}), measurable surface precipitation begins at 5 h as LWP increases, proceeding from light drizzle (surface rain rate < 0.1 mm day^{-1}) to moderate drizzle (0.1–1 mm day^{-1}) after 7 h. During the daytime, the heating due to cloud absorption of solar radiation partially offsets the cloud top LW cooling, stabilizing the MBL. Heating of the cloudy layer via SW absorption acts to thin the cloud; surface precipitation is suppressed after 12 h (Fig. 2.5d). Also, the MSc becomes decoupled from the sub-cloud layer as the cloud gets slightly warmer than the sub-cloud layer and a stable layer occurs at the cloud base. In the θ_l and q_t daytime profiles (Fig. 2.4b, 2.4c), it is shown that the moister and cooler surface air is not transported to the cloud layer effectively (12–14 h). As the cloud continues to warm, the LWP decreases, attaining a minimum at ~14 h. It is noted, however, that the solar heating is likely overestimated with the Dudhia SW radiation scheme and leads to overly reduced daytime cloud water.

After 14 h, cloud top height begins to increase again due to a decrease in downwelling SW radiation, and drizzle appears after ~16 h (Fig. 2.5d). In the clean case, the drizzle

evaporation below the cloud can moisten and cool the sub-cloud layer, increasing the relative humidity of the sub-cloud air, lowering the cloud lifting condensation level, hence lowering cloud base (Lu and Seinfeld, 2005). Also, the cloud-top entrainment decreases in the presence of drizzle, therefore the cloud top falls. The decreased entrainment drying/ warming increases the MBL relative humidity and leads to a lower lifting condensation level. Therefore, more raindrops are likely to reach the surface before evaporating in the sub-cloud layer. As the surface precipitation increases during the second night, the cloud becomes optically thinner (Fig. 2.5f) and cloud top LW cooling decreases, allowing subsidence to compress the MBL. The cloud eventually disappears at ~24 h.

Proceeding from clean to semi-polluted (Na =200 cm^{-3}) condition, more numerous and smaller cloud droplets undergo less efficient collision-coalescence, which leads to a suppression of precipitation. Therefore, the semi-polluted case is nonprecipitating for the first 25 h. The precipitation suppression at nighttime results in higher TKE, because in the presence of precipitation, drizzle formation leads to stabilization of the sub-cloud layer through evaporative cooling and moistening. The cooling and moistening below the cloud leads to weaker turbulence intensity and inhibition of deeper mixing, and may also lower the cloud base (Lu and Seinfeld, 2005). During the daytime this can partially offset the warming of the cloud base due to absorption of solar radiation and counteract the tendency for the cloud base to rise (Sandu et al., 2008). The existence of drizzle reduces the buoyancy, stabilizes the MBL, decreases the TKE, and reduces the entrainment strength. As a result, precipitation suppression due to increased N_a increases the buoyancy fluxes and TKE, destabilizes the MBL, enhances the cloud-top entrainment (as shown in pathway (c)), and establishing a well-mixed MBL. This is consistent with previous findings (e.g., Stevens et al., 1998; Ackerman et al., 2004; Lu and Seinfeld, 2005; Wood, 2007).

From 10 to 15 h, the semi-polluted cloud thins due to solar heating. With a stabilized MBL and decreased TKE during the daytime, the cloud top falls by 80m due to reduced cloud top entrainment. As the MBL gradually warms with SW heating, the relative humidity in the MBL decreases, causing the cloud base to rise by 100 m. Consequently, LWP decreases as cloud thins. During the second night, the LWP of the semi-polluted cloud increases with weaker SW heating, exceeding 110 g m^{-2}, and drizzle appears in the last 5 h of the simulation.

Proceeding from semi-polluted to polluted condition (N_a=1000 cm^{-3}), stronger TKE is generated from sedimentation-entrainment and evaporation-entrainment by numerous smaller cloud droplets (as discussed previously in Chapter 1. pathway (d) and (e)), resulting in a drier cloud layer and less LWP, as compared to the semi-polluted cloud. This is evident from the vertical profile of vertical velocity variance ($\overline{w'w'}$, a measure of strength of turbulent mixing, Fig. 2.3a). This result agrees with that of Ackerman et al. (2004), in that the entrainment increases with increasing N_a in all simulations. And the LWP is lower in the polluted cloud than in the semi-polluted cloud for the 30 h duration (Fig. 2.4a). After 1500 h, as in the case of the semi-polluted cloud, the well-mixed MBL is restored through enhanced LW cooling and TKE, and the cloud grows even thicker than during the first night. Compared to the clean case, in the absence of precipitation the MSc lifetime increases.

It is shown that when the surface precipitation rate exceeds ~ 0.1 mm day^{-1}, the LWP increases with N_d (following effect (b)). Similar trends have also been found in other nocturnal MSc studies (Table 2.1), in which opposite responses of LWP to an increase in N_a for moderate/heavy and non/light drizzling conditions occur. In Fig. 2.5f, the cloud optical depth, , is calculated by

$$\tau = \iint 2\pi r^2 \, n(r) dr dz \qquad (2.7)$$

where the extinction efficiency is approximately 2 at visible wavelengths for the typical size of cloud drops (Seinfeld and Pandis, 2006), and n(r) is the droplet number concentration distribution. It is shown that the cloud optical depth increases with N_a (Fig. 2.5f), with larger enhancement at night than during the daytime. During the 30 h simulation, cloud optical depth, as well as LWP, precipitation, and cloud fraction exhibit a strong diurnal variation (Fig. 2.5). The cloud fraction remains 100% for semi-polluted and polluted cases except from 12 to 14 h when SW heating is strongest. However, under clean condition, with both precipitation and solar heating, cloud fraction decreases significantly (Fig. 2.5g). Also, as a result of more pronounced entrainment, the polluted cloud is warmer and drier than the clean and semi-polluted clouds (Fig. 2.4b, 2.4c).

The overall effect (Control cases) of changes in N_a can be summarized as follows: (1) with non/light drizzle (surface precipitation rate < 0.1 mm day^{-1}), increase in N_a results in stronger entrainment and thus lower LWP; and (2) with moderate/heavy drizzle (surface

precipitation rate > 0.1 mm day^{-1}), increase in N_a results in precipitation suppression, and thus higher LWP. (Note that clouds are classified as non/light drizzling and moderate/heavy drizzling rather than as clean and polluted.) For the diurnal variation, nighttime LWP is larger than daytime LWP, a result of cloud thinning and decoupling during daytime. Overall, cloud optical depth increases with increased N_a (Fig. 2.5f). These effects are consistent with the studies listed in Table 2.1.

2.6.2 Sensitivity to environmental conditions

2.6.2.1 Effects of SST – SST290 and SST292 cases

First, we examine the effect of a higher SST on the response of the MSc to perturbations in aerosol concentration. As SST increases, the surface sensible and latent heat fluxes increase accordingly (Fig. 2.6c, 2.6g), resulting in higher θ_l and q_t in the MBL (Fig. 2.7b, 2.7c). The extent of heating exceeds the extent of moistening in terms of affecting the relative humidity, resulting in lower relative humidity under higher SST, and thus higher cloud base. The increased surface fluxes also enhance the TKE (Fig. 2.7a) and cloud top entrainment, and therefore deepen the cloud by rising cloud top (Fig. 2.6b). Overall, cloud base rises more than cloud top, resulting in a thinner cloud, consistent with the short time scale responses in Lu and Seinfeld (2005). In SST290 and SST292 clean cases, the precipitation is suppressed (Fig. 2.6d) because of a thinner cloud and lower LWP. During the daytime, the cloud thickness is constrained by both solar absorption and the warmer MBL. In the second night, the LW radiation enhances the turbulence and MBL overturning, and a well-mixed state is reestablished, causing the cloud to thicken. The precipitation in SST290 clean case initiates at ~20 h, and with moderate drizzling rate (0.1–1 mm day^{-1}) after 21 h, the cloud becomes very thin in the end of simulation. While in SST292 clean case, lower LWP prevents the cloud from drizzling, and it keeps thickening in the second night.

In SST290 and SST292 polluted cases, stronger entrainment drying/warming due to evaporation and sedimentation feedbacks as compared to that in clean cases further dries the MBL, leading to cloud dissipation at ~14 h with existence of strong solar heating. With the onset of the second night, the LW-driven TKE enhances the vertical advection of water

vapor, gradually replenishing moisture at the lifting condensation level. The cloud reforms at ~27 h and 20 h for SST290 and SST292 polluted cases, respectively (Fig. 2.6f).

The overall effect of an increasing SST can be summarized as follows: (1) when SST is increased as compared to the Control case, the simulated cloud thins and LWP decreases on a short time scale (several hours); and (2) when SST is increased and N_a is increased, entrainment effects are more pronounced and LWP decreases.

2.6.2.2 Effects of free tropospheric humidity – QFT3 and QFT1 cases

As the free tropospheric air becomes drier, the larger discontinuity in humidity between the MBL and the free troposphere results in stronger evaporative cooling in the cloud top inversion region. This enhances the TKE and leads to stronger mixing and increased cloud top entrainment. As more dry air is entrained into the cloud layer, the MBL gets drier, causing the surface latent heat flux to increase. Compared to the Control case, the enhanced cloud top entrainment leads to a deeper MBL as well as stronger drying and warming. As a result, both the cloud top and base rise (Fig. 2.8b, 2.8f), with the cloud base rising more, thus resulting in a thinner cloud. The effects of the free tropospheric moisture can be summarized (Ackerman et al., 2004) as: (1) moist entrained air → does not dry MBL effectively → cloud thickening, versus (2) dry entrained air → dry the MBL → cloud thinning. Similar results were also obtained by Sandu et al. (2008) for a diurnal cycle.

In the QFT3 case, no precipitation indicates stronger mixing in the MBL so the vapor from the surface is transported more efficiently to the cloud layer. The increased surface moisture flux compensates for the drying from enhanced entrainment, and the cloud thickens at night. However in the QFT1 case, the cloud thins as drying from entrainment mixing exceeds the moistening from the surface flux (Fig. 2.8a, 2.8e). In the QFT3 clean case, the precipitation occurs after 20 h, with heavier drizzle (> 0.1 mm day^{-1}) occurring after 21 h. The cloud eventually dissipates by the end of simulation. On the other hand, the lower LWP in the QFT1 clean case prevents the cloud from precipitating during the 30 h duration. In the second night, the cloud deepens as the surface moisture flux outweighs the drying by entrainment, and LWP gradually increases. Compared to the QFT1 polluted case, LWP is higher in the clean case than in the polluted case within the 30 h duration.

The overall effect of a drier free troposphere can be summarized as follows: (1) when q_{ft} is decreased as compared to the Control case, the cloud thins and LWP decreases on a short time scale; and (2) when q_{ft} is decreased and N_a is increased, entrainment effects are significant and LWP decreases.

2.6.2.3 Effects of large-scale divergence – DIV3 and DIV8 Cases

Changes in the large-scale divergence rate mainly affect the cloud top height. As the large-scale divergence weakens (DIV3), the cloud height increases, and the cloud thickens. In the DIV3 clean case, this results in earlier and heavier precipitation than in the Control case (Fig. 2.9d). During the first night, surface precipitation initiates at ~4 h with a maximum rate of 0.45 mm day^{-1}. During the day, LWP decreases, reaching a minimum at ~14 h (Fig. 2.9a), the same as in the Control case. The cloud thickens again afterwards as the SW heating decreases. Due to the lower cloud layer in the second evening (Fig. 2.9b), precipitation droplets are less likely to evaporate before reaching the surface, causing heavier surface precipitation to occur between 16 and 21 h, with a maximum rate of 1.2 mm day^{-1}, and eventually the cloud dissipates at ~22 h.

In the DIV3 polluted case, the cloud thickens with the LWP reaching ~150 gm^{-2} during the first night, as compared to ~100 gm^{-2} in the Control case (Fig. 2.9e). During the second night, the cloud grows even thicker, with LWP reaching 160 gm^{-2} at the end of the simulation, showing that with a weaker subsidence rate, the polluted cloud can keep thickening without being strongly capped.

In the DIV8 case, on the other hand, the stronger subsidence results in a lower inversion height and therefore a lower cloud top height. In the DIV8 clean case, lower LWP inhibits precipitation during the first night. Compared to the DIV3 and Control clean clouds, the cloud dissipates later due to later onset and less drizzle. In the DIV8 polluted case, however, the cloud disappears due to stronger subsidence and daytime solar absorption. It is shown that when the subsidence rate is increased, the cloud thins due to a decrease in cloud top height and is even able to dissipate completely. The overall effect of the large-scale divergence rate can be summarized as follows: (1) in the precipitating case, when D is increased as compared to the Control case, the cloud thins and LWP decreases on a short

time scale; and (2) when D is increased (decreased) and N_a is increased, stronger entrainment (precipitation suppression) leads to lower (higher) LWP.

2.6.2.4 Effects of stronger wind speed – WIND Cases

Stronger wind (U and V are −4 and 10 ms^{-1}, respectively; compared to −1 and 6 ms^{-1} in Control case) increases the surface latent heat fluxes, resulting in slightly higher LWP than in the Control case, and thus more precipitation in the clean case (Fig. 2.10d). Stronger sedimentation lowers the cloud top and base relative to the Control case (Fig. 2.10b). In the afternoon, the LWP increases and heavy drizzle occurring in the clean case causes the cloud to disappear at ~21 h, earlier than that in the Control clean case. This is a result of significant water loss due to low cloud base. In the polluted case, on the other hand, it shows similar diurnal variation as the Control case (Fig. 2.10f), but with higher LWP than the Control case at night. It is shown that within the range simulated, the cloud response is not very sensitive to the wind speed compared to other environmental variables.

The overall effect of stronger wind speed can be summarized as follows: (1) when U, V are increased as compared to the Control case, the cloud thickens and LWP increases, resulting in heavier precipitation (short time scale); and (2) when U, V are increased and N_a is increased, precipitation is suppressed and LWP is higher than that of the case with lower N_a.

2.6.3 LWP differences between clean and polluted cases

The LWP difference between the polluted and clean case (ΔLWP) for all cases is shown in Fig. 2.11 (after 16 h the cloud dissipates in some cases). For Control, DIV3 and WIND cases, LWP is higher under polluted conditions (ΔLWP > 0), with the maximum ΔLWP reaching 70 gm^{-2} in the DIV3 case. This is because under these conditions in which heavier precipitation occurs (Figs. 9d, 10d), the increase in aerosol number concentration more effectively suppresses precipitation, resulting in less water loss and higher LWP. In contrast, the other cases (SST290, SST292, DIV8, QFT3 and QFT1 case) have lower LWP in the polluted condition than the clean condition (ΔLWP < 0), which shows that in the absence of precipitation or with light drizzle, the evaporation-entrainment effect and

sedimentation-entrainment effect are pronounced in the polluted case, causing LWP to decrease. The minimum ΔLWP is ~ −28 gm^{-2} in the QFT1 case, showing that the drier the free troposphere, the stronger the entrainment effect. The time evolution of difference in LWP between polluted and clean condition has the same tendency as compared to Fig. 2.7 of Sandu et al. (2008), with larger LWP difference under moister conditions, and vice versa. Also, during daytime the LWP difference decreases, and becomes negative for all simulations after ~14 h, similar to the results in Sandu et al. (2008).

2.6.4 Relation of LES experiments to analytical approximation

Equation (2.3) is an approximate analytical expression relating changes in N_a to changes in various cloud properties. Here we attempt to estimate the sign and relative magnitude of each term in equation (2.3) using the LES simulation. To evaluate the derivatives we use finite differences, ΔN_a, to represent dN_a, using N_a values of 100, 200, 500 and 1000 cm^{-3}. As noted earlier, while the diabaticity effect, $d(lnf)/d(lnN_a)$, is expressed separately in equation (2.3), this effect cannot easily be separated numerically from the others in Eq. (2.3). Therefore, $\Delta\,(lnN_d)/\Delta\,(lnN_a)$ is estimated rather than $\Delta\,(lnN_{ad})/\Delta\,(lnN_a)$; and the estimation of $\Delta\,(lnk)/\Delta\,(lnN_a)$ and $\Delta\,(lnH)/\Delta\,(lnN_a)$ already incorporates the adiabaticity effect. Control, SST290, QFT3, and DIV3 cases are considered to evaluate each term. The relationship of τ, N_d, k, and H to N_a are calculated by conditionally-averaging over the cloudy fraction of the domain. Nighttime (4–7 h) and daytime (12–15 h) are discussed separately (Fig. 2.12).

2.6.4.1 Twomey effect

The estimated value of $\Delta\,(lnN_d)/\Delta\,(lnN_a)$ is within the range of 1.00–1.25 at night (4–7 h) and 0.83–1.37 during the day (12–15 h) (Table 2.4), with a lower value in SST290 and QFT3 cases than in Control and DIV3 cases, a result of a drier atmosphere and lower supersaturation, and thus lower N_d. During the daytime, N_d is lower than that at nighttime due to solar heating (Fig. 2.12), and the values of $\Delta\,(lnN_d)/\Delta\,(lnN_a)$ are more scattered. Compared to other studies (Table 2.2), the estimated magnitude of $\Delta\,(lnN_d)/\Delta\,(lnN_a)$ is higher, as compared to the range of 0.6 to 0.9 based on Eqs. (2.4) and (2.5).

2.6.4.2 Dispersion effect

The coefficient k is calculated (Martin et al., 1994; Lu and Seinfeld, 2006) as a function of relative dispersion (d) and skewness (s) of the droplet number concentration distribution $n(r)$,

$$k = \frac{(1+d^2)^3}{(sd^3+1+3d^2)^2} \tag{2.8}$$

where $= \sigma/\bar{r}$, $\bar{r}$ is mean droplet radius, σ is the standard deviation of droplet spectrum, given by

$$\sigma = (\frac{1}{N_d}\int (r-\bar{r})^2 n(r)dr)^{1/2} \tag{2.9}$$

, and skewness s is defined as

$$s = \frac{1}{\sigma^3 N_d}\int (r-\bar{r})^3 n(r)dr. \tag{2.10}$$

The calculated k from the simulations is within the range of 0.5 to 0.9 (Fig. 2.9a). During the daytime, *k* is smaller than at night, suggesting that the evaporation of cloud droplets due to SW heating results in a more dispersed droplet spectrum and smaller *k*. Also, the estimated $\Delta\ (lnk)/\Delta\ (lnN_a)$ at nighttime is smaller for the drier cases (SST290 and QFT3), and larger for the moister case (DIV3). In the DIV3 case with stronger precipitation, $\Delta\ (lnk)/\Delta\ (lnN_a)$ accounts for 10% of total cloud susceptibility, larger than in other cases with less precipitation; this result is consistent with Lu and Seinfeld (2006), where smaller value of $\Delta\ (lnk)/\Delta\ (lnN_a)$ occurs for the cloud with weaker drizzle, and larger value with stronger precipitation. This is because with increased N_a, there is less spectral broadening due to suppressed collision-coalescence. Also, spectral narrowing occurs via condensational growth in regions of higher updraft velocities because suppressed precipitation leads to stronger TKE. The positive correlation of *k* to N_a is consistent with Miles et al. (2000) and individual ship tracks in Lu et al. (2007), yet opposite to that obtained by other flight-averaged data (Martin et al., 1994; Liu and Daum, 2002; ensemble cloud averages in Lu et al. (2007)).

Lu et al. (2007) found that on the ensemble-averaged cloud scale (~several tens of kilometers), an increase in N_a results in spectral broadening (smaller k), because for the flight-averaged data, the relationship between k and N_a are affected not only by N_a but also by various meteorological conditions in different sampling locations. The meteorological differences thus affect the dynamical factors, such as entrainment mixing, updraft velocity, drizzle strength, etc., which accordingly changes the dispersion width. Therefore for the flight-averaged observational data, the clean and polluted clouds were not necessarily subject to the same sounding (Lu et al., 2007), which causes the k - N_a relationship to be contaminated with factors other than simply changes in N_a. While on the scale of a cloud perturbed by a single ship track, spectral narrowing (larger k) occurs in response to increased N_a, for which the similar sounding is embedded in the ship track and clean regions. In this LES study, with the ambient conditions being fixed, the environment is identical, and the aerosol-induced dispersion changes can therefore be distinguished and separated from other meteorological factors.

2.6.4.3 Cloud thickness effect

Aerosols exert the main influence on cloud thickness through precipitation efficiency, radiation, and cloud dynamics (entrainment). The estimated $\Delta\ln H/\Delta\ln N_a$ at nighttime is slightly negative (~ −0.01 to −0.04) within the range of simulated environmental conditions (Table 2.4), except for the DIV3 case ($\Delta\ln H/\Delta\ln N_a$ =0.014) in which stronger drizzle occurs in the clean case, causing H to increase with increasing N_a, a result of precipitation suppression. As N_a increases from 200 to 1000 cm^{-3}, $\Delta\ln H/\Delta\ln N_a$ is negative in all cases (Fig 12) as a result of evaporation-entrainment and sedimentation-entrainment effects. During the daytime, H is smaller and the values of $\Delta\ln H/\Delta\ln N_a$ is more scattered than at night. The sign of $\Delta\ln H/\Delta\ln N_a$ is consistent with Lu and Seinfeld (2005) (Table 2.2), where $\partial \ln LWP/\partial \ln N_a$ is negative, with a larger impact under clean background. The cloud thickness effect is the only one that exhibits either positive or negative magnitude, which enhances or counteracts other effects

2.6.4.4 Cloud optical depth susceptibility

Cloud optical depth is calculated following Eq. (2.7). As N_a increases from 100 to 1000 cm^{-3}, the estimated value of $\Delta\ln\tau/\Delta\ln N_a$ lies between 0.28 and 0.53 at night, with higher

value in the DIV3 case and lower value in the SST290 and QFT3 cases (Table 2.4). This suggests that with a moister atmosphere and heavier precipitation, $\Delta\ln\tau/\Delta\ln N_a$ is larger. Also, $\Delta\ln\tau/\Delta\ln N_a$ is larger at lower N_a. In the nighttime Control case, as N_a doubles from 100 to 200 cm^{-3}, $\Delta\ln\tau/\Delta\ln N_a$ is more than two times larger than that when doubling N_a from 500 to 1000 cm^{-3} (0.54 versus 0.24), suggesting that total cloud susceptibility is stronger under lower N_a. This is because when N_a increases from that of a clean background, transition from precipitating to non-precipitating cloud results in more pronounced enhancement of total cloud susceptibility.

During the daytime, the magnitude of is lower as a result of solar heating and cloud thinning (Fig. 2.12). The magnitude of $\Delta\ln\tau/\Delta\ln N_a$ lies between −0.36 and 0.63, more scattered than that of the nighttime (0.28–0.53). Because the MBL decouples and the cloud thins significantly during the day, the evaluation which is based on only cloudy grids has a larger standard deviation and should be viewed with more caution. In the SST290 case, $\Delta\ln\tau/\Delta\ln N_a$ is actually negative during the day, a result of cloud dissipation under polluted case. With higher temperature, cloud droplet evaporation during the day causes the cloud to disappear (Fig. 2.6f).

Comparing $\Delta\, ln\tau/\Delta\, lnN_a$ from LES simulation and from equation (2.3) (Table 2.4), it is seen that the two values are quite close to each other for most cases. The difference between these two estimated $\Delta\, ln\tau/\Delta\, lnN_a$ value lies within the margin of error (standard deviation), with the largest discrepancy occurring in daytime case SST290. Note that the standard deviation is also large for daytime SST290, showing the value is less representative than in other cases. The relatively close agreement between the direct calculation and Eq. (2.3) was not necessarily to have been expected. The analytical formulation can therefore be treated as a good approximation of cloud optical depth susceptibility.

Considering the significance of each term in contributing to the cloud susceptibility $\Delta\, ln\tau/\Delta\, lnN_a$, the Twomey effect $\Delta\, lnN_d/\Delta\, lnN_a$ is the dominant term, contributing over 85% of the total effect during the nighttime. The dispersion effect accounts for 3% to 10% of the total effect at night, and the cloud thickness effect accounts for 5% to 22% of the overall effect, acting to diminish or enhance the Twomey effect.

During daytime the ranges of values are more scattered due to the MBL decoupling and significant cloud thinning. Certain processes, including the solar absorption, cloud top entrainment, reducing surface buoyancy fluxes, and drizzle evaporation below cloud base tend to promote a more stable density stratification within the MBL (Nicholls, 1984; Lewellen and Lewellen, 2002). Daytime absorption of solar radiation often leads to afternoon cloud thinning due to decoupling. Decoupling can occur when sub-cloud buoyancy fluxes become negative, inhibiting convection below cloud base (e.g., Bretherton and Wyant, 1997). The existence of decoupling can be diagnosed using the buoyancy integral ratio (BIR) (Turton and Nicholls, 1987; Bretherton and Wyant, 1997) defined as:

$$BIR = -\int_{z^*} \langle w'\theta_v' \rangle dz \; / \; \int_{all\ other\ z} \langle w'\theta_v' \rangle dz \tag{2.11}$$

where z^* indicates integration over the region below cloud base height in which $\langle w'\theta_v' \rangle < 0$, and θ_v is virtual potential temperature. In Turton and Nicholls (1987), the value BIR > 0.4 is chosen as a condition for decoupling of the sub-cloud layer and the cloud layer. Bretherton and Wyant (1997) suggest that the threshold value BIR > 0.15 is more appropriate. BIR values under nighttime (4–7 h)/daytime (12–15 h) conditions and clean / polluted cases are shown in Fig. 2.14 for eight cases. If BIR > 0.15 is used for the decoupling threshold, the MBL in most daytime cases is decoupled. As the daytime solar heating offsets the cloud top radiative cooling, less production of turbulence by cloud top cooling favors greater decoupling (e.g., Bretherton and Wyant, 1997; Stevens, 2000) and hence a thinning of the stratocumulus layer. The largest BIR is shown in DIV8 polluted case during the daytime condition. In the DIV8 polluted case, stronger subsidence and enhanced entrainment lead to a thinner cloud. Solar heating during the daytime further results in enhanced decoupling of sub-cloud layer and the cloud layer, which leads to cloud dissipation at ~14 h. In the WIND cases, stronger wind helps ventilate the surface. The surface latent heat flux, which is proportional to the mean wind, becomes more negative in the polluted case (Fig. 2.10g). This results in lower buoyancy flux near the surface, and enhanced decoupling of the sub-cloud layer and cloud layer. Thus BIR is higher under WIND polluted case during the daytime.

Under nighttime conditions, the MBL is well mixed, with BIR < 0.15 in all cases. However, the MBL under DIV3 and WIND clean conditions has slightly higher BIR than

others, indicating that the heavier precipitation in DIV3 and WIND clean conditions leads to a more stable boundary layer and a less mixed/coupled MBL compared to those with lighter or no precipitation. This shows that below-cloud evaporation of drizzle produces a cooler and moister sub-cloud layer that inhibits deep mixing. Overall, it is shown that decoupling is most likely to occur during daytime.

2.6.4.5 Ratio of indirect effects

Ignoring the dispersion and diabaticity effects, Eq. (2.3) can be rewritten as:

$$\frac{dln\tau}{dlnN_a} = \frac{1}{3}\left(\frac{dlnN_d}{dlnN_a} + 5\frac{dlnH}{dlnN_a}\right) \quad (2.12).$$

One can define the ratios of the cloud thickness effect to the Twomey effect, that is, $R_{IE} = 5(\frac{\Delta\, lnH}{\Delta\, lnN_d})$ (Wood, 2007). A value of R_{IE}=1 corresponds to the cloud thickness effect doubling the Twomey effect, and R_{IE}=-1 implies a complete cancellation the Twomey effect. In Wood (2007), with given environmental forcing, the MLM determines the equilibrium state of the MBL. By perturbing N_d by 5%, the analytical response indicates that R_{IE} is strongly tied to cloud base height on a short time scale (0–8 h); and only when the cloud base height is very low does the cloud thickness effect outweigh the Twomey effect.

In this study we perform an examination similar to that of Wood (2007) by doubling the aerosol concentration from 100 to 200 cm^{-3}. Here RIE is calculated by $5(\frac{\Delta\, lnH}{\Delta\, lnN_a})/(\frac{\Delta\, lnN_d}{\Delta\, lnN_a})$, from the LES simulation, and the value is averaged over 4–7 h for 27 cases, covering the variables and values listed in Table 2.5. Fig. 2.15a demonstrates a similar trend in RIE as that shown by Wood (2007) (Fig. 2.8a). With higher cloud base, RIE < 0, and vice versa.

The positive RIE appears only in Control and DIV3 cases, where the moister environment leads to lower cloud base and stronger precipitation in the unperturbed (N_a 100 cm^{-3}) condition. The other cases have negative RIE, suggesting the cloud thickness effect offsets the Twomey effect. In a drier environment, the cloud base is higher, and thus less precipitation occurs under clean conditions. With increased aerosol, the enhanced entrainment effect therefore results in a thinner cloud and negative cloud thickness effect.

The lowest RIE (−1.47) appears under the driest condition (in which SST is 292 K, D is 8×10^{-6} s^{-1}, and q_{ft} is 1.1 g kg^{-1}). The relationship between RIE and cloud thickness (Fig. 2.15b) also shows a positive correlation; a thicker cloud corresponds to a larger RIE, and vice versa.

To fully cover the responses to different aerosol perturbations during nighttime/daytime, RIE values are also calculated with changes from 100 to 200 cm^{-3} and 200 to 1000 cm^{-3} under both nighttime and daytime conditions for four cases (Control, SST290, QFT3, and DIV3, Fig. 2.16). The same trend of RIE versus cloud base height is shown as that in Wood (2007), with larger RIE corresponding to lower cloud base and smaller RIE corresponding to higher cloud base. The range of RIE values during the nighttime (−0.42 to 0.20) is smaller than that during the daytime (−4.18 to 1.38), showing that RIE is more scattered during the daytime. From N_a 100 to 200 cm^{-3}, RIE is positive for both day and night conditions for the heavier drizzling cases (Control and DIV3), and is negative for the non/light drizzling cases (SST290 and QFT3). This suggests that with suppressed precipitation, RIE tends to be positive (cloud thickens). From N_a 200 to 1000 cm^{-3}, RIE is negative for all the cases considered, as the pronounced evaporation-entrainment and sedimentation-entrainment feedbacks lead to cloud thinning.

Environmental conditions that favor higher cloud bases are those of higher SST and a drier free troposphere, consistent with results of Wood (2007). Variation in large-scale divergence affects the cloud top height, but not the cloud base height, therefore RIE under difference divergence rates is independent of cloud base height.

2.7 Conclusions

Aerosol-cloud-precipitation interactions, which involve aerosol and cloud microphysics, atmospheric dynamics, and radiation, are complex and intertwined. We report here on a comprehensive numerical study of the dynamical response of MSc to changes in aerosol number concentration N_a using the WRF model with a detailed bin-resolved microphysical scheme as a three-dimensional LES model. Simulations are performed to explore the cloud diurnal responses to varied aerosol number concentration and different meteorological conditions (SST, free-tropospheric water vapor mixing ratio, large-scale subsidence, and wind speed). Based on the LES simulations, the magnitude and sign of the Twomey effect,

cloud droplet dispersion effect, cloud thickness effect, and cloud susceptibility are evaluated and compared with these from approximate analytical expressions that have been previously derived.

For moderate/heavy drizzling (> 0.1 mm day^{-1}) clouds, increase in N_a suppresses precipitation, causing the LWP to increase. For non/light drizzling (< 0.1 mm day^{-1}) clouds, an increase in N_a leads to numerous smaller cloud droplets, reducing the sedimentation, increasing the evaporation at cloud top, resulting in larger TKE, stronger entrainment, and LWP reduction. These are termed as sedimentation-entrainment and evaporation-entrainment effects. In daytime, SW heating offsets LW cooling, causing the cloud to thin, and reduced turbulent mixing results in a decoupled MBL. Over the 30 h duration, for the Control case, the clean cloud disappears during the second night due to enhanced precipitation, whereas the semi-polluted and polluted clouds continue to thicken. The dominant physical/dynamical mechanisms due to aerosol perturbations differ for moderate/heavy drizzling and non/light drizzling MSc.

Considering different environmental conditions, the simulated cloud responses are generally consistent with previous studies. Under higher SST, drier free-troposphere, or stronger large scale divergence rate, the clouds become thinner than in the Control case, and precipitation decreases. Higher SST causes both cloud top and base heights to increase, with cloud base being lifted more, resulting in a thinner cloud. Lower free-tropospheric humidity leads to stronger evaporation-entrainment, and therefore higher TKE and deeper MBL. Also, the entrainment dries the air, causing the cloud base to be higher. Overall, the cloud base elevates more than does the cloud top, thus creating a thinner cloud. Under stronger large scale subsidence, the cloud top is prohibited from rising; consequently the lower cloud top makes the cloud thinner. Under stronger wind speed, the enhanced surface fluxes moisten the MBL, thicken the cloud, and increase precipitation.

An analytical formulation of total cloud susceptibility to aerosol perturbations can be expressed by the sum of the Twomey, cloud droplet dispersion, cloud thickness, and diabaticity effects. Control, SST290, QFT3, and DIV3 cases covering N_a values of 100, 200, 500, and 1000 cm^{-3} are utilized to evaluate each effect for both nighttime and daytime conditions. The estimated Twomey effect is the dominant term in the total cloud

susceptibility and is larger under moister ambient conditions. The sign of the cloud droplet dispersion effect is positive; it is larger for heavier drizzling cases (Control and DIV3), and smaller for non/light drizzling cases (SST290 and QFT3). The dispersion effect plays a minor role in the total cloud susceptibility, accounting for 3%–10 % at night. The cloud thickness effect is negative in all cases, expect in DIV3 case, where stronger precipitation occurs in clean case, and thus an increase in N_a suppresses precipitation, causing the cloud to thicken. The drier the environment, the smaller the magnitude of $\Delta\ (lnH)/\Delta\ (lnN_a)$; the same trend as in the other effects. The cloud thickness effect is the only one that can reduce the total cloud susceptibility through cloud thinning.

The estimated magnitude of the cloud susceptibility, $\Delta\ (ln\tau)/\Delta\ (lnN_a)$, is between 0.28 and 0.53 at nighttime, with larger magnitude for heavier drizzling cases and smaller magnitude for non/light drizzling cases. Thus $\Delta\ (ln\tau)/\Delta\ (lnN_a)$ is more pronounced under a moister environment with stronger precipitation. Also, the total cloud susceptibility is larger in a cleaner background. Comparing the total cloud susceptibility derived directly from LES results and that calculated based on each individual effect, there is good agreement between the LES result and the analytical formulation, with the difference being within one standard deviation (Fig. 2.13). This indicates that the analytical expression is a useful form to evaluate cloud susceptibility. In daytime, the range of magnitude of each effect is more scattered as compared to nighttime. Because the MBL decouples and the cloud thins during the day, the evaluation which is based on only cloudy grids has a larger standard deviation should be viewed with more caution. Overall, however, the magnitude of each term during the daytime is larger for moderate/ heavy drizzling conditions, consistent with the nighttime tendency.

The ratio of the cloud thickness effect to the Twomey effect (RIE) is examined. It is found in a short time scale, the ratio depends on cloud base height and cloud thickness in the unperturbed clouds. For thicker clouds with stronger precipitation and lower cloud base, the cloud thickness effect enhances the Twomey effect. On the other hand, for drier cases with less precipitation and higher cloud base, they tend to have negative RIE, showing that the cloud thickness effect diminishes the Twomey effect. In the simulated cases, RIE is negative for most cases, showing that when there is no/light precipitation, the cloud thickness effect counteracts the Twomey effect.

From the comprehensive and systematic evaluation of the impact of aerosol, precipitation and meteorological conditions on the evolution of MSc, it is shown that MSc is sensitive to aerosol perturbation under clean background, and to the important meteorological conditions considered.

Also, the total cloud susceptibility to aerosol perturbation is larger under heavier drizzling clouds and cleaner environment. Among the Twomey, droplet dispersion, and cloud thickness effects which contribute to the total cloud susceptibility, Twomey effect dominates, droplet dispersion effect plays a minor role, and cloud thickness effect acts to enhance or counteract the Twomey effect, depending on precipitation strength and cloud base height. Moreover, the good agreement of total cloud susceptibility between analytical expression and LES simulation suggests that the analytical formulation is effective in representing the complex aerosol-cloud- precipitation interactions and is useful in quantifying the cloud responses to aerosol perturbations.

2.8 Acknowledgements

This work was supported by Office of Naval Research grant N00014-10-1-0200. The authors thank Frank Li, Adrian Hill, and Andreas Zuend for helpful suggestions. LX acknowledges the support of the Advanced Study Program at NCAR. HW thanks the Fund for Innovative Climate and Energy Research (FICER) at the University of Calgary. Computations were carried out on the CITerra Dell Cluster of the Geological and Planetary Sciences Division at Caltech.

2.9 Bibliography

Ackerman, A. S., Toon O. B., Taylor, J. P., Johnson, D. W., Hobbs, P. V., and Ferek, R. J.: Effects of aerosols on cloud albedo: Evaluation of Twomey's parameterization of the cloud susceptibility using measurement of ship tracks, J. Atmos. Sci., 57, 2684-2695, 2000.

Ackerman, A. S., Kirkpatrick, M. P., Stevens, D. E., and Toon, O. B.: The impact of humidity above stratiform clouds on indirect aerosol climate forcing, Nature, 432, 1014-1017, 2004.

Ackerman, A. S., vanZanten, M. C., Stevens, B., and coauthors: Large-eddy simulations of a drizzling, stratocumulus-topped marine boundary layer, Mon. Weather Rev., 137, 1083-1110, 2009.

Albrecht, B.: Aerosols, cloud microphysics, and fractional cloudiness, Science, 245, 1227-1230, 1989.

Brenguier, J.-L., Pawloska, H., Sch¨uller, L., Preusker, R., and Fischer, J.: Radiative properties of boundary layer clouds: Droplet effective radius versus number concentration, J. Atmos. Sci., 57, 803–821, 2000.

Bretherton, C. S. and Wyant, M. C.: Moisture transport, lower-troposphere stability, and decoupling of cloud-topped boundary, J. Atmos. Sci., 54, 148-167, 1997.

Bretherton, C. S., Macvean, M. K., Bechtold, P., Chlond, A., Cotton, W. R., Cuxart, J., Cuijpers, H., Khairoutdinov, M., Kosovic, B., Lewellen, D., Moeng, C.-H., Siebesma, P., Stevens, B., Stevens, D. E., Sykes, I., and Wyant, M. C.: An intercomparison of radiatively driven entrainment and turbulence in a smoke cloud, as simulated by different numerical models, Q. J. Roy. Meteorol. Soc., 125, 391–423, 1999.

Bretherton, C. S., Blossey, P. N., and Uchida, J.: Cloud droplet sedimentation, entrainment efficiency, and subtropical stratocumulus albedo. Geophys. Res. Lett., 34, L03813, doi:10.1029/2006GL027648, 2007.

Caldwell, P. and Bretherton, C. S.: Response of a subtropical stratocumulus-capped mixed layer to climate and aerosol changes, J. Climate, 22, 20-38, 2009a.

Caldwell, P. and Bretherton, C. S.: Large eddy simulation of the diurnal cycle in Southeast Pacific stratocumulus, J. Atmos. Sci., 66, 432-449, 2009b.

Chlond, A., and Wolkau, A.: Large-eddy simulation of a nocturnal stratocumulus-topped marine atmospheric boundary layer: An uncertainty analysis. Bound.-Layer Meteor., 95, 31-55, 2000.

Deardorff, J.: Stratocumulus-capped mixed layers derived from a three dimensional model. Bound.-Layer Meteor., 18, 495–527, 1980.

Duynkerke, P. G., de Roode, S. R., van Zanten, M. C., Calvo, J., Cuxart, J., Cheinet, S., Chlond, A., Grenier, H., Jonker, P. J., Kohler, M., Lenderink, G., Lewellen, D., Lappen, C.-

L., Lock, A. P., Moeng, C.-H., Muller, F., Olmeda, D., Piriou, J.-M., Sanchez, E., and Sednev, I.: Observations and numerical simulations of the diurnal cycle of the EUROCS stratocumulus case, Q. J. Roy. Meteor. Soc., 604, 3269-3296, 2004.

Feingold, G. and Chuang, P. Y.: Analysis of the influence of film-forming compounds on droplet growth: Implications for cloud microphysical processes and climate, J. Atmos. Sci., 59, 2006– 2018, 2002.

Feingold, G., Tzivion, S., and Levin, Z.: Evolution of raindrop spectra – Part I: Solution to the stochastic collection/breakup equation using the method of moments, J. Atmos. Sci., 45, 3387–3399, 1988.

Feingold, G. and Seibert, H.: Cloud-Aerosol Interactions from the micro to cloud scale, in: Clouds in the perturbed climate system: their relationship to energy balance, atmospheric dynamics, and precipitation, edited by: Heintzenberg, J. and Charlson, R. J., 319–338, MIT Press, Cambridge, UK, 2009.

Geresdi, I.: Idealized simulation of the Colorado hailstorm case: comparison of bulk and detailed microphysics, Atmos. Res., 45, 237-252, 1998.

Hall, W. D.: A detailed microphysical model within a two-dimensional framework: Model description and preliminary results. J. Atmos. Sci., 37, 2486-2507, 1980.

Hill, A. A., Dobbie, S., and Yin, Y.: The impact of aerosols on non-precipitating marine stratocumulus: Part 1. Model description and prediction of the indirect effect, Q. J. Roy. Meteor. Soc., 134, 1143-1154, 2008.

Hill, A. A., Feingold, G., and Jiang, H.: The influence of entrainment and mixing assumption on aerosol-cloud interactions in marine stratocumulus, J. Atmos. Sci., 66, 1450-1464, 2009.

IPCC: Summary for policymakers, in: Climate Change 2007: The Physical Science Basis, Contribution of Working Group I to the Fourth Assessment Report of the Intergovernmental Panel on Climate Change, edited by: Solomon, S., Qin, D., Manning, M., Chen, Z., Marquis, M., Averyt, K. B., Tignor, M., and Miller, H. L., Cambridge University Press, 2007.

Jiang, H., Feingold, G., and Cotton, W. R.: Simulations of aerosol-cloud-dynamical feedbacks resulting from entrainment of aerosol into the marine boundary layer during the Atlantic Stratocumulus Transition Experiment. J. Geophys. Res., **107,** 4813, doi:10.1029/2001JD001502, 2002.

Klein, S. A., and Hartmann, D. L.: The seasonal cycle of low stratiform clouds. J. Climate, 6, 1588–1606, 1993.

Lewellen, D. C. and Lewellen, W. S.: Entrainment and decoupling relations for cloudy boundary layers, J. Atmos. Sci., 59, 2966–2986, doi:10.1175/1520-0469(2002)059¡2966:EADRFC¿2.0.CO;2, 2002.

Lilly, D. K.: Models of cloud topped mixed layers under a strong inversion, Q. J. Roy. Meteor. Soc., 94, 292-309, 1968.

Lilly, D. K.: Entrainment into mixed layers. Part II: A new closure, J. Atmos. Sci., 59, 3353-3361, 2002.

Liu, Y., and Daum, P. H.: Anthropogenic aerosols: Indirect warming effect from dispersion forcing, Nature, 419, 580-581, 2002.

Lu, M.-L. and Seinfeld, J. H.: Study of the aerosol indirect effect by Large-Eddy Simulation of marine stratocumulus, J. Atmos. Sci., 62, 3909-3932, 2005.

Lu, M.-L. and Seinfeld, J. H.: Effect of aerosol number concentration on cloud droplet dispersion: a large-eddy simulation study and implications for aerosol indirect forcing, J. Geophys. Res., 111, D02207, doi:10.1029/2005JD006419, 2006.

Lu, M.-L., Conant, W. C., Jonsson, H. H., Varutbangkul, V., Flagan, R. C., and Seinfeld, J. H.: The Marine Stratus/Stratocumulus Experiment (MASE): Aerosol-cloud relationships in marine stratocumulus, J. Geophys. Res., 112, D10209, doi:10.1029/2006JD007985, 2007.

Martin, G. M., Johnson, D. W., and Spice, A.: The measurement and parameterization of effective radius of droplets in warm stratocumulus clouds, J. Atmos. Sci., 51, 1823–1842, 1994.

Miles, N. L., Verlinde, J., and Clothiaux, E. E. : Cloud droplet size distributions in low-level stratiform clouds, J. Atmos. Sci., 57, 295–311, 2000.

Mlawer, E. J., Taubman, S. J., Brown, P. D., Iacono, M. J., and Clough, S. A.: Radiative transfer for inhomogeneous atmospheres: RRTM, a validated correlated-k model for the longwave, J. Geophys. Res., 102(D14), 16663–16682, 1997.

Moeng, C.-H., Dudhia, J., Klemp, J. B., and Sullivan, P. P.: Examining two-way grid nesting for large eddy simulation of the PBL using the WRF model, Mon. Weather Rev., 135, 2295–2311, doi:10.1175/MWR3406.1, 2007.

Nicholls, S: The dynamics of stratocumulus – aircraft observations and comparisons with a mixed layer model, Q. J. Roy. Meteor. Soc., 110, 783–820, doi:10.1256/smsqj.46601, 1984.

Petters, M. D. and Kreidenweis, S. M.: A single parameter representation of hygroscopic growth and cloud condensation nucleus activity, Atmos. Chem. Phys., 7, 1961–1971, doi:10.5194/acp-7-1961-2007, 2007.

Pincus, R. and Baker, M. B.: Effect of precipitation on the albedo susceptibility of marine boundary layer clouds, Nature, 372, 250-252, 1994.

Pruppacher, H. R. and Klett, J. D.: Microphysics of Clouds and Precipitation, Kluwer Academic Publishers, Boston, 1997.

Randall, D. A.: Stratocumulus cloud deepening through entrainment, Tellus, 36, 446–457, 1984.

Randall, D. A., Coakley Jr., J. A., Fairall, C. W., Kropfli, R. A., and Lenschow, D. H.: Outlook for research on subtropical marine stratiform clouds. Bull. Amer. Meteor. Soc., 65, 1290-1301, 1984.

Rasmussen, R. M., Geresdi, I., Thompson, G, Manning, K., and Karplus, E: Freezing drizzle formation in stably stratified layer clouds: The role of radiative cooling of cloud droplets, cloud condensation nuclei, and ice initiation. J. Atmos. Sci., 59, 837-860, 2002.

Reisin, T., Levin, Z., and Tzivion, S.: Rain production in convective clouds as simulated in an axisymmetric model with detailed microphysics – Part I: Description of the model, J. Atmos. Sci., 53, 497–519, 1996.

Rotstayn, L. D., and Liu, Y.: Sensitivity of the first indirect aerosol effect to an increase of cloud droplet spectral dispersion with droplet number concentration, J. Climate, 16, 3476–3481, 2003.

Rotstayn, L. D., and Liu, Y.: Cloud droplet spectral dispersion and the indirect aerosol effect: Comparison of two treatments in a GCM, Geophys. Res. Lett., 36, L10801, doi:10.1029/2009GL038216, 2009.

Sandu, I., Brenguier, J. L., Geoffroy, O., Thouron, O., and Masson, V.: Aerosol impacts on the diurnal cycle of marine stratocumulus, J. Atmos. Sci., 65, 2705-2718, 2008.

Sandu I., Brenguier J.-L., Thouron O., and Stevens B.: How important is the vertical structure for the representation of aerosol impacts on the diurnal cycle of marine stratocumulus? Atmos. Chem. Phys., 9, 4039-4052, 2009.

Savic-Jovcic, V. and Stevens, B.: The structure and mesoscale organization of precipitating stratocumulus, J. Atmos. Sci., 65, 1587-1605, 2008.

Seinfeld, J. H. and Pandis, S. N.: Atmospheric Chemistry and Physics, John Wiley and Sons, Inc., Hoboken, NJ, 2nd edn., 2006.

Shao, H., and Liu, G.: A critical examination of the observed first aerosol indirect effect. J. Atmos. Sci., 66, 1018-1032, 2009.

Stevens, B.: Cloud transitions and decoupling in shear-free stratocumulus-topped boundary layers, Geophys. Res. Lett., 27, 2557–2560,doi:10.1029/1999GL011257, 2000.

Stevens, B.: Atmospheric moist convection, Annu. Rev. Earth Pl. Sc., 33, 605–643, doi:10.1146/annurev.earth.33.092203.122658, 2005.

Stevens, B.: Bulk boundary-layer concepts for simplified models of tropical dynamics, Theor. Comp. Fluid Dyn., 20, 279–304, doi:10.1007/s00162-006-0032-z, 2006.

Stevens, B. and Brenguier, J.-L.: Cloud controlling factors: low clouds. Clouds in the perturbed climate system, Heintzenberg, J. and Charlson, R. J., The MIT Press, Cambridge, Massachusetts, 173-196, 2009.

Stevens, D. E., and Bretherton, C. S.: Effects of resolution on the simulation of stratocumulus entrainment. Quart. J. Roy. Meteor. Soc., 125, 425-439, 1999.

Stevens, B. and Feingold, G.: Untangling aerosol effects on clouds and precipitation in a buffered system, Nature, 461, 607-613, 2009.

Stevens, B., Cotton, W. R., Feingold, G., and Moeng, C.-H.: Large-eddy simulations of strongly precipitating, shallow, stratocumulus-toped boundary layers, J. Atmos. Sci., 55, 3616-3638, 1998.

Stevens, B., Lenschow, D. H., Faloona, I., Moeng, C.-H., Lilly, D. K., Blomquist, B., Vali, G., Bandy, A., Campos, T., Gerber, H., Haimov, S., Morley, B., and Thornton, D.: On entrainment rates in nocturnal marine stratocumulus, Q. J. Roy. Meteorol. Soc., 129, 3469-3493, 2003

S Stevens, B., Moeng, C.-H., Ackerman, A. S., Bretherton, C. S., Chlond, A., De Roode, S., Edwards, J., Golaz, J., Jiang, H., Khairoutdinov, M., Kirkpatrick, M. P., Lewellen, D. C., Lock, A., Muller, F., Stevens, D. E., Whelan, E., and Zhu, P.: Evaluation of large-eddy simulations via observations of nocturnal marine stratocumulus, Mon. Weather Rev., 133, 1443-1462, 2005.

Turton, J. and Nicholls, S.: A study of the diurnal variation of stratocumulus using a multiple mixed-layer model, Q. J. Roy. Meteor. Soc., 113, 969-1011, 1987.

Twomey, S.: The nuclei of natural cloud formation Part 2: The supersaturation in natural clouds and the variation of cloud droplet concentration, Pure Appl. Geophys., 43, 243-249, 1959.

Twomey, S.: The influence of pollution on the shortwave albedo of clouds, J. Atmos. Sci., 34, 1149-1152, 1977.

Tzivion, S., Feingold, G., and Levin, Z.: An efficient numerical solution to the stochastic collection equation, J. Atmos. Sci., 44, 3139-3149, 1987.

Tzivion, S., Feingold, G., and Levin, Z.: The evolution of raindrop spectra ¡V Part II: Collisional collection/breakup and evaporation in a rainshaft, J. Atmos. Sci., 46, 3312-3327, 1989.

Uchida, J., Bretherton, C. S., and Blossey, P. N.:The sensitivity of stratocumulus-capped mixed layers to cloud droplet concentration: do LES and mixed-layer models agree? Atmos. Chem. Phys., 10, 4097-4109, 2010.

Wang, S., Wang, Q., and Feingold, G.: Turbulence, condensation, and liquid water transport in numerically simulated nonprecipitating stratocumulus clouds. J. Atmos. Sci., 60, 262-278, 2003.

Wang, H. and Feingold, G.: Modeling mesoscale cellular structures and drizzle in marine stratocumulus. Part I: Impact of drizzle on the formation and evolution of open cells, J. Atmos. Sci., 66, 3237-3256, 2009a.

Wang, H. and Feingold, G.: Modeling mesoscale cellular structures and drizzle in marine stratocumulus. Part II: The microphysics and dynamics of the boundary region between open and closed cells, J. Atmos. Sci., 66, 3257-3275, 2009b.

Wang, H., Skamarock,W. C., and Feingold, G.: Evaluation of scalar advection schemes in the Advanced Research WRF model using large-eddy simulations of aerosol-cloud interactions, Mon. Weather Rev., 137, 2547–2558, 2009.

Wang, H., Feingold, G., Wood, R., and Kazil, J.: Modelling microphysical and meteorological controls on precipitation and cloud cellular structures in Southeast Pacific stratocumulus, Atmos. Chem. Phys., 10, 6347-6362, 2010.

Warren, S. G., Hahn, C. J., London, J., Chervin, R. M., and Jenne, R. L.: Global distribution of total cloud cover and cloud type amounts over the ocean. NCAR Tech. Note NCAR/TN-317+STR, 42 pp., 1988.

Wood, R., Irons, S., and Jonas, P. R.: How important is the spectral ripening effect in stratiform boundary layer clouds? Studies using simple trajectory analysis, J. Atmos. Sci., 59, 2681– 2693, 2002.

Wood, R.: Cancellation of aerosol indirect effects in marine stratocumulus through cloud thinning, J. Atmos. Sci., 64, 2657-2669, 2007.

Xue, H., and Feingold, G.: Large-eddy simulations of trade wind cumuli: Investigation of aerosol indirect effects. J. Atmos. Sci., 63, 1605-1622, 2006.

Xue, L. and Teller, A. and Rasmussen, R. M. and Geresdi, I., and Pan, Z.: Effects of aerosol solubility and regeneration on warm-phase orographic clouds and precipitation simulated by a detailed bin microphysical scheme, J. Atmos. Sci., doi= {10.1175/2010JAS3511.1, 2010.

Yamaguchi, T., and Randall, D. A.: Large-eddy simulation of evaporatively driven entrainment in cloud-topped mixed layers. J. Atmos. Sci., 65, 1481-1504, 2008.

Table 2.1 Studies of aerosol-cloud interactions in MSc.

	Nighttime			Daytime		Diurnal Mean*
	Non-drizzling	Drizzling		Non-drizzling	Drizzling	
		Light	Moderate/ Heavy		Light	Moderate/ Heavy
Ackerman et al. (2004)		$N_a \uparrow \Longrightarrow$ LWP $\downarrow$ $q_{ft} \downarrow \Longrightarrow$ LWP $\downarrow$	$N_a \uparrow \Longrightarrow P \downarrow \Longrightarrow$ LWP $\uparrow$			
Lu and Seinfeld (2005)		$N_a \uparrow \Longrightarrow$ LWP $\downarrow$ SST $\uparrow \Longrightarrow$ LWP $\downarrow$ $D \uparrow \Longrightarrow$ LWP $\downarrow$	$N_a \uparrow \Longrightarrow P \downarrow \Longrightarrow$ LWP $\uparrow$	$N_a \uparrow \Longrightarrow$ LWP $\downarrow$		
Wood (2007)						$N_a \uparrow \Longrightarrow H \downarrow$ or $\uparrow$
Sandu et al. (2008)			$N_a \uparrow \Longrightarrow P \downarrow \Longrightarrow$ LWP $\uparrow$ $D \uparrow \Longrightarrow$ LWP $\downarrow$ $q_{ft} \downarrow \Longrightarrow$ LWP $\downarrow$		$N_a \uparrow \Longrightarrow$ LWP $\downarrow$ $D \uparrow \Longrightarrow$ LWP $\downarrow$ $q_{ft} \downarrow \Longrightarrow$ LWP $\downarrow$	
Hill et al. (2008, 2009)	$N_a \uparrow \Longrightarrow$ LWP $\downarrow$			$N_a \uparrow \Longrightarrow$ LWP $\downarrow$		
Wang et al. (2010)			$N_a \uparrow \Longrightarrow P \downarrow \Longrightarrow$ LWP $\uparrow$		$N_a \uparrow \Longrightarrow$ LWP $\downarrow$	
Caldwell and Bretherton (2009a)		$N_a \uparrow \Longrightarrow$ LWP $\downarrow$ SST $\uparrow \Longrightarrow$ LWP $\uparrow$				
Summary	$N_a \uparrow \Longrightarrow$ LWP $\downarrow$	$N_a \uparrow \Longrightarrow$ LWP $\downarrow$ SST $\uparrow \Longrightarrow$ LWP $\downarrow$ or $\uparrow$ $D \uparrow \Longrightarrow$ LWP $\downarrow$ $q_{ft} \downarrow \Longrightarrow$ LWP $\downarrow$	$N_a \uparrow \Longrightarrow P \downarrow \Longrightarrow$ LWP $\uparrow$ $D \uparrow \Longrightarrow$ LWP $\downarrow$ $q_{ft} \downarrow \Longrightarrow$ LWP $\downarrow$	$N_a \uparrow \Longrightarrow$ LWP $\downarrow$	$N_a \uparrow \Longrightarrow$ LWP $\downarrow$ $D \uparrow \Longrightarrow$ LWP $\downarrow$ $q_{ft} \downarrow \Longrightarrow$ LWP $\downarrow$	$N_a \uparrow \Longrightarrow H \downarrow$ or $\uparrow$

P is surface precipitation, H is cloud thickness, D is large-scale divergence rate, and q_{ft} is free tropospheric humidity. Light drizzle is defined as surface precipitation rate $<0.1\,\mathrm{mm\,day^{-1}}$, and moderate/heavy drizzle $>0.1\,\mathrm{mm\,day^{-1}}$.
* Wood (2007) uses the downwelling shortwave radiation close to the annual diurnal mean value over the subtropical regions.

Table 2.2 Sign and magnitude of each term in Eq. (2.3) from previous studies.

	$\frac{\Delta(\ln N_d)}{\Delta(\ln N_a)}$	$\frac{\Delta(\ln k)}{\Delta(\ln N_d{}^*)}$	$\frac{\Delta(\ln H)}{\Delta(\ln N_d{}^*)}$	$\frac{\Delta(\ln \tau)}{\Delta(\ln N_a)}$
Measurement	0.6–0.9[a] 0.25–0.85[b]	−0.2[c] −0.14[d]		
LES	0.91[e] (constant LWP)	~0.03 (light drizzle)[f] ~0.2 (heavy drizzle)[f]	$\frac{\partial(\ln LWP)}{\partial(\ln N_a)}$ [e] = −0.1 (clean) −0.03 (polluted)	0.22 (clean)[e] 0.28 (polluted)[e]
Other			cloud base >400 m: thinning[g] cloud base <400 m: thickening[g]	0.28[h]

* Note N_d is applied rather than N_a.
[a] Pruppacher and Klett (1997)
[b] Shao and Liu (2009), based on in situ measurements.
[c] Rotstayn and Liu (2003), including measurements from FIRE, SOCEX, ACE1, ASTEX, SCMS, INDOEX, MAST, etc.
[d] Ackerman et al. (2000)
[e] Lu and Seinfeld (2005): LES based on sounding profiles from FIRE and ASTEX. Note LWP is applied rather than H.
[f] Lu and Seinfeld (2006): LES based on sounding profiles from FIRE and ASTEX.
[g] Wood (2007): obtained by MLM and analytical formulations.
[h] Hill et al. (2009) Table 4.

Table 2.3 Summary of simulated cases.

	N_a (cm^{-3})	Domain (km^2)	SST (K)	q_{ft} ($g\,kg^{-1}$)	D ($10^{-6}\,s^{-1}$)	U, V (ms^{-1})
Control	100, 200, 1000	1×1, 2.5×2.5	288	6.1	5.5	x: −1, y:6
SST290, SST292	100, 1000	1×1	290, 292			
QFT3, QFT1	100, 1000	1×1		3.1, 1.1		
DIV3, DIV8	100, 1000	1×1			3.0, 8.0	
WIND	100, 1000	1×1				x: −4, y:10

Table 2.4 Estimation of aerosol-induced effects on MSc cloud properties from the LES model and of cloud susceptibility from Eq. (2.3) for specific sensitivity simulations under nighttime (4–7 h) and daytime (12–15 h) conditions; aerosol number concentrations considered are 100, 200, 500, and 1000 cm^{-3}.

		$\frac{\Delta(\ln N_d)}{\Delta(\ln N_a)}$		$\frac{\Delta(\ln k)}{\Delta(\ln N_a)}$		$\frac{\Delta(\ln H)}{\Delta(\ln N_a)}$		$\frac{\Delta(\ln \tau)}{\Delta(\ln N_a)}$		$\frac{\Delta(\ln \tau)}{\Delta(\ln N_a)}$ (Eq. 3)	
		Night	Day	Night	Day	Night	Day	Night	Day	Night	Day
Control	Mean	1.077	1.158	0.072	0.094	−0.014	−0.126	0.350	0.261	0.360	0.207
	Stdev	0.049	0.029	0.016	0.030	0.010	0.034	0.035	0.104		
SST290	Mean	1.000	0.805	0.036	0.050	−0.038	−0.346	0.280	−0.358	0.282	−0.292
	Stdev	0.023	0.086	0.010	0.023	0.007	0.160	0.018	0.370		
QFT3	Mean	1.000	1.037	0.026	0.070	−0.026	−0.120	0.291	0.165	0.299	0.169
	Stdev	0.010	0.025	0.006	0.036	0.016	0.011	0.026	0.039		
DIV3	Mean	1.245	1.370	0.150	0.082	0.014	−0.005	0.528	0.625	0.488	0.476
	Stdev	0.128	0.070	0.047	0.018	0.013	0.050	0.120	0.154		

Table 2.5 Values of environmental variables.

Variable	Values
SST (K)	288, 290, 292
q_{ft} ($g\,kg^{-1}$)	1.1, 3.1, 6.1
D ($10^{-6}\,s^{-1}$)	3.0, 5.5, 8.0

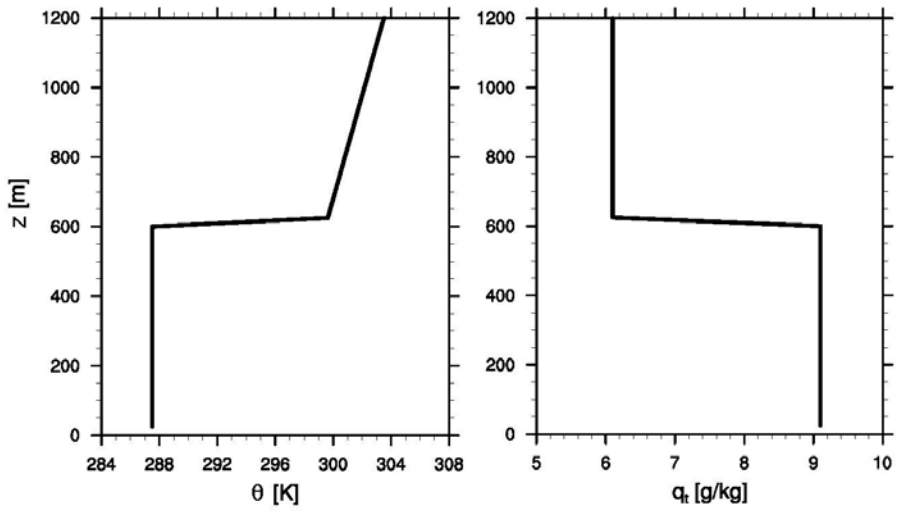

Figure 2.1 Initial sounding profile (potential temperature θ and total water mixing ratio q_t) for the MSc of Control case.

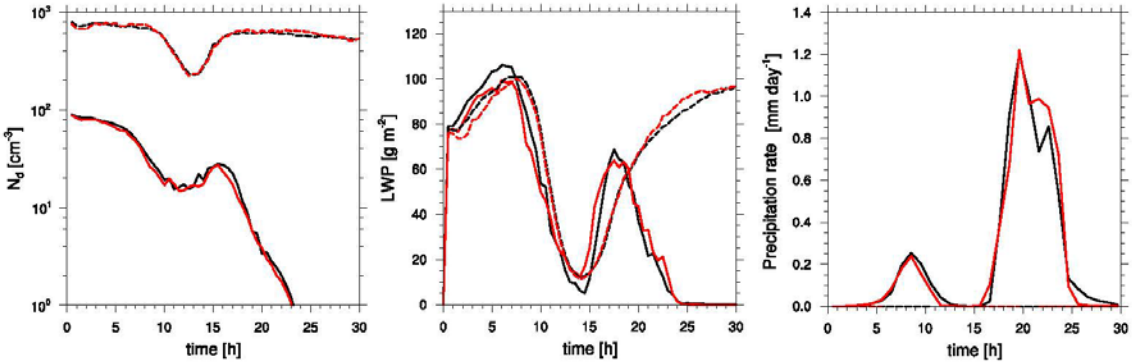

Figure 2.2 Time evolution of N_d, LWP, and surface precipitation rate under different domain size: 2.5×2.5 km^2 (black) and 1×1 km^2 (red); under different N_a: clean (solid line) and polluted (dashed line) cloud.

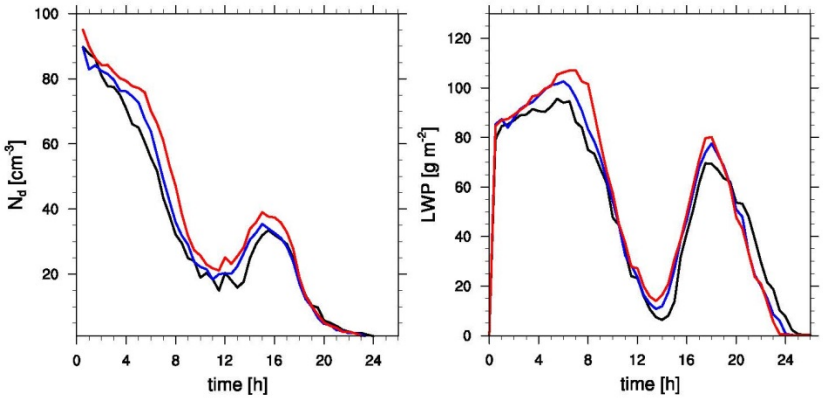

Figure 2.3 Time evolution of N_d and LWP under different vertical spacing: 20m (black), 10m (blue), and 5m (red) for clean condition.

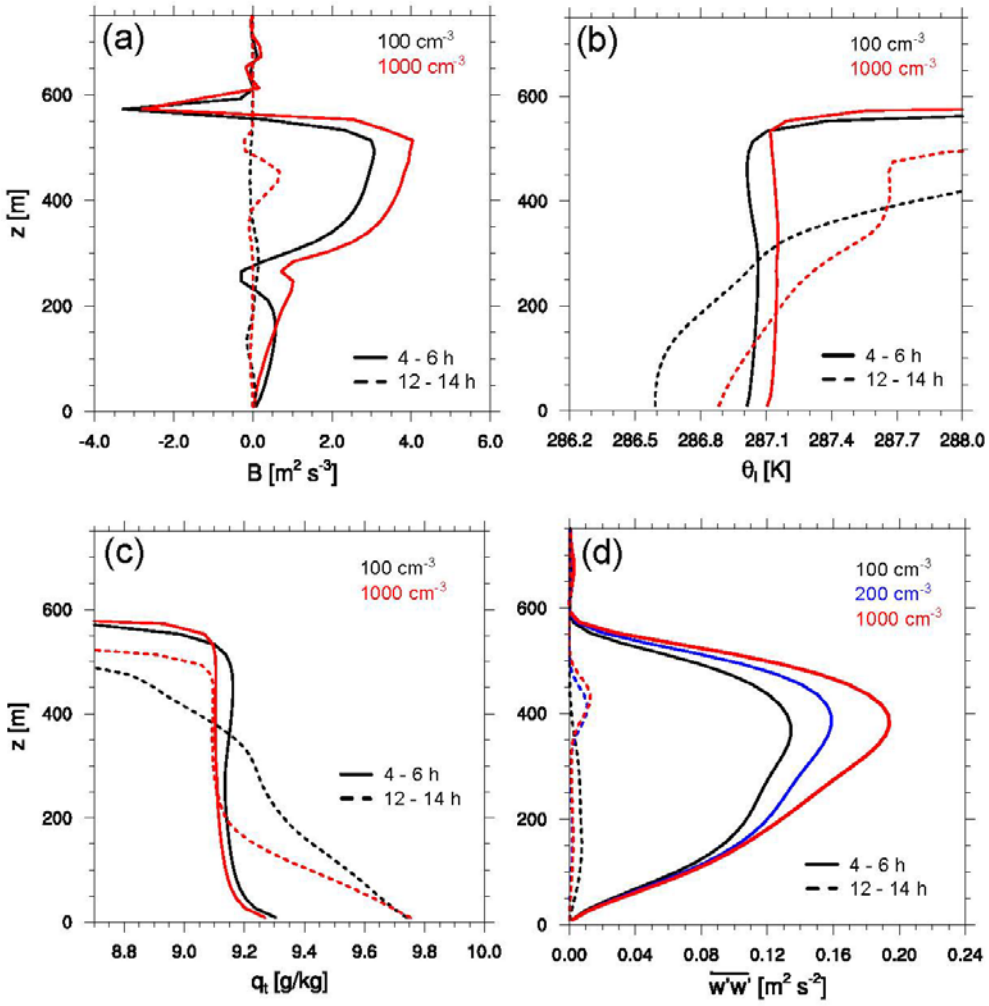

Figure 2.4 Vertical profile averaged over 4–6 h (solid line) and 12–14 h (dashed line) of **(a)** mean buoyancy flux, $B = \frac{g}{\theta_v}\overline{w'\theta_v'} \times 10^{-4}$, where θ_v is virtual potential temperature, **(b)** mean liquid water potential temperature θ_l , **(c)** mean total water mixing ratio q_t , and **(d)** mean vertical velocity variance of clean (black), semi-polluted (blue), and polluted (red) cloud.

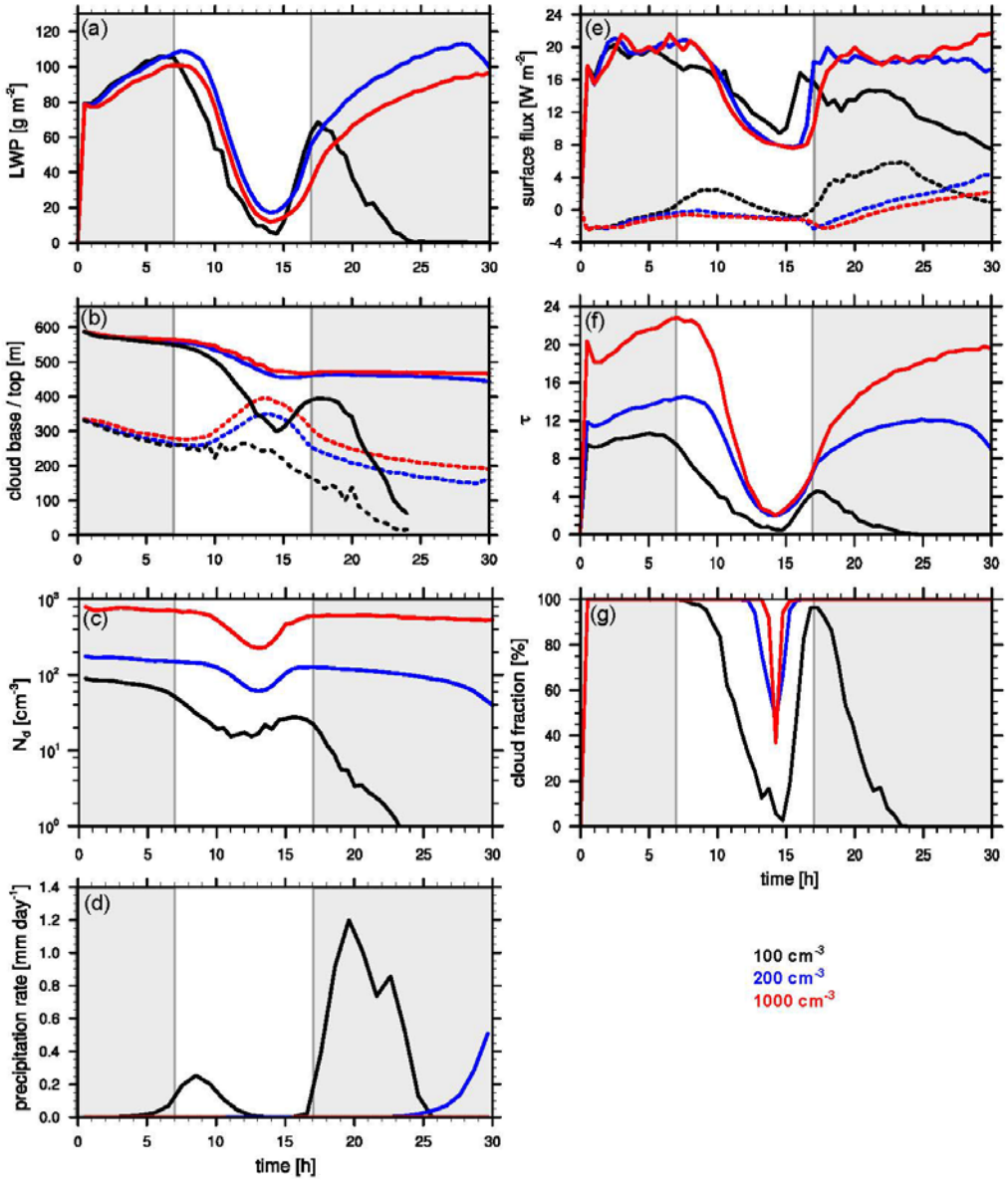

Figure 2.5 Time evolution of clean (N_a = 100 cm^{-3}, black), semi-polluted (N_a = 200 cm^{-3}, blue), and polluted (N_a = 1000 cm^{-3}, red) cloud (2.5×2.5 km^2 horizontal domain): **(a)** average LWP; **(b)** average cloud top (solid line) and cloud base (dashed line) height, where the cloudy grid is defined as grid with cloud water mixing ratio > 0.01 g kg^{-1}; **(c)** cloud droplet number concentration N_d, averaged over the cloudy grid; **(d)** surface precipitation rate, hourly averaged; **(e)** domain average surface latent (solid line) and sensible (dashed line) heat flux; **(f)** average cloud optical depth; **(g)** cloud fraction, defined by cloud optical depth > 2. Gray regions are for the nighttime conditions (0–7 h and 17–30 h), while write regions are for the daytime conditions (7–17 h).

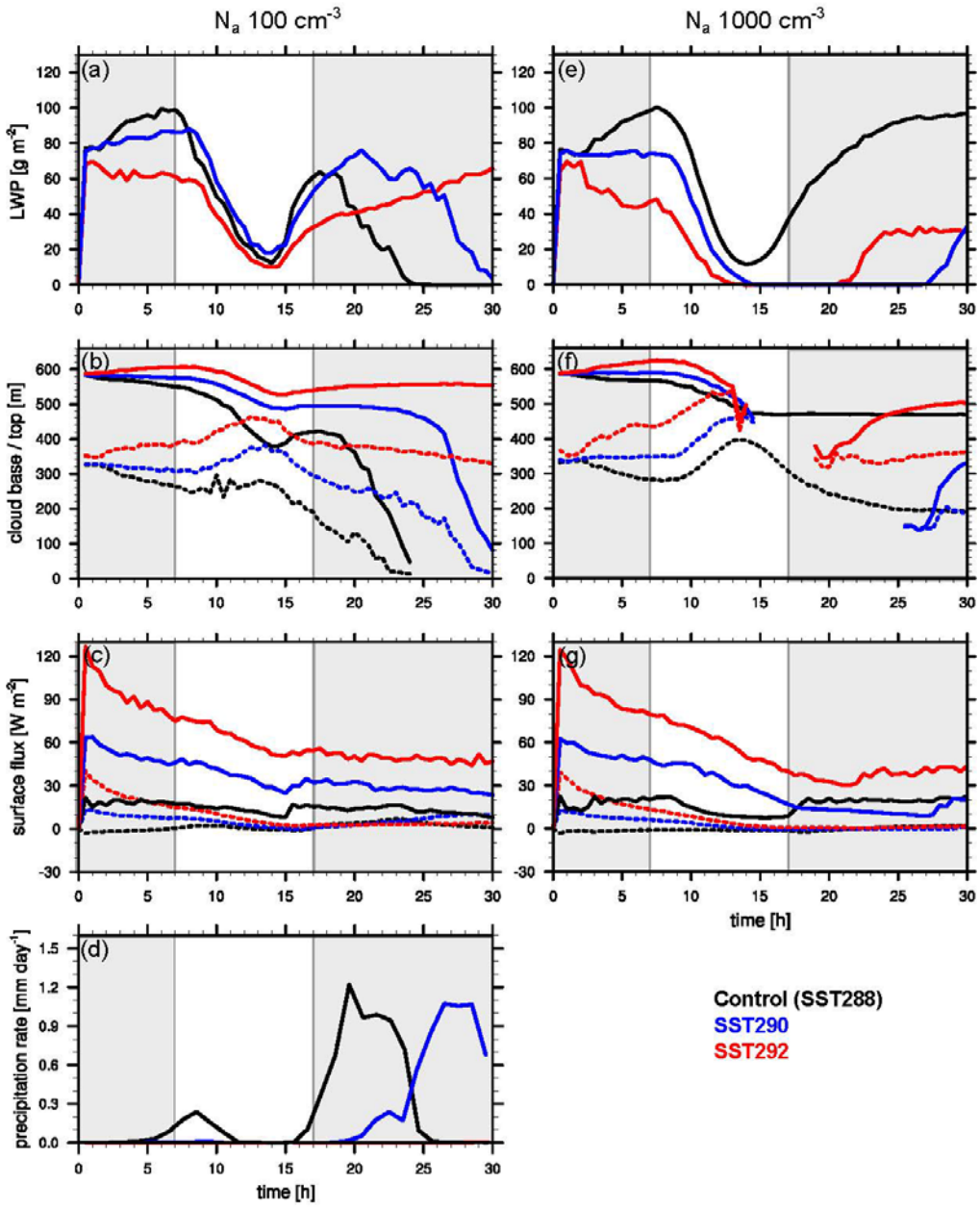

Figure 2.6 Time evolution of 1×1 km^2 clean (N_a =100 cm^{-3}, left column) and polluted (N_a =1000 cm^{-3}, right column) cloud for Control (black), SST290 (blue) and SST292 (red) case: **(a)** and **(e)** average LWP; **(b)** and **(f)** average cloud top/base height; **(c)** and **(g)** domain average surface latent (solid line) and sensible (dashed line) heat flux; **(d)** surface precipitation rate, hourly averaged.

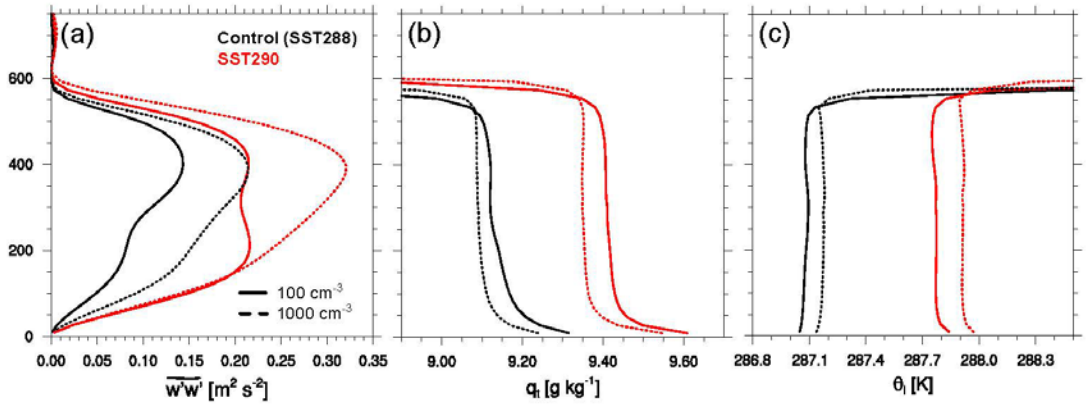

Figure 2.7 Vertical profile averaged over 4–6 h of **(a)** mean vertical velocity variance, **(b)** mean total water mixing ratio q_t, and **(c)** mean liquid water potential temperature θ_l for Control (black)/SST290 (red) and clean (solid line)/polluted (dashed line) case.

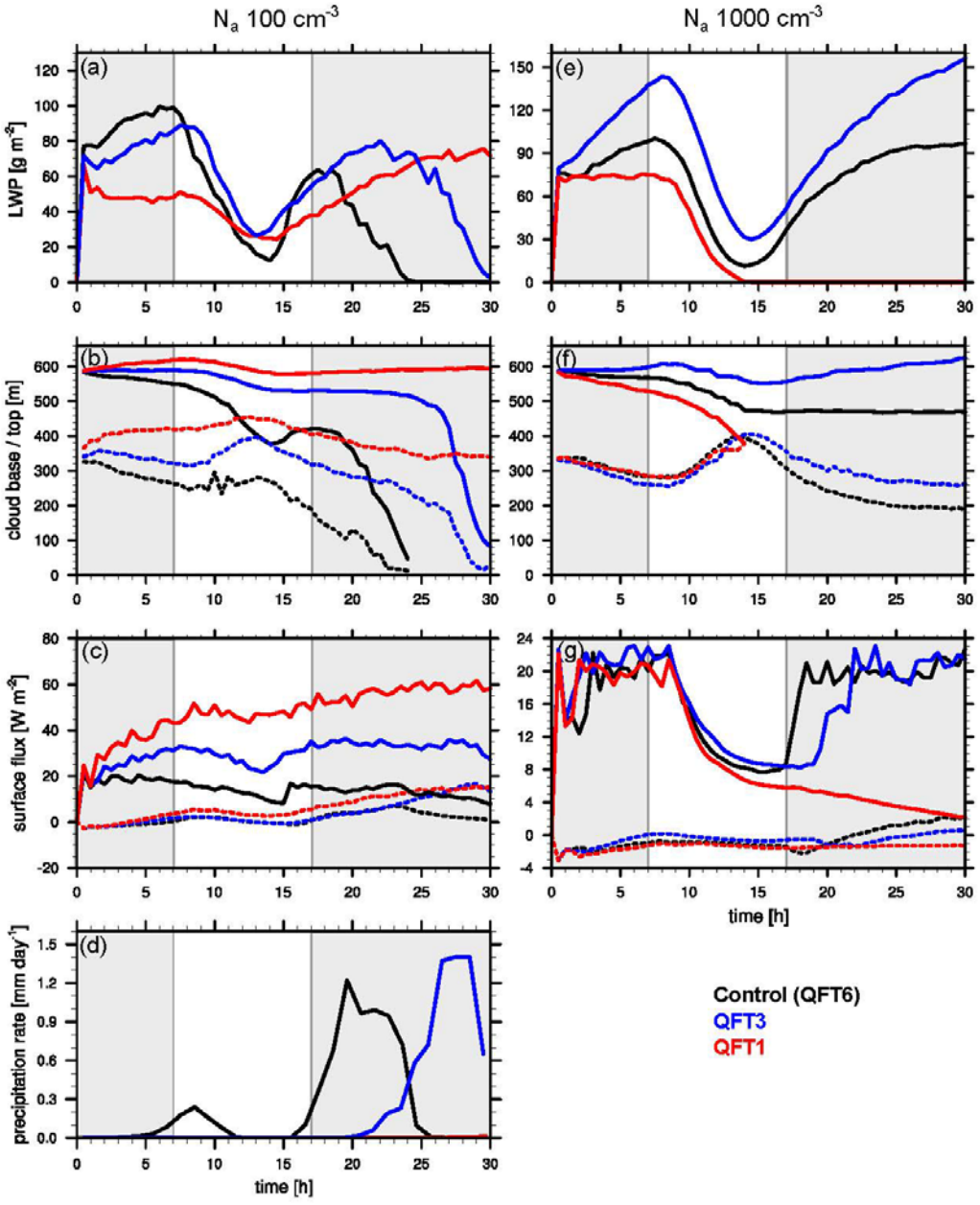

Figure 2.8 The same as Fig. 2.6, except for Control (black), QFT3 (blue) and QFT1 (red) case.

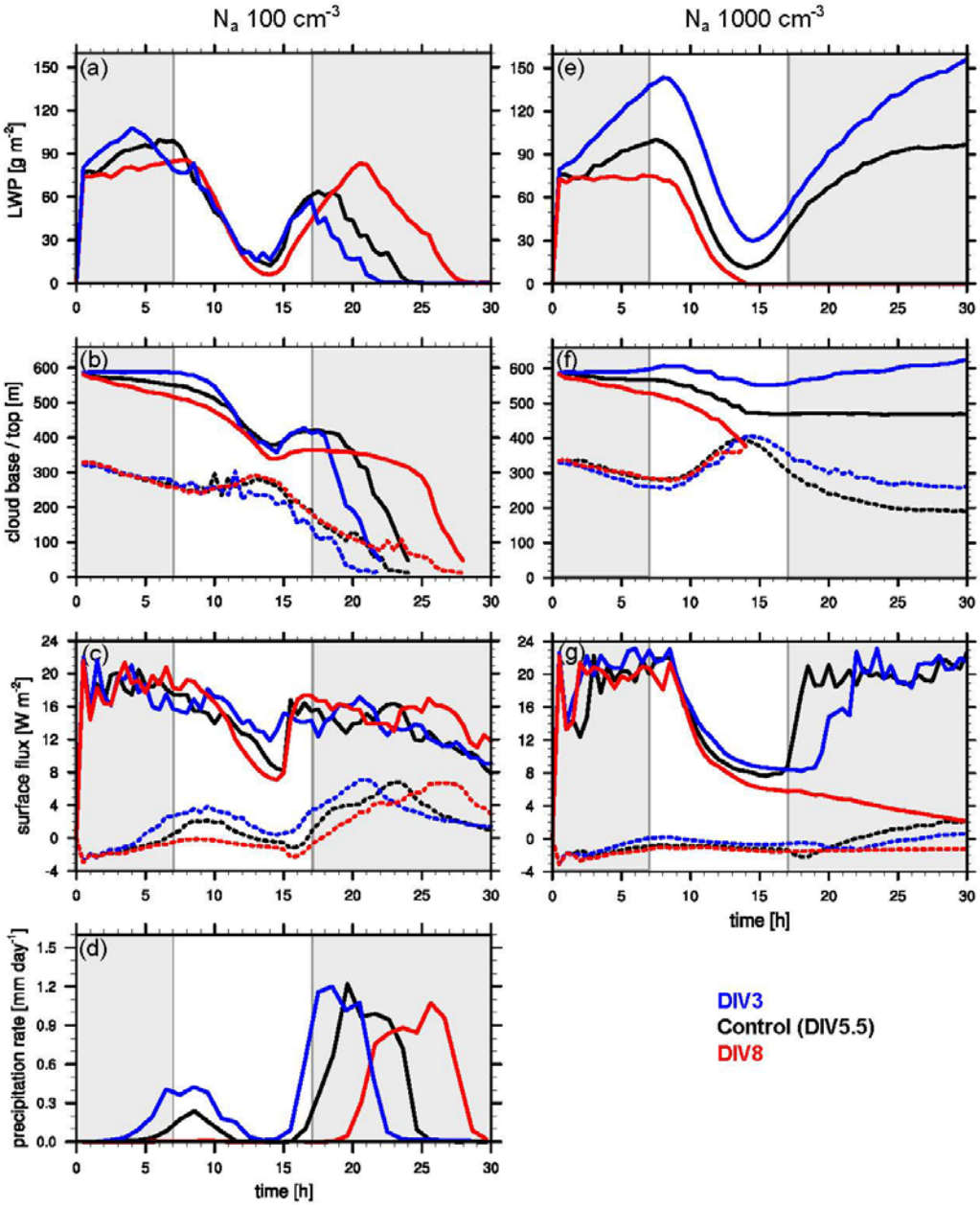

Figure 2.9 The same as Fig. 2.6, except for Control (black), DIV3 (blue) and DIV8 (red) case.

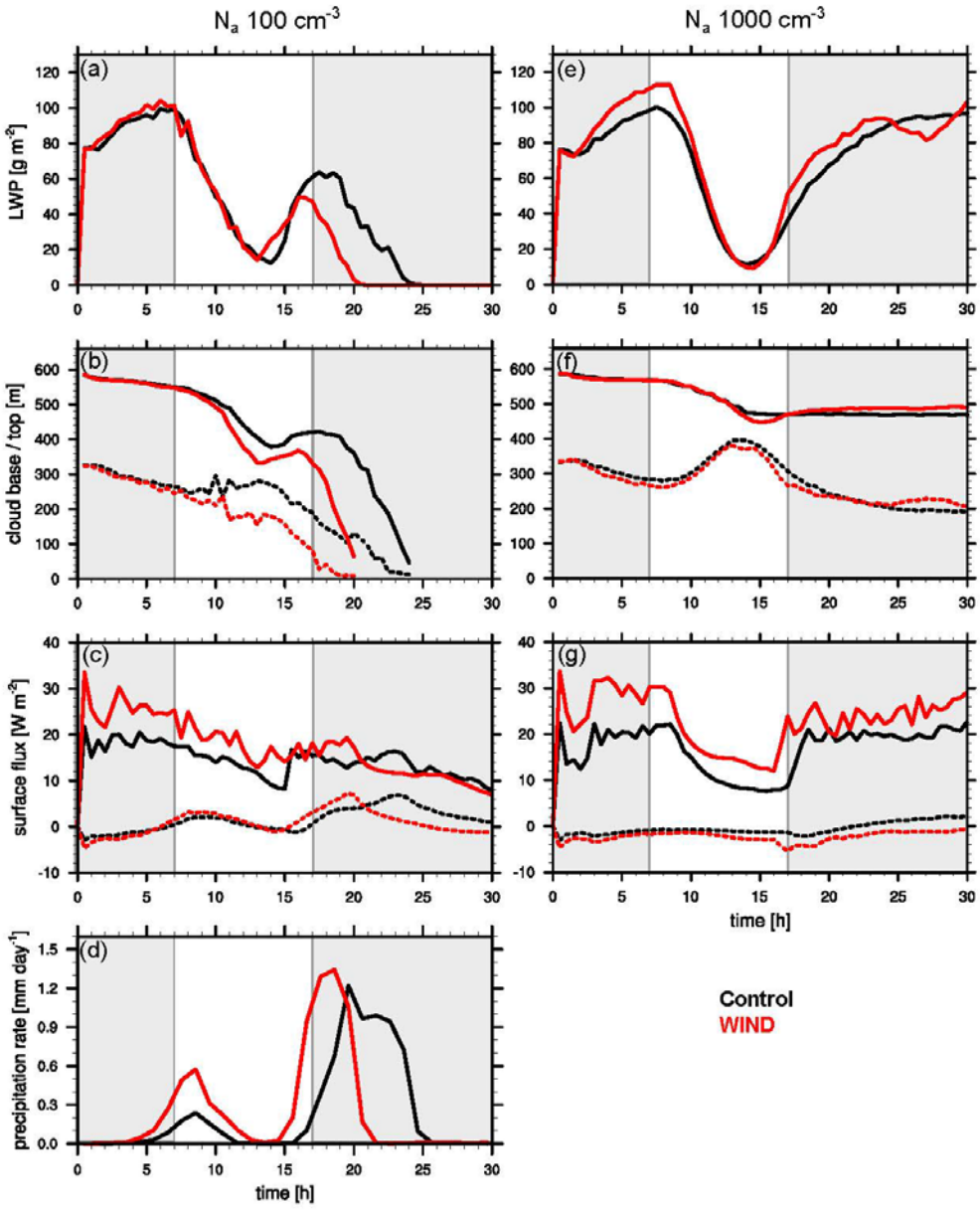

Figure 2.10 The same as Fig. 2.6, except for Control (black) and WIND (red) case.

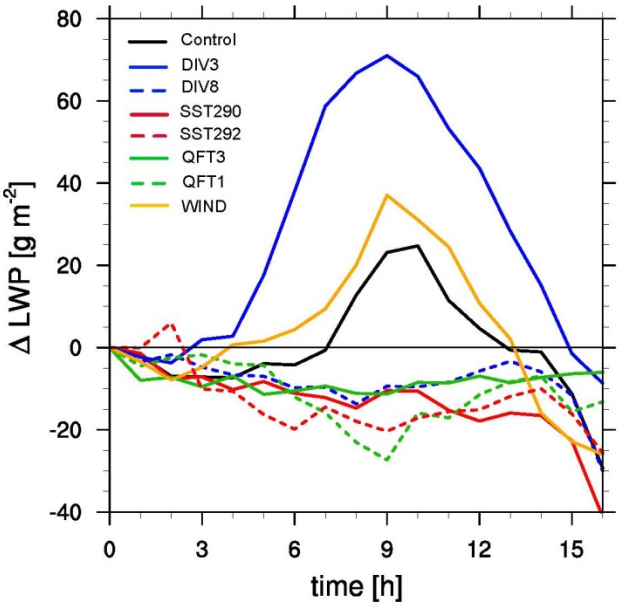

Figure 2.11 Time evolution of LWP difference between polluted and clean condition for Control (black), SST290 (red solid), SST292 (red dashed), QFT3 (green solid), QFT1 (green dashed), DIV3 (blue solid), DIV8 (blue dashes), and WIND (orange) case.

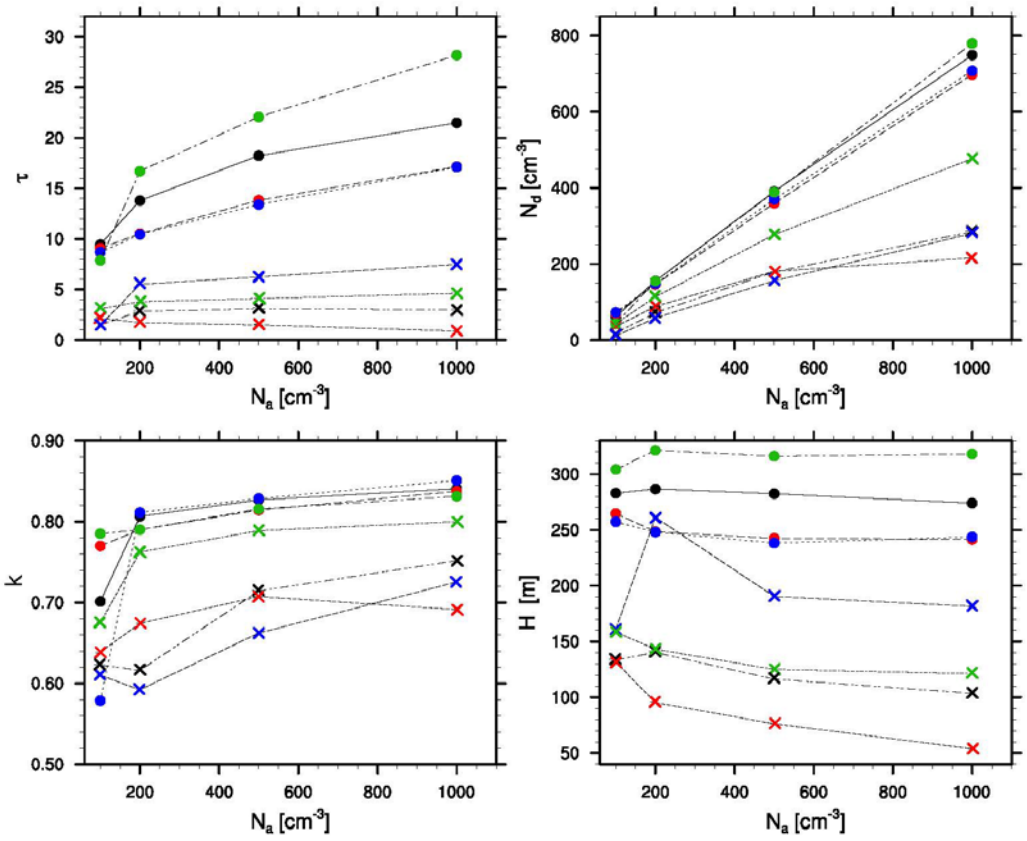

Figure 2.12 Averaged optical depth (τ), cloud droplet number concentration (N_d), dispersion coefficient (k) and cloud thickness (H) as a function of aerosol number concentration N_a. Values are averaged horizontally and vertically between cloud top and base for Control (black), SST290 (red), QFT3 (blue), and DIV3 (green) cases during nighttime (averaged over 4–7 h, filled circle) and daytime (average over 12–15 h, cross).

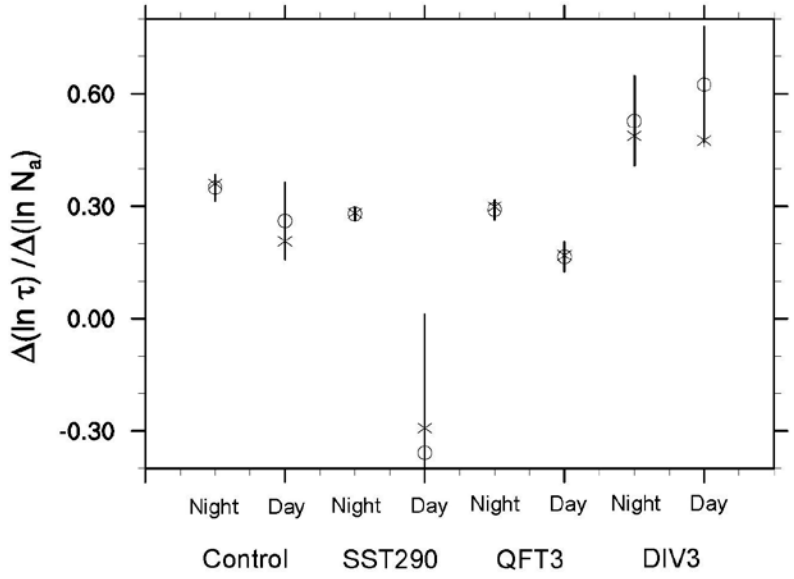

Figure 2.13 Averaged $\Delta(\ln\tau)/\Delta(\ln N_a)$ from the LES model (unfilled circle) and Eq. (2.3) (asterisk) for specific sensitivity simulations under nighttime (4–7 h) and daytime (12–15 h), as shown in last two columns of Table 2.4. The error bar (standard deviation) is computed from LES experiments.

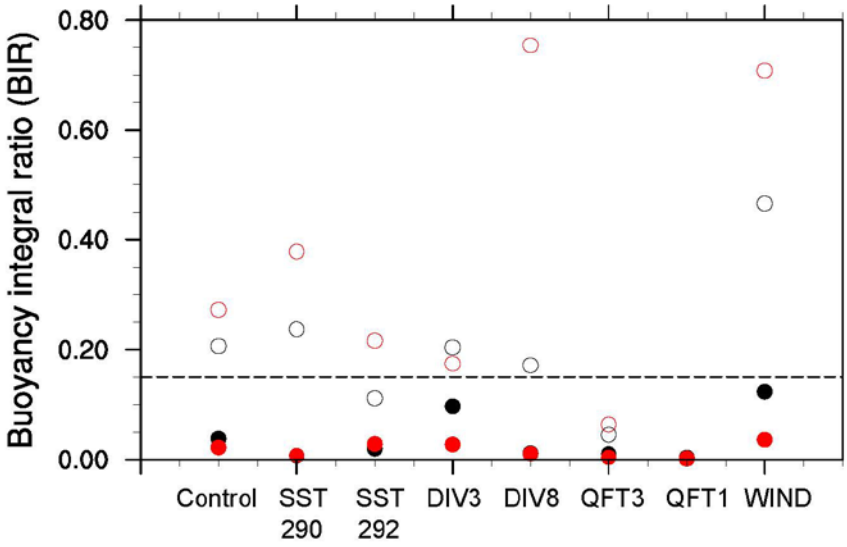

Figure 2.14 The buoyancy integral ratio (BIR) for clean (N_a = 100 cm^{-3}) nighttime (4–7 h, black), clean daytime (12–15 h, black open circle), polluted (N_a =1000 cm^{-3}) nighttime (red), and polluted daytime (red open circle) clouds under different environmental conditions. The dashed line corresponds to critical value 0.15 (suggested by Bretherton and Wyant (1997)).

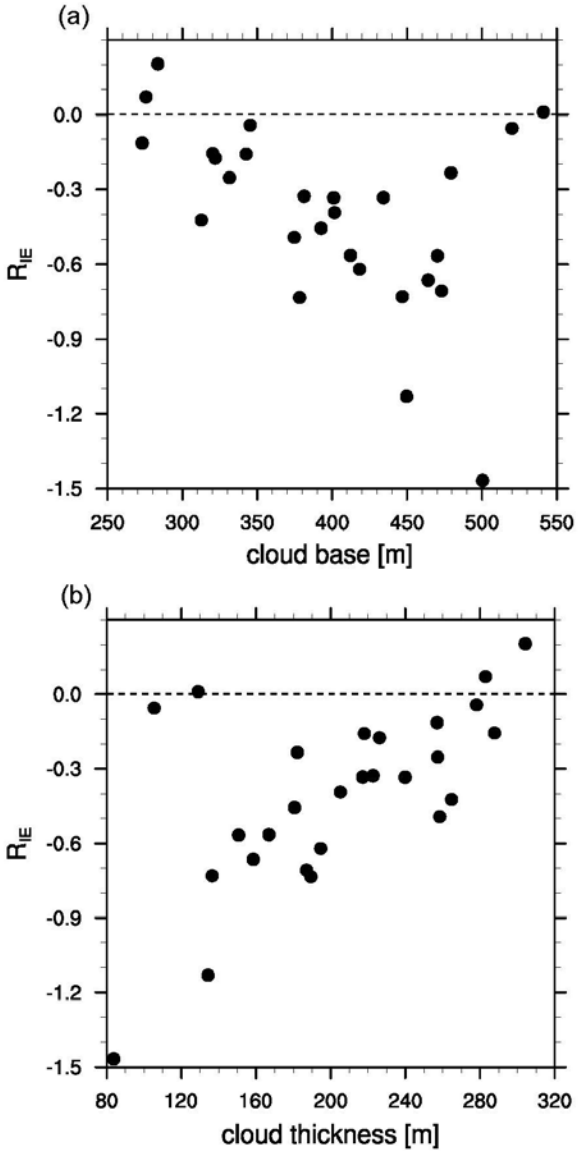

Figure 2.15 The mean ratio of second to first indirect effect (RIE) for N_a from 100 to 200 cm^{-3} as a function of **(a)** cloud base height, and **(b)** cloud thickness. The data points are averaged over 4–7 h.

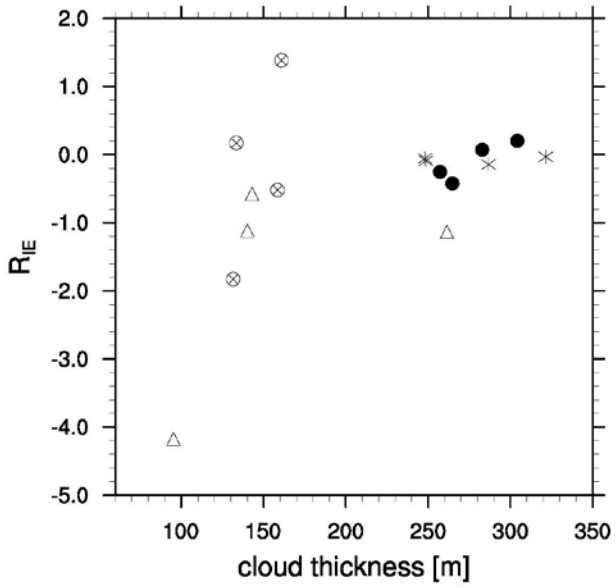

Figure 2.16 The mean ratio of second to first indirect effect (RIE) for N_a from 100 to 200 cm^{-3} during nighttime (4–7 h, black filled circle) and daytime (12–15 h, circle with cross inside), and from 200 to 1000 cm^{-3} during nighttime (asterisk) and daytime (triangle).

Chapter 3

Occurrence of Lower Cloud Albedo in Ship Tracks

Published in *Atmospheric Chemistry and Physics*: Chen, Y.-C., Christensen, M. W., Xue, L., Sorooshian, A., Stephens, G. L., Rasmussen, R. M., and Seinfeld, J. H.: Occurrence of lower cloud albedo in ship tracks, Atmos. Chem. Phys., 12, 8223–8235, doi:10.5194/acp-12-8223-2012, 2012

3.1 Abstract

The concept of geoengineering by marine cloud brightening is based on seeding marine stratocumulus clouds with sub-micrometer sea-salt particles to enhance the cloud droplet number concentration and cloud albedo, thereby producing a climate cooling effect. The efficacy of this as a strategy for global cooling rests on the extent to which aerosol-perturbed marine clouds will respond with increased albedo. Ship tracks, cloud regions impacted by ship exhaust, are a well-known manifestation of the effect of aerosol injection on marine clouds. We present here an analysis of the albedo responses in ship tracks, based on in situ aircraft measurements and three years of satellite observations of 589 individual ship tracks. We show that the sign (increase or decrease) and magnitude of the albedo response in ship tracks depends on the mesoscale cloud structure, the free tropospheric humidity, and cloud top height. In closed cell cloud (cloud cells ringed by a perimeter of clear air), nearly 30% of ship tracks exhibited a decreased albedo. Detailed cloud responses must be accounted for in global studies of the potential efficacy of sea-spray geoengineering as a means to counteract global warming.

3.2 Introduction

Marine stratocumulus clouds (MSc), covering, on average, nearly one-third of the ocean surface (Warren et al., 1988), exert a cooling influence on climate. It has been estimated that a 6% increase of the albedo of MSc would offset the warming by atmospheric CO_2 doubling (Latham et al., 2008). Based on the assumption that increasing aerosol number concentration leads to higher cloud droplet number concentration and an increase in cloud albedo (Twomey, 1991) (assuming constant LWP), a marine geo-engineering scheme was proposed (Salter et al., 2008): using wind-driven spray-vessels that pump sub-micrometer sea-salt particles into the air beneath MSc. The effect of injecting aerosols into the marine boundary layer has been evaluated in several global climate modeling studies with prescribed enhanced cloud droplet number concentration (Jones et al., 2009; Rasch et al., 2009; Bala et al., 2011), global aerosol microphysics models (Korhonen et al., 2010; Partanen et al., 2012; Pringle et al., 2012), parcel models (Russell et al.,1999; Bower et al., 2006), and cloud-system resolving models (Wang et al., 2011) to investigate the effectiveness of cloud brightening.

According to IPCC (2007), the median value of global aerosol indirect radiative forcing is -0.7 Wm^{-2}, with an uncertainty range from -1.8 to -0.3 Wm^{-2}. Modeling the global aerosol indirect effect is challenging because the representations of aerosol-cloud interactions in climate models are crude (Lohmann and Feichter, 2005). Parameterizations that relate cloud droplet number concentration to aerosol number concentration exhibit considerable variations in the effect of microphysical changes on cloud optical properties. The common premise that clouds and precipitation are strongly sensitive to aerosol perturbations neglects the mechanisms that buffer the effects of aerosol perturbations (Stevens and Feingold, 2009). Also, as both aerosol and meteorology (i.e., large-scale dynamic and thermodynamic state) govern the cloudiness, the intertwining of these two factors complicates the interpretation of data (Stevens and Brenguier, 2009).

Ship tracks serve as a prominent manifestation of marine aerosol-cloud interactions. There have been a number of observational studies of ship tracks, including in-situ airborne measurements (e.g., Radke et al., 1989; Ferek et al., 1998; Durkee et al., 2000; Twohy et al., 2005; Lu et al., 2007, 2009) and remote sensing satellite observations (e.g., Coakley and Walsh, 2002; Schreier et al., 2007; Segrin et al., 2007; Lebsock et al., 2008; Christensen and Stephens, 2011, 2012). Whereas ample evidence exists that increased aerosol levels lead to more numerous and smaller cloud droplets, the response of cloud macrophysics (i.e., cloud thickness, LWP) to aerosol perturbations is not as clear-cut. Cloud macrophysical responses to increased aerosol levels can lead to either enhancement or diminution of cloud brightening. One of the challenges in understanding the cloud macrophysical responses lies in untangling the aerosol effects from others such as meteorological conditions. By utilizing both in situ aircraft measurements and A-Train satellite data, we present here an analysis of the factors that control the sign and magnitude of the aerosol indirect effect in ship tracks.

3.3 Data Description

3.3.1 In-situ E-PEACE data description

The Eastern Pacific Emitted Aerosol Cloud Experiment (E-PEACE) aircraft campaign, carried out in July and August 2011 (30 research flights) over the eastern Pacific adjacent to the coast of Monterey, California, was designed to provide a well-defined data set on MSc

responses to ship emissions (Russell et al., 2012). This area of widespread ship traffic is characterized by layers of persistent stratocumulus clouds. The Center for Interdisciplinary Remotely-Piloted Aircraft Studies (CIRPAS) Twin Otter aircraft was employed, with a full payload of state-of-the-art aerosol and cloud instrumentation (Table 3.1). In the E-PEACE campaign, three types of particle sources were used as cloud perturbations: (a) combustion exhaust from large container/tanker vessels (dry diameters 50–100 nm); (b) organic smoke generated onboard the Research Vessel Point Sur (dry diameters 100 nm–1 μm); and (c) aircraft-emitted milled salt particles (dry diameters 3–5 μm). The present work focuses on the effect of combustion exhaust from large container/tanker ships. Over 30 flights, approximately 45 cargo and tanker ships were probed. Several flight strategies were applied. In most flights, the aircraft executed a zigzag pattern in and out of the plume, with below cloud, in-cloud (cloud base, mid-cloud, cloud top), and above cloud legs. In four of the flights, spiral soundings and/or slanted ascents (Fig. 3.1) were conducted in areas clearly influenced by the ship exhaust and in adjacent areas relatively free of ship exhaust, from which the cloud base/top heights, LWP, and cloud albedo, using the vertical boundary layer profile, were obtained. This strategy of spiral sounding and slanted ascents proved ideal to probe the response of cloud properties with respect to ship-emitted particles: ship exhaust and background marine aerosol below cloud, in cloud, and above cloud were probed, with the perturbed clouds subject to the same background meteorological conditions as those outside the region of exhaust impact. We focus here on these four research flights during E-PEACE.

In situ measurements are subject to a variety of uncertainties and limitations. The measurement uncertainty of the probes is documented in several studies (e.g., Baumgardner et al., 2001; Conant et al., 2004; Lance et al., 2010). The probes were repeatedly calibrated during the E-PEACE field mission. The aerosol number concentration (N_a) was measured by a condensation particle counter (CPC) and a passive cavity aerosol spectrometer probe (PCASP). Cloud droplet size distributions were measured by the cloud, aerosol, and precipitation spectrometer (CAPS), and cloud droplets are defined as those with radius greater than 1.77 μm but smaller than drizzle droplets. Drizzle drop size distribution was measured using the Cloud-Imaging Probe (CIP, included in the CAPS package, with size range from 15 μm to 1.6 mm), and drizzle drops are defined as those with radius greater than 20 μm. These values (radius 1.77 and 20 μm) were chosen based on the particle size

range of each measuring bin. Cloud droplet is defined as drops with radius larger than 2 μm (e.g., Chen et al., 2011), and the corresponding size bin in CAPS is between 1.77 and 2.35 μm in radius. Therefore 1.77 μm was chosen as the threshold of cloud droplet size. For drizzle drops, the cutoff radius between cloud and drizzle drops is defined as 25 μm (e.g., Wang and Feingold, 2009). The closest size bin in CIP is that ranging from ~20 to 32 μm, with 25 μm being the geometric mean. Thus 20 μm was chosen as the lowest boundary of drizzle drops. The cloud base and top are defined with cloud droplet number concentration (N_d) threshold > 10 cm^{-3} and liquid water content (LWC) > 0.01 g m^{-3}. LWC is calculated by $LWC = \int \frac{4}{3}\pi\rho_w r^3 n(r)dr$, where ρ_w is density of water, r is droplet radius, and $n(r)$ is the droplet number concentration distribution. And $\mathrm{LWP} = \sum[z(i+1) - z(i)] \times \frac{[LWC(i+1)+LWC(i)]}{2}$, where $z(i)$ is the altitude from cloud base ($i = 1$) to cloud top. The cloud effective radius (R_e), it is calculated using $R_e = \int r^3\, n(r)dr / \int r^2\, n(r)dr$.

With the drizzle drop size distribution, the rain rate (mm day^{-1}) is calculated by Zhao et al. (2011): $R = 24 \times 0.6\pi \times 10^{-3} \int_{D_{min}}^{D_{max}} D^3 v(D) n(D) dD$, where D is the raindrop diameter, and $v(D)$ is the droplet terminal velocity (m s^{-1}), determined by $v(D) = 3.778 \times D^{0.67}$ (Zhang et al., 2001). The cloud base rain rate is averaged over the lower quarter of the cloud depth.

Using the cloud droplet spectra, the cloud optical depth, τ, is calculated by

$$\tau = \iint 2\,\pi r^2 n(r) dr dz \qquad (3.1)$$

where the extinction efficiency at visible wavelength is approximately 2 in the geometric optics limit for typical cloud droplet sizes, r is droplet radius, and $n(r)$ is the droplet number concentration distribution. The approximate cloud albedo, A, is calculated using A=τ/(τ+7.7).

Under adiabatic conditions, a relationship between cloud optical depth and cloud droplet number concentration, N_d, can be expressed as (Brenguier et al., 2000):

$$\tau = \frac{9}{10} \left(\frac{4}{3}\pi\right)^{1/3} {l_0}^{2/3} (k\, N_d)^{1/3}\; H^{5/3} \qquad (3.2)$$

where $l_0 = \frac{C_w}{\rho_w}$, ρ_w is the density of water, C_w is the moist adiabatic condensation coefficient, ranging from 1 to 2.5×10^{-3} gm^{-4} for temperatures between 0°C and 40°C (Brenguier et al., 2000); k is a parameter inversely proportional to the droplet distribution breadth (unitless), approaching 0 for a very wide droplet spectrum and 1 for a monodisperse droplet population; and H is cloud thickness. The assumption of adiabatic conditions in Eq. (3.2) may not be appropriate for heavy drizzling clouds and/or partly cloudy (i.e., open cell cloud) conditions (e.g., Hayes et al., 2010). Comparison of cloud albedo susceptibility using Eqs. (3.1) and (3.2) will be investigated to evaluate the effect of the adiabatic assumption. From the approximate cloud albedo, $A=\tau/(\tau+7.7)$, one obtains $\frac{dA}{d\tau} = \frac{A(1-A)}{\tau}$. Together with the equation above, the susceptibility of cloud albedo to a perturbation in cloud droplet number concentration can be approximated as:

$$\frac{dA}{dN_d} = \frac{A(1-A)}{3N_d}\left(1 + \frac{dlnk}{dlnN_d} + 5\frac{dlnH}{dlnN_d}\right) . \qquad (3.3)$$

The first term on the R.H.S. of (3) represents the so-called Twomey effect, the second term is the dispersion effect (i.e., effect of changes in N_a on the cloud droplet size distribution), and the third term expresses the sensitivity of cloud thickness to aerosol perturbations. The cloud thickness response, which can be either positive or negative, is determined by the balance between (a) the moistening/cooling of the marine boundary layer resulting from precipitation suppression, and (b) drying/warming resulting from enhanced entrainment due to increased turbulence (Ackerman et al., 2004; Wood, 2007). Precipitation suppression does not always lead to moistening of the MSc; under certain conditions, it can enhance entrainment and lead to cloud thinning. The three effects represented in Eq. (3.3) are the major ones governing the response of cloud albedo to a perturbation in cloud droplet number concentration. As an increase in emitted aerosol particles can lead to an increase in N_d (the strength of which depends on background aerosol number concentration, particles acting as cloud condensation nuclei, etc.), Eq. (3.3) can be applied to the ship exhaust observations, expressing the change between the unperturbed clouds, subject only to the marine background aerosol number concentration (thus background N_d), and those perturbed by ship exhaust.

For the dispersion effect, the coefficient k is calculated following Lu and Seinfeld (2006) as a function of relative dispersion (d) and skewness (s) of the droplet number concentration distribution $n(r)$, $k = \frac{(1+d^2)^3}{(sd^3+1+3d^2)^2}$, where $d = \sigma/\bar{r}$, $\bar{r}$ is mean droplet radius, σ is the standard deviation of droplet spectrum, given by $\sigma = (\frac{1}{N_d}\int(r-\bar{r})^2 n(r)dr)^{1/2}$, and skewness s is defined as $s = \frac{1}{\sigma^3 N_d}\int(r-\bar{r})^3 n(r)dr$.

3.3.2 A-Train satellite data description

The A-Train satellite observations stemmed from the framework of Christensen and Stephens (2012). Using 1-km MODIS imagery over regions on the globe where MSc are prevalent (e.g., the North Pacific Ocean, and adjacent to the coasts of South America and South Africa), ship tracks during the period June 2006–December 2009 were meticulously logged by hand. Polluted and nearby unpolluted clouds identified from MODIS images were co-located to the closest observation from the Cloud-Aerosol Lidar with Orthogonal Polarization (CALIOP) and cloud profiling radar (CPR) on CloudSat. Droplet effective radius and cloud optical thickness were derived from the 3.7-μm reflectances and obtained using the MODIS cloud product (MYD06, King et al., 1998). One-kilometer pixels were screened to include only those with full cloud coverage and fitting the requirement of a single layer, low-level (cloud top pressure greater than 600 hPa), and warm phase cloud. The screening criteria are similar to those applied in Christensen and Stephens (2012). Cloud albedo was calculated using BUGSrad (Stephens et al., 2001), a two-stream radiative transfer model. LWP was derived from the effective radius and optical depth through $LWP = (2/3)\rho_w r_e$ (Stephens, 1978), assuming that the cloud contains spherical droplets and that liquid water content follows an adiabatic vertical profile. These assumptions lead to 30% error at the pixel scale, as derived from Bennartz (2007). Therefore, numerous pixels, a minimum of 30 for a ship track, were grouped together into segments to reduce the uncertainty, thereby producing a more representative average of the cloud optical properties derived from MODIS.

In total, 589 ship tracks were identified. Clouds were classified subjectively as closed cell, open cell, unclassifiable, or others (rolled, wavy, streets, etc.) by visually inspecting the region of clouds in a MODIS image (0.64-μm channel) surrounding the ship track. An

automated pixel identification scheme, outlined in Christensen and Stephens (2012), was applied to each ship track domain in order to isolate the 1-km MODIS pixels in the ship track from the surrounding unpolluted clouds. Segments, 30-km in length, containing a number of pixels were used to construct reasonably representative averages of the cloud optical properties derived from MODIS for the polluted and unpolluted portions of ship track domains.

3.4 Results

3.4.1 Cloud Response in Ship Tracks: In situ Observations

During four of the research flights (RF18, 19, 20, and 24) with ideal conditions, the detailed response of cloud properties with respect to ship-emitted particles were probed. In each case, the clouds showed marked differences in the microphysical (e.g., effective radius) and macrophysical properties between the unperturbed clouds (in the absence of ship emissions) and those impacted by ship plumes. The perturbed clouds exhibited higher cloud droplet number concentration, N_d, and smaller R_e (Table 3.2 and Fig. 3.2), consistent with findings in past field studies of ship tracks (e.g., Radke et al., 1989; Hudson and Yum, 1997; Durkee et al., 2000; Brenguier et al., 2000; Twohy et al., 2005; Lu et al., 2007).

During RF20 (Aug. 4, 2011), the clouds were heavily drizzling (Table 3.2). The presence of heavy drizzle produced an open-cell-like cloud structure (i.e., open spaces ringed by cloud edges, Fig. 3.3a). Previous studies (Stevens et al., 2005; VanZanten and Stevens, 2005; Savic-Jovcic and Stevens, 2008; Wang and Feingold, 2009) have shown that appreciable precipitation can lead to patchy, scattered cloud, associated with open cellular structures. In the presence of heavy drizzle and solar heating, drizzle evaporation below cloud base and solar absorption tend to promote a stable density stratification within the marine boundary layer (e.g., Stevens et al., 1998; Lewellen and Lewellen, 2002). In the cloud region impacted by the injection of ship exhaust, significant increases in cloud thickness (Clean = 252 m, Ship = 344 m) and LWP (Clean = 41.5 gm^{-2}, Ship = 158.5 gm^{-2}) were observed, and the cloud albedo is estimated to have increased by 82 % (using Eq. (3.1); Table 3.3). For this optically thin cloud with an open cell structure and low background aerosol number concentration, the injection of ship exhaust produced a much brighter cloud than those neighboring owing to more numerous smaller droplets and higher

LWP. Also, numerous smaller droplets in ship tracks resulted in less efficient coalescence and a slightly lower cloud base precipitation rate, corroborating the argument in Albrecht et al. (1989). This response has been observed in previous field studies (e.g., Ferek et al., 1998; Lu et al., 2007). The open cell cloud thickened by 36%, with a considerably lower cloud base (~100 m) and a slightly lower cloud top.

During RF18, 19, and 24, an overcast sky existed with closed cell cloud structures (Fig. 3.3b). The clouds were non-drizzling in RF18, and lightly drizzling in RF19 and 24. A reduced cloud base rain rate was also evident in RF19 and RF24 ship-exhaust-perturbed conditions. Reduced sedimentation of cloud droplets near the cloud top entrainment zone tends to cause more efficient cloud top evaporation, enhancing turbulent kinetic energy and entrainment, and leading to smaller LWP and a thinner cloud (Bretherton et al., 2007). These phenomena (less precipitation, higher vertical velocity variance, lower LWP and thinner cloud) are evident in RF18 and 24 (Table 3.2 and 3.3).

Among the three closed cell cases, the perturbed cloud in RF19 had higher LWP, cloud thickness, and optical depth than the adjacent clean cloud, similar to that observed in the open cell cloud in RF20. However, the opposite response was observed in RF18 and 24, where decreases in LWP, cloud thickness, and optical depth in the ship track region were found. The difference in cloud macrophysical responses among these cases can be explained by the ambient thermodynamic conditions. The dewpoint depression (i.e., difference between temperature and dewpoint temperature, an estimate of moisture) above cloud top was much larger in RF18 and 24 as compared to RF19 and 20, indicating a drier free troposphere in these two cases (Table 3.3). The temperature and humidity variations near cloud top reflect the processes of cloud top entrainment warming and drying (positive $d\theta/dz$ and negative dq/dz near cloud top; not shown). As the boundary layer dried, the cloud base increased and cloud top height decreased, leading to a thinner cloud. Entrainment drying dominated the response of cloud water[31]. In RF18 and RF24, with drier air above the cloud deck and a relatively stable atmosphere in the closed cell cloud structure, not only did the LWP decrease, but the cloud optical depth also decreased by 20.7 % and 7.8 %, respectively.

The susceptibility of cloud albedo to increased N_d (i.e., dA/dN_d), was calculated for these four cases to evaluate the change between the unperturbed clouds and those perturbed by ship emission (Fig. 3.4). Comparing the cloud albedo susceptibility estimated from the analytical formulation based on the adiabatic assumption (Eq. 3) and derived using the droplet size spectrum (using Eq. 3.1 and $A = \tau/(\tau + 7.7)$; see also Table 3.3), the two derived albedo susceptibilities exhibit only small difference for non-precipitating and light drizzling clouds (RF18, 19, and 24, as shown in Fig. 3.4). However, for heavy drizzling clouds with open cell structure (RF20), the cloud albedo susceptibility derived using Eq. (3.1) is about twice as large as that from Eq. (3.3), indicating that the assumption of adiabatic conditions is not applicable for heavy drizzling clouds (see also Hayes et al., 2010). In RF18 and RF24, where negative albedo response (i.e., lower albedo with increased N_d) was observed, the sign of the cloud thickness effect is negative (Fig. 3.4), as stronger entrainment drying/warming led to a thinner cloud. The sign of the dispersion effect is also slightly negative in these two cases where non/light drizzle exists. The broadening of the spectrum is caused by the competition for water vapor in the relatively polluted, condensation-dominated regime, offsetting the cooling from the Twomey effect (Feingold and Seibert, 2009). This result is consistent with previous observational studies (e.g., Ackerman et al., 2000; Liu and Daum, 2002). In RF18 and RF24, though the sign of the Twomey effect is positive, it is offset by the negative cloud thickness effect, as the cloud optical depth is five times more sensitive to changes in cloud thickness (Eq. 3). Combined, these effects produced 11.8% and 2.2% (for RF18 and RF24, respectively) decreases in cloud albedo in the ship track region.

In RF20, with an open cell cloud structure and an optically thin cloud, the cloud susceptibility is the largest among the four cases. The Twomey effect, dispersion effect, and cloud thickness effect are all positive, with the largest contribution coming from the cloud thickness effect (Fig. 3.4). The positive dispersion effect (narrower droplet size spectrum under polluted condition) in this heavy drizzling case is in opposite trend to the cases with non/light drizzle (RF18, 19, 24). This result agrees with the large eddy simulation (LES) studies in Lu and Seinfeld (2006) and Chen et al. (2011), where a larger value of the dispersion effect occurs for clouds with stronger precipitation. With increased aerosol, smaller droplets suppress collision-coalescence, leading to less spectral broadening. Also, higher updraft velocity (due to stronger turbulence) leads to droplet condensational growth

and thus spectral narrowing (Lu and Seinfeld, 2006). In RF20, the dispersion effect acts to enhance the Twomey effect. Among these three major effects, the dispersion effect plays a minor role in the total albedo susceptibility. In RF19, with a closed cell cloud structure, cloud susceptibility is also positive. In these two cases (RF19 and RF20), the relatively moist overlying air led to less efficient entrainment drying, together with reduction in drizzle, resulting in higher LWP and albedo (cloud brightening).

3.4.2 Cloud Response in Ship Tracks: A-Train Observations

Based on 1-km MODIS imagery during the period June 2006–December 2009, 589 ship tracks were classified as closed cell, open cell, unclassifiable, or others by visually inspecting the cloud regions surrounding each ship track using MODIS images.

Among the 589 ship tracks identified, ship plumes enhanced the cloud albedo ~75 % of the time, while ~25 % of the time, a decrease in cloud albedo was observed. Ship tracks were separated into two categories: those with enhanced albedo (cloud brightening) and those with diminished albedo (cloud dimming) as compared to the surrounding clouds (Fig. 3.5). The average dewpoint depression (average moisture profile above the boundary layer from ECMWF-AUX reanalysis data, e.g., Partain, 2004; Benedetti, 2005) is higher in cloud dimming cases (24.0 K) than those in cloud brightening cases (18.0 K), consistent with the findings from the in-situ E-PEACE data. Also, the average cloud top height is higher in cases of reduced albedo, as a higher cloud top suggests a greater chance for the cloud layer to be decoupled from the surface moisture supply. Higher clouds, which are relatively decoupled and consequently not as susceptible to aerosol perturbations, were found to exhibit more frequent reduced cloud albedo than lower clouds. A dependence of albedo response on cloud top height was not observed during the E-PEACE in situ flights as the cloud top heights were all below 650 m. Based on the satellite data, the impacts of effective radius and optical depth on albedo response are less evident (Fig. 3.5). Generally, the average effective radius is slightly smaller, and the average optical depth is slightly higher in ship tracks for which a dimming response was observed than those with brightening response. Despite the higher cloud tops in the cloud dimming regime, smaller droplets in the ambient clouds were observed, suggesting that droplet growth was suppressed in an environment of drier air above cloud tops. In Christensen and Stephens

(2012), the optically thin clouds with larger droplets were the most susceptible to a cloud albedo increase. Based on satellite data, the effect of LTS (here defined as the difference in potential temperature at 700 mb and that at surface) on cloud albedo response is muted, as the average LTS is 22.2 (3.5) and 22.2 (3.3) K for the cloud brightening and dimming regimes, respectively (standard deviation in parenthesis; figure not shown).

The relative change of cloud thickness (or LWP) versus the Twomey effect determines, in short, the cloud albedo response. The dispersion effect is of secondary significance (Fig. 3.4; also in Chen et al., 2011). Based on Eq. (3.3), assuming the cloud thickness effect remains constant under quasi-instantaneous changes (i.e., the timescale over which the cloud microphysics adjusts to changes in aerosol concentration is rapid (order of minutes) compared to the macrophysical adjustment timescale, and thus in the quasi-instantaneous process clouds are macrophysically identical), the cloud susceptibility is simply the Twomey effect, and can be expressed as:

$$\frac{\Delta A}{A(1-A)} = \frac{1}{3}\Delta(\ln N_d) \qquad (3.4).$$

When the perturbed and unperturbed clouds are macrophysically similar (i.e., red dots in Fig. 3.6, defined by the absolute value of the fractional change in LWP and cloud top height less than 5%), the regime is defined as the Twomey regime (~30 % of ship tracks). As expected, at nearly constant LWP, cloud albedo is higher in the perturbed clouds compared to the surroundings, primarily resulting from increased N_d. When the macrophysical differences between perturbed and unperturbed clouds are larger (black dots in Fig. 6, in which clouds interact with the environment, leading to change in LWP), the differences in LWP govern the magnitude and sign of the cloud albedo response. With LWP increased in the ship track, the cloud albedo is influenced beyond that predicted by the Twomey effect and, in some ship tracks, the loss in LWP was so great that the cloud albedo enhancement was diminished to the point where complete cancellation occurred. The four in situ E-PEACE data points (Fig. 3.6) lie generally within the range of the satellite data distribution.

As the albedo response of the clouds is, to some extent, linked to the cloud top altitude and the dryness of the air above, the effects of the cloud top height and dew point

depression on the fractional change in cloud albedo, R_e, LWP, and H can be seen (see Fig. 3.7). The impact of the ship plumes on cloud droplet effective radius is relatively constant with cloud top height. On the other hand, fractional changes in LWP caused by the plume become increasingly negative as the cloud top height increases, in agreement with Christensen and Stephens (2012). Also, as the dew point depression above cloud top increases (drier air), the fractional change in LWP becomes increasingly negative. As the cloud albedo response follows closely the LWP response, the cloud brightening diminishes as the cloud top altitudes decrease and the free troposphere becomes drier. Cloud top height and dewpoint depression exert strong controls on the LWP response.

Clouds were classified as closed cell, open cell, unclassifiable, or others. In the closed cell regime, nearly 30% of ship tracks exhibit decreased cloud albedo. In the open cell and unclassifiable regimes, ~14% and 19% of the ship tracks, respectively, also exhibit decreased albedo.

3.5 Conclusions

The coupling among aerosol, cloud, precipitation, and meteorological conditions in the marine boundary layer is complex (Fig. 3.8). The so-called Twomey and Albrecht effects can lead to cloud brightening and thus cooling. On the other hand, in response to an aerosol perturbation, reduced in-cloud sedimentation leads to an increase of cloud water and evaporation in entrainment regions, resulting in stronger entrainment (Ackerman et al., 2004; Bretherton et al., 2007). Besides, less drizzle reduces below-cloud evaporative cooling and in-cloud latent heat release, resulting in higher turbulent kinetic energy and thus stronger entrainment (Wood, 2007). In this study, we evaluate, based on both in-situ and satellite data, the effect of environmental conditions, cloud cellular structures, and cloud properties (e.g., cloud top height, drizzling or not) on cloud albedo responses to ship emissions. Cloud brightening is evident in an open cellular cloud structure, and with relatively moist air above cloud tops. The opposite effect appears in the presence of a drier free troposphere and stable atmosphere in a closed cellular cloud structure. With sufficiently dry air above cloud tops, the enhanced entrainment drying/warming facilitated by smaller droplets in polluted clouds leads to lower LWP and thinner clouds. Also, increased stability led to less efficient boundary layer mixing and decreased moisture

supply from the ocean. When the negative cloud thickness effect outweighs the positive Twomey effect (Eq. 1), a lower cloud albedo results. Based on over 3 years of satellite data, both the dryness of the air above marine boundary layer and cloud top heights are seen to play significant roles in determining the albedo response. In the cases in which cloud albedo actually decreased, cloud top heights were deeper and capped by very dry overlying air. In classification of cloud cellular regimes, 30% of the closed cell ship tracks exhibited lower cloud albedo.

The satellite data show that, on average, 75% of the ship tracks are brighter than the surrounding clouds. When taken as a whole, the polluted clouds are about 2–3% more reflective than the surrounding clouds. The ship track radiative forcing at the local scale (averaged over numerous ship tracks) is on the order of ~ -10 to -20 W m^{-2} (e.g., Coakley et al., 1987; Christensen and Stephens, 2011). On the global scale, however, negligible radiative forcing from ship tracks has been observed (Schreier et al., 2007; Peters et al., 2011). In the current study, ~25% of the ship tracks produce a positive radiative forcing, the strength of which depends on the depth of the cloud (or decoupling) and the free-troposphere humidity. The current study employs ship track observations as means to assess the microphysics of aerosol-cloud relationships. Further studies are needed to quantify these effects on global scale.

While the present study has been motivated predominantly by gaining a more thorough understanding of the response of marine stratocumulus to perturbations in aerosol concentrations, it has obvious implications in terms of marine cloud brightening geo-engineering. There are some important differences, however; when the boundary layer is well mixed the buoyancy of ship exhaust may increase the amount of ship effluent entering the overlying clouds (Liu et al., 2000), whereas the surface generation of sea-salt particles, as demonstrated in the ship wake observations of Durkee et al. (2000), lead to a plume that is largely neutrally buoyant. The extent to which the added buoyancy from the plume aids in ship track formation is confounded by the observations from Hobbs et al. (2000) which demonstrate that the heat and moisture associated with ship exhaust dissipate rapidly into the boundary layer. Thus, the efficiency of vertical transport of a plume of sea salt aerosol, under a variety of conditions, needs to be considered in the design of a geo-engineering strategy.

Cloud macrophysical responses are crucial in determining both the strength and the sign of the cloud albedo response to aerosols intentionally injected into the marine boundary layer. These responses must be accounted for in global studies of the potential efficacy of sea spray geo-engineering as a means to counteract global warming.

3.6 Acknowledgements

This work was supported by Office of Naval Research grants N00014-10-1-0200 and N00014-04-1-0018, and National Science Foundation grant AGS-1008848. Y.-C. C. thanks D. Axisa, Z. Wang and H. Duong for help on aircraft data analysis.

3.7 Bibliography

Ackerman, A. S., Toon O. B., Taylor, J. P., Johnson, D. W., Hobbs, P. V., and Ferek, R. J.: Effects of aerosols on cloud albedo: Evaluation of Twomey's parameterization of the cloud susceptibility using measurement of ship tracks, J. Atmos. Sci., 57, 2684-2695, 2000.

Ackerman, A. S., Kirkpatrick, M. P., Stevens, D. E., and Toon, O. B.: The impact of humidity above stratiform clouds on indirect aerosol climate forcing, Nature, 432, 1014-1017, 2004.

Albrecht, B.: Aerosols, cloud microphysics, and fractional cloudiness, Science, 245, 1227-1230, 1989.

Bala, G., Caldeira, K., Nemani, R., Cao, L., Ban-Weiss, G., and Shin, H.-J.: Albedo enhancement of marine cloud to counteract global warming: impacts on the hydrological cycle, Clim. Dynam., 37, 915–931, doi:10.1007/s00382-010-0868-1, 2011.

Baumgardner, D., Jonsson, H., Dawson, W., O'Connor, D., and Newton, R.: The cloud, aerosol and precipitation spectrometer: a new instrument for cloud investigations, Atmos. Res., 59, 251–264, doi:10.1016/S0169-8095(01)00119-3, 2001.

Benedetti, A.: CloudSat AN–ECMWF ancillary data interface control document, Cooperative Institute for Research in the Atmosphere, Colorado State University, Fort Collins, CO 80523, 2005.

Bennartz, R.: Global assessment of marine boundary layer cloud droplet number concentration from satellite, J. Geophys. Res., 112, D02201, doi:10.1029/2006JD007547, 2007.

Bower, K., Choularton, T., Latham, J., Sahraei, J., and Salter, S.: Computational assessment of a proposed technique for global warming mitigation via albedo-enhancement of marine stratocumulus clouds, Atmos. Res., 82, 328–336, doi:10.1016/j.atmosres.2005.11.013, 2006.

Brenguier, J.-L., Pawloska, H., Sch¨uller, L., Preusker, R., and Fischer, J.: Radiative properties of boundary layer clouds: Droplet effective radius versus number concentration, J. Atmos. Sci., 57, 803–821, 2000.

Bretherton, C. S. and Wyant, M. C.: Moisture transport, lower-troposphere stability, and decoupling of cloud-topped boundary, J. Atmos. Sci., 54, 148-167, 1997.

Bretherton, C. S., Blossey, P. N., and Uchida, J.: Cloud droplet sedimentation, entrainment efficiency, and subtropical stratocumulus albedo. Geophys. Res. Lett., 34, L03813, doi:10.1029/2006GL027648, 2007.

Chen, Y.-C., Xue, L., Lebo, Z. J., Wang, H., Rasmussen, R. M., and Seinfeld, J. H.: A comprehensive numerical study of aerosol-cloud-precipitation interactions in marine stratocumulus, Atmos. Chem. Phys., 11, 9749–9769, doi:10.5194/acp-11-9749-2011, 2011.

Christensen, M. W. and Stephens, G. L.: Microphysical and macrophysical responses of marine stratocumulus polluted by underlying ships: Evidence of cloud deepening, J. Geophys. Res., 116, D03201, doi:10.1029/2010JD014638, 2011.

Christensen, M. W. and Stephens, G. L.: Microphysical and macrophysical responses of marine stratocumulus polluted by underlying ships. Part 2: Impacts of haze on precipitating clouds, J. Geophys. Res., 117, D11203, doi:10.1029/2011JD017125, 2012.

Coakley, J. A. and Walsh, C. D.: Limits to the aerosol indirect radiative effect derived from observations of ship tracks, J. Atmos. Sci., 59, 668–680, doi:10.1175/1520-0469(2002)059<0668:LTTAIR>2.0.CO;2, 2002.

Coakley, J. A., Bernstein, J. R., and Durkee, P. A.: Effect of ship track effluents on cloud reflectivity, Science, 237, 1020–1021, 1987.

Conant, W. C., VanReken, T. M., Rissman, T. A., Varutbangkul, V., Jonsson, H. H., Nenes, A., Jimenez, J. L., Delia, A. E., Bahreini, R., Roberts, G. C., Flagan, R. C., and Seinfeld, J. H.: Aerosol-cloud drop concentration closure in warm cumulus, J. Geophys. Res., 109, D13204, doi:10.1029/2003JD004324, 2004.

Durkee, P. A., Noone, K. J., and Bluth, R. T.: The Monterey area ship track experiment, J. Atmos. Sci., 57, 2523–2541, doi:10.1175/1520-0469(2000)057<2523:TMASTE>2.0.CO;2, 2000.

Feingold, G. and Seibert, H.: Cloud-Aerosol Interactions from the micro to cloud scale, in: Clouds in the perturbed climate system: their relationship to energy balance, atmospheric dynamics, and precipitation, edited by: Heintzenberg, J. and Charlson, R. J., 319–338, MIT Press, Cambridge, UK, 2009.

Ferek, R. J., Hegg, D. A., Hobbs, P. V., Durkee, P., and Nielsen, K.: Measurements of ship-induced cloud tracks off the Washington coast, J. Geophys. Res., 103, 23199-23206, doi:10.1029/98JD02121, 1998.

Hayes, C. R., Coakley, J. A., and Tahnk, W. R.: Relationships among properties of marine stratocumulus derived from collocated CALIPSO and MODIS observations, J. Geophys. Res., 115, D00H17, doi:10.1029/2009JD012046, 2010.

Hobbs, P. V., Garrett, T. J., Ferek, R. J., Strader, S. R., Hegg, D. A., Frick, G. M., Hoppel, W. A., Gasparovic, R. F., Russell, L. M., Johnson, D. W., O'Dowd, C., Durkee, P. A., Nielsen, K. E., and Innis, G.: Emissions from ships with respect to their effects on clouds, J. Atmos. Sci., 57, 2570–2590, doi:10.1175/1520-0469(2000)057<2570:EFSWRT>2.0.CO;2, 2000.

Hudson, J. G. and Yum, S. S.: Droplet spectral broadening in marine stratus, J. Atmos. Sci., 54, 2642–2654, doi:10.1175/1520- 0469(1997)054<2642:DSBIMS>2.0.CO;2, 1997.

IPCC: Summary for policymakers, in: Climate Change 2007: The Physical Science Basis, Contribution of Working Group I to the Fourth Assessment Report of the Intergovernmental Panel on Climate Change, edited by: Solomon, S., Qin, D., Manning,

M., Chen, Z., Marquis, M., Averyt, K. B., Tignor, M., and Miller, H. L., Cambridge University Press, 2007.

Jones, A., Haywood, J., and Boucher, O.: Climate impacts of geoengineering marine stratocumulus clouds, J. Geophys. Res., 114, D10106, doi:10.1029/2008JD011450, 2009.

King, M., Tsay, S.-C., Platnick, S., Wang, M., and Liou, K.-N.: Cloud retrieval algorithms for MODIS: Optical thickness, effective particle radius, and thermodynamic phase, Algorithm Theor. Basis Doc. ATBDMOD-05, NASA Goddard Space Flight Cent., 1998.

Korhonen, H., Carslaw, K. S., and Romakkaniemi, S.: Enhancement of marine cloud albedo via controlled sea spray injections: a global model study of the influence of emission rates, microphysics and transport, Atmos. Chem. Phys., 10, 4133–4143, doi:10.5194/acp-10-4133-2010, 2010.

Lacis, A. A. and Hansen, J. E.: A parameterization for the absorption of solar radiation in the Earth's atmosphere, J. Atmos. Sci., 31, 118–133, doi:10.1175/1520-0469(1974)031<0118:APFTAO>2.0.CO;2, 1974.

Lance, S., Brock, C. A., Rogers, D., and Gordon, J. A.: Water droplet calibration of the Cloud Droplet Probe (CDP) and inflight performance in liquid, ice and mixed-phase clouds during ARCPAC, Atmos. Meas. Tech., 3, 1683–1706, doi:10.5194/amt-3-1683-2010, 2010.

Latham, J., Rasch, P., Chen, C.-C., Kettles, L., Gadian, A., Gettelman, A., Morrison, H., Bower, K., and Choularton, T.: Global temperature stabilization via controlled albedo enhancement of low-level maritime clouds, Philos. Trans. Roy. Soc. London, 366, 3969-3987, doi:10.1098/rsta.2008.0137, 2008.

Lebsock, M. D., Stephens, G. L., and Kummerow, C.: Multisensor satellite observations of aerosol effects on warm clouds, J. Geophys. Res., 113, D15205, doi:10.1029/2008JD009876, 2008.

Lewellen, D. C. and Lewellen, W. S.: Entrainment and decoupling relations for cloudy boundary layers, J. Atmos. Sci., 59, 2966–2986, doi:10.1175/1520-0469(2002)059¡2966:EADRFC¿2.0.CO;2, 2002.

Liu, Q., Kogan, Y. L., Lilly, D. K., Johnson, D. W., Innis, G. E., Durkee, P. A., and Nielsen, K. E.: Modeling of ship effluent transport and its sensitivity to boundary layer structure, J. Atmos. Sci., 57, 2779–2791, doi:10.1175/1520-0469(2000)057<2779:MOSETA>2.0.CO;2, 2000.

Liu, Y. G., and Daum, P. H.: Anthropogenic aerosols: Indirect warming effect from dispersion forcing, Nature, 419, 580-581, 2002.

Lohmann, U. and Feichter, J.: Global indirect aerosol effects: a review, Atmos. Chem. Phys., 5, 715–737, doi:10.5194/acp-5-715- 2005, 2005.

Lu, M.-L. and Seinfeld, J. H.: Effect of aerosol number concentration on cloud droplet dispersion: a large-eddy simulation study and implications for aerosol indirect forcing, J. Geophys. Res., 111, D02207, doi:10.1029/2005JD006419, 2006.

Lu, M.-L., Conant, W. C., Jonsson, H. H., Varutbangkul, V., Flagan, R. C., and Seinfeld, J. H.: The Marine Stratus/Stratocumulus Experiment (MASE): Aerosol-cloud relationships in marine stratocumulus, J. Geophys. Res., 112, D10209, doi:10.1029/2006JD007985, 2007.

Lu, M.-L., Sorooshian, A., Jonsson, H. H., Feingold, G., Flagan, R. C., and Seinfeld, J. H.: Marine stratocumulus aerosol-cloud relationships in the MASE-II experiment: Precipitation susceptibility in eastern Pacific marine stratocumulus, J. Geophys. Res., 114, D24203, doi:10.1029/2009JD012774, 2009.

Partain, P.: CloudSat ECMWF-AUX auxiliary data process description and interface control document, Cooperative Institute for Research in the Atmosphere, Colorado State University, Fort Collins, CO 80523, 2004.

Partanen, A.-I., Kokkola, H., Romakkaniemi, S., Kerminen, V.-M., Lehtinen, K. E. J., Bergman, T., Arola, A., and Korhonen, H.: Direct and indirect effects of sea spray geoengineering and the role of injected particle size, J. Geophys. Res., 117, D02203, doi:10.1029/2011JD016428, 2012.

Peters, K., Quaas, J., and Grassl, H.: A search for large-scale effects of ship emissions on clouds and radiation in satellite data, J. Geophys. Res., 116, D24205, doi:10.1029/2011JD016531, 2011.

Pringle, K. J., Carslaw, K. S., Fan, T., Mann, G.W., Hill, A., Stier, P., Zhang, K., and Tost, H.: A multi-model assessment of the efficacy of sea spray geoengineering, Atmos. Chem. Phys. Discuss., 12, 7125–7166, doi:10.5194/acpd-12-7125-2012, 2012.

Radke, L. F., Coakley, J. A., and King, M. D.: Direct and remote sensing observations of the effects of ships on clouds, Science, 246, 1146–1149, doi:10.1126/science.246.4934.1146, 1989.

Rasch, P. J., Latham, J., and Chen, C.-C.: Geoengineering by cloud seeding: influence on sea ice and climate system, Environ. Res. Lett., 4, 1290–1301, doi:10.1088/1748-9326/4/4/045112, 2009.

Russell, L. M., Seinfeld, J. H., Flagan, R. C., Ferek, R. J., Hegg, D. A., Hobbs, P. V., Wobrock, W., Flossmann, A., O'Dowd, C. D., Nielsen, K. E., and Durkee, P. A.: Aerosol dynamics in ship tracks, J. Geophys. Res., 104, 31077–31095, 1999.

Russell, L. M., Sorooshian, A., Seinfeld, J. H., Albrecht, B. A., Nenes, A., Ahlm, L., Chen, Y.-C., Coggon, M., Craven, J. S., Flagan, R. C., Frossard, A. A., Jonsson, H., Jung, E., Lin, J. J., Metcalf, A. R., Modini, R., Muelmenstaedt, J., Roberts, G. C., Shingler, T., Song, S., Wang, Z., and Wonaschuetz, A.: Eastern Pacific Emitted Aerosol Cloud Experiment (E-PEACE), B. Am. Meteorol. Soc., submitted, 2012.

Salter, S., Sortino, G., and Latham, J.: Sea-going hardware for the cloud albedo method of reversing global warming, Philos. Trans. Roy. Soc. London, 366, 3989–4006, doi:10.1098/rsta.2008.0136, 2008.

Savic-Jovcic, V. and Stevens, B.: The structure and mesoscale organization of precipitating stratocumulus, J. Atmos. Sci., 65, 1587-1605, 2008.

Schreier, M., Mannstein, H., Eyring, V., and Bovensmann, H.: Global ship track distribution and radiative forcing from 1 year of AATSR data, Geophys. Res. Lett., 34, L17814, doi:10.1029/2007GL030664, 2007.

Segrin, M. S., Coakley, J. J. A., and Tahnk, W. R.: MODIS observations of ship tracks in summertime stratus off the west coast of the United States, J. Atmos. Sci., 64, 4330–4345, doi:10.1175/2007JAS2308.1, 2007.

Seinfeld, J. H. and Pandis, S. N.: Atmospheric Chemistry and Physics, John Wiley and Sons, Inc., Hoboken, NJ, 2nd edn., 2006.

Stephens, G. L.: Radiation profiles in extended water clouds. Part II: Parameterization schemes, J. Atmos. Sci., 35, 2123–2132, doi:10.1175/1520-0469(1978)035<2123:RPIEWC>2.0.CO;2, 1978.

Stephens, G. L., Gabriel, P. M., and Partain, P. T.: Parameterization of atmospheric radiative transfer. Part I: Validity of simple models, J. Atmos. Sci., 58, 3391–3409, 2001.

Stevens, B. and Brenguier, J.-L.: Cloud controlling factors: low clouds. Clouds in the perturbed climate system, Heintzenberg, J. and Charlson, R. J., The MIT Press, Cambridge, Massachusetts, 173-196, 2009.

Stevens, B. and Feingold, G.: Untangling aerosol effects on clouds and precipitation in a buffered system, Nature, 461, 607-613, 2009.

Stevens, B., Cotton, W. R., Feingold, G., and Moeng, C.-H.: Large-eddy simulations of strongly precipitating, shallow, stratocumulus-toped boundary layers, J. Atmos. Sci., 55, 3616-3638, 1998.

Stevens, B., Vali, G., Comstock, K., vanZanten, M. C., Austin, P. H., Bretherton, C. S., and Lenschow, D. H.: Pockets of open cells and drizzle in marine stratocumulus, B. Am. Meteorol. Soc., 86, 51–57, 2005.

Twohy, C. H., Petters, M. D., Snider, J. R., Stevens, B., Tahnk, W., Wetzel, M., Russell, L., and Burnet, F.: Evaluation of the aerosol indirect effect in marine stratocumulus clouds: Droplet number, size, liquid water path, and radiative impact, J. Geophys. Res., 110, D08203, doi:10.1029/2004JD005116, 2005.

Twomey, S.: Aerosols, clouds, and radiation, Atmos. Environ., 25, 2435–2442, 1991.
vanZanten, M. C., Stevens, B., Vali, G., and Lenschow, D. H.: Observations of drizzle in nocturnal marine stratocumulus, J. Atmos. Sci., 62, 88-106, 2005.

Wang, H. and Feingold, G.: Modeling mesoscale cellular structures and drizzle in marine stratocumulus. Part I: Impact of drizzle on the formation and evolution of open cells, J. Atmos. Sci., 66, 3237-3256, 2009a.

Wang, H., Rasch, P. J., and Feingold, G.: Manipulating marine stratocumulus cloud amount and albedo: a process-modelling study of aerosol-cloud-precipitation interactions in response to injection of cloud condensation nuclei, Atmos. Chem. Phys., 11, 4237–4249, doi:10.5194/acp-11-4237-2011, 2011.

Warren, S. G., Hahn, C. J., London, J., Chervin, R. M., and Jenne, R. L.: Global distribution of total cloud cover and cloud type amounts over the ocean. NCAR Tech. Note NCAR/TN-317+STR, 42 pp., 1988.

Wood, R.: Cancellation of aerosol indirect effects in marine stratocumulus through cloud thinning, J. Atmos. Sci., 64, 2657-2669, 2007.

Zhang, G., Vivekanandan, J., and Brandes, E.: A method for estimating rain rate and drop size distribution from polarimetric radar measurements, IEEE T. Geosci. Remote, 39, 830–841, 2001.

Zhao, G., Chu, R., Zhang, T., Li, J., Shen, J., and Wu, Z.: Improving the rainfall rate estimation in the midstream of the Heihe River Basin using raindrop size distribution, Hydrol. Earth Syst. Sci., 15, 943–951, doi:10.5194/hess-15-943-2011, 2011.

Table 3.1 Instrumentation Payload on CIRPAS Twin Otter.

Parameter	Instrument	Detected Size
Particle Number Concentration	Condensation Particle Counter: CPC3010 CPC3025	D_p[a] > 10 nm D_p > 3 nm
Aerosol Size Distribution	Passive Cavity Aerosol Spectrometer Probe (PCASP) Scanning Differential Mobility Analyzer (DMA)	0.1–2.6 μm 15 nm–1 μm
Cloud and Drizzle Drop Size Distribution	Cloud, Aerosol, and Precipitation Spectrometer[b] (CAPS) Phase Doppler Interferometer (PDI) Forward Scattering Spectrometer Probe (FSSP) Gerber Light Diffraction (PVM-100 probe)	0.4 μm–1.6 mm 4–200 μm 1–46 μm ~ 5–50 μm
Aerosol Bulk Composition	Aerodyne Time-of-Flight Aerosol Mass Spectrometer (AMS) Single-Particle Soot Photometer (SP2)	D_{va}[c] ~ 40 nm–1 mm
Particle Properties	Cloud Condensation Nuclei Counter (CCN Spectrometer) Particle Soot Absorption Photometer (PSAP) Photoacoustic Soot Spectrometer (PASS-3)	
Cloud Structures	Frequency-Modulated Continuous-Wave 94 GHz Doppler Cloud Radar (upward-facing)	
Particle and Droplet Inlets	Counterflow Virtual Impactor (CVI)	
Meteorological variables (Temperature, relative humidity, wind properties, etc.)	Meteorology probes	

[a] Particle diameter.
[b] Drizzle drop size distribution is measured by the Cloud Imaging Spectrometer (CIP-2D), included in the CAPS package.
[c] Vacuum aerodynamic diameter.

Table 3.2 Aerosol/cloud properties measured during E-PEACE Research Flights 18, 19, 20, and 24. For the cloud structure, closed/open means closed or open cloud cellular structure. Cloud layer is defined with cloud droplet number concentration > 10 cm^{-3} and liquid water content > 0.01 gm^{-3}. Mean N_a, N_d, r_e (cloud drop effective radius), and k (droplet spectral shape parameter) are geometric mean values. BL average w'w' is the mean vertical velocity variance in the boundary layer. Standard deviation is in parenthesis.

Research Flight (2011)		Cloud Structure	Cloud top (m)	Cloud base (m)	Cloud thickness (m)	Mean N_a (> 120 nm)	Mean N_d (cm^{-3})	Mean r_e (μm)	Cloud base rain rate ($mm\ d^{-1}$)	BL mean $w'w'$ ($m^2\ s^{-2}$)	k
RF18	Clean	Closed	609.5	460.0	149.5	153.9 (96.3)	216.1 (44.1)	6.15 (0.97)	n/a	0.214	0.81
(2 Aug)	Ship		598.8	475.3	123.5	379.5 (137.7)	316.8 (117.4)	5.45 (0.84)	n/a	0.216	0.71
RF19	Clean	Closed	630.7	329.1	301.6	126.2 (82.4)	161.4 (33.6)	8.80 (1.04)	0.63 (0.28)	0.239	0.74
(3 Aug)	Ship		648.2	266.2	382.0	217.6 (111.3)	341.7 (127.7)	7.32 (1.18)	0.60 (0.32)	0.311	0.73
RF20	Clean	Open	616.3	363.9	252.4	24.3 (13.8)	14.0 (6.4)	16.94 (2.63)	12.53 (4.03)	0.103	0.39
(4 Aug)	Ship		608.6	264.8	343.8	73.4 (43.1)	39.0 (9.3)	16.01 (2.73)	11.40 (3.60)	0.113	0.57
RF24	Clean	Closed	607.7	238.6	369.1	115.2 (78.2)	153.5 (38.7)	9.27 (1.57)	1.58 (0.54)	0.135	0.65
(10 Aug)	Ship		591.5	254.4	337.1	197.2 (96.0)	193.5 (80.5)	8.76 (1.36)	1.07 (0.59)	0.200	0.63

Table 3.3 Cloud LWP, optical properties, and environmental conditions measured during E-PEACE Research Flights 18, 19, 20, and 24. Standard deviation is in parenthesis.

Research Flight		LWP ($g m^{-2}$)	Optical depth τ[a]	Cloud albedo A	$\Delta LWP/LWP$[b]	$\Delta A/A$	Dewpoint depression[c] (K)
RF18	Clean	31.0	7.3	0.49	−0.33	−0.12	40.0 (1.4)
(2 Aug)	Ship	21.1	5.8	0.43			
RF19	Clean	104.0	18.4	0.70	0.62	0.16	14.3 (1.4)
(3 Aug)	Ship	168.2	35.4	0.82			
RF20	Clean	41.5	4.6	0.37	2.82	0.82	2.8 (0.5)
(4 Aug)	Ship	158.5	16.4	0.68			
RF24	Clean	128.6	21.8	0.74	−0.17	−0.02	16.9 (1.8)
(10 Aug)	Ship	107.2	20.1	0.72			

[a] Calculated using Eq. (1).
[b] Relative LWP difference between exhaust-perturbed and unperturbed clouds.
[c] The free tropospheric dewpoint depression ($T - T_d$) is averaged over the region from 100 m above the cloud top to the highest point reached in the flight (on average 100 to ~ 140 m above cloud top).

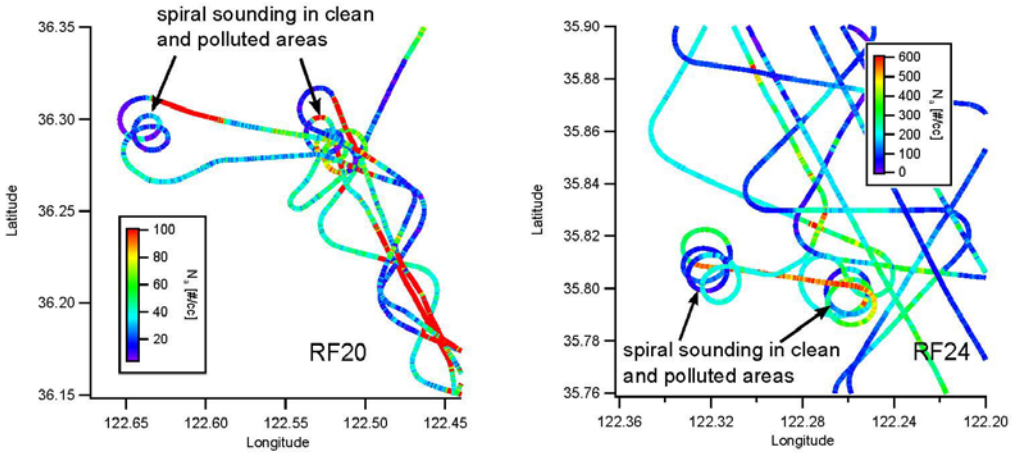

Figure 3.1 Spiral soundings of clean and ship exhaust perturbed areas in E-PEACE research flight 20 and 24 (4 and 10 August 2011, respectively). Flight path is colored according to aerosol number concentration (particle diameter >120 nm).

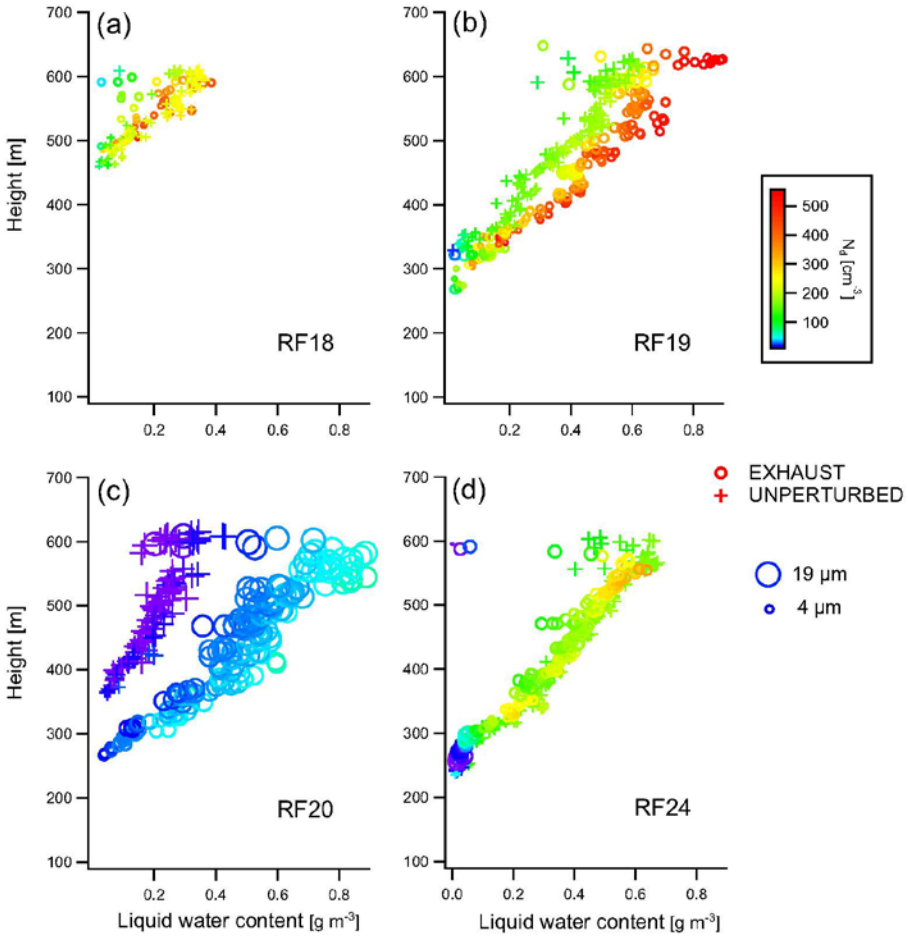

Figure 3.2 Cloud microphysical parameters measured along the flight tracks. Each symbol represents data over a 1 s increment. Cloud droplet number concentration [cm^{-3}] is colored on a logarithmic scale; droplet effective radius (r_e) is given by the size of symbols varying between ~4 and 19 µm. Clean and perturbed cloud data are presented by crosses and open circles, respectively.

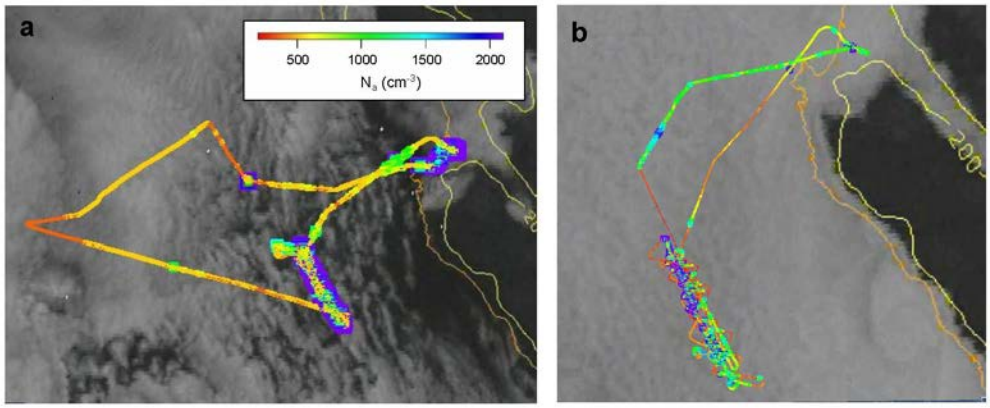

Figure 3.3 GOES satellite images. Satellite images during **(a)** RF20 (4 August 2011) and **(b)** RF24 (10 August 2011) off coast of Monterey, CA, exemplifying open and closed cell cloud structures, respectively. Flight path is colored according to aerosol number concentration (particle diameter > 10 nm).

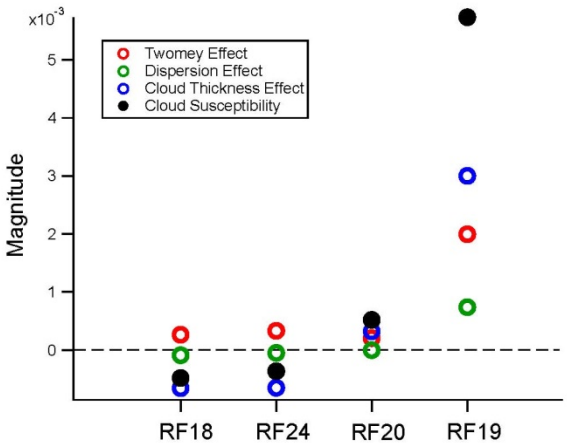

Figure 3.4 Magnitude of cloud susceptibility in four E-PEACE cases. Twomey effect (red circle), dispersion effect (green circle), cloud thickness effect (blue circle), and total cloud albedo susceptibility based on Eq. (3.3) (black circle) and Eq. (3.1) (black cross) for RF18, RF24, RF19, and RF20 (order from low to high cloud albedo susceptibility).

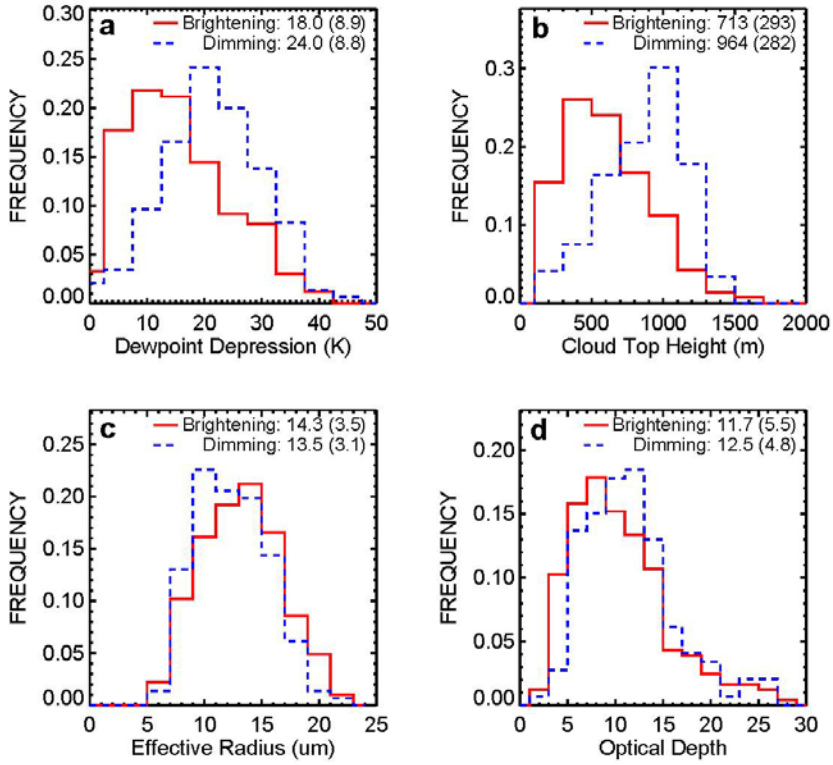

Figure 3.5 Frequency distribution of different parameters for 589 individual ship tracks from June 2006–December 2009 A-Train observations. The parameters include: **(a)** dew point depression, **(b)** cloud top height, **(c)** effective radius, and **(d)** optical depth. Albedo enhancement (brightening) and decrease (dimming) cases are shown by red and blue lines, respectively. Means and (standard deviations) are given at the top of each panel. The cloud top height, effective radius, and optical depth are averaged over the unpolluted cloudy sections of each ship track.

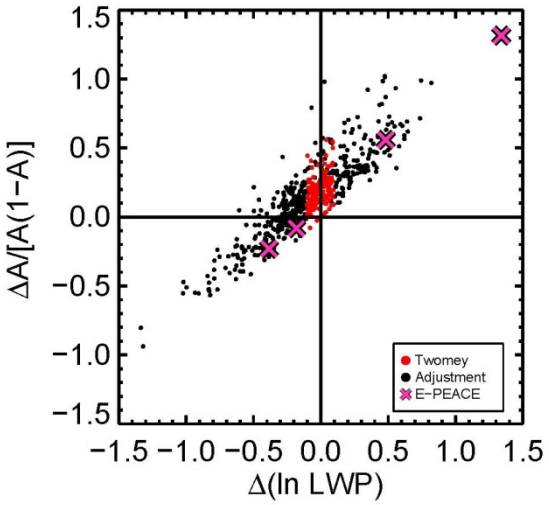

Figure 3.6 Fractional change in cloud albedo (Eq. 3.4) versus the fractional change in logarithm LWP. Indicated are the regime of the Twomey effect (red dots, defined by the absolute value of the fractional change in LWP less than 5 %) and of LWP feedback adjustment (black dots, in which clouds interacted with the environment, resulting in change in LWP). The four E-PEACE data points (pink) are shown.

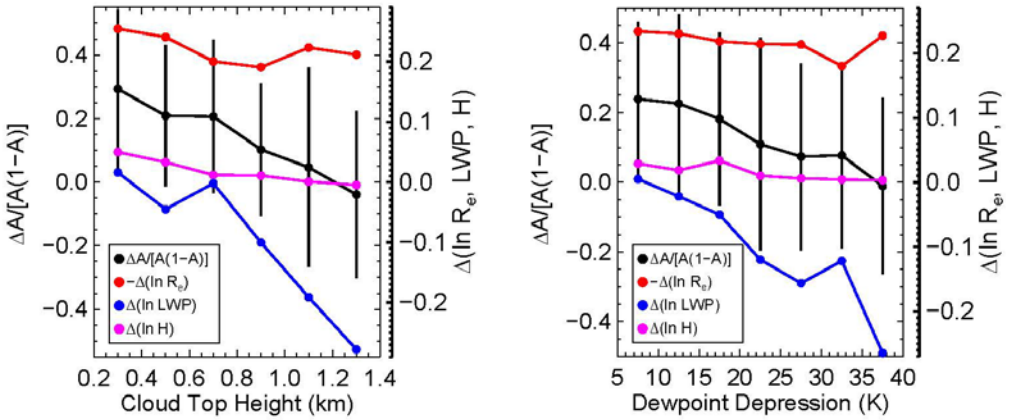

Figure 3.7 Binned change in albedo, effective radius (r_e), LWP, and cloud thickness (H) as a function of cloud top height (left panel), and dew point depression (right panel) based on 589 ship tracks observed over June 2006–December 2009. Cases were binned by 200 m wide bins in cloud top height and 5 K wide bins in dewpoint depression. A minimum of 20 ship tracks was required for each bin. Error bars were determined from the standard deviation of average cloud albedos taken from the population of ship tracks in each bin. The length of the error bars extends over two standard deviations; i.e., the bar extends one standard deviation below and one above the mean for each bin.

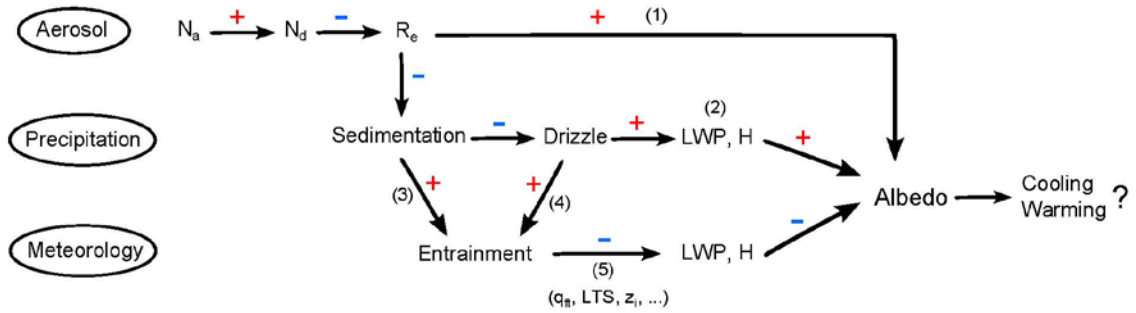

Figure 3.8 Conceptual diagram displaying the interactions among aerosol, cloud, precipitation, and meteorology. The response of each property/phenomenon to increased aerosol (N_a) is shown as a red plus (signifying positive response), and a blue minus (negative response) sign.
Footnotes to figure: (1) Twomey effect (Twomey, 1991). (2) Albrecht effect (Albrecht, 1989). (3) Sedimentation-entrainment effect (Bretherton et al., 2007). (4) Drizzle-entrainment effect (Wood, 2007). (5) Significant meteorological conditions, such as free tropospheric humidity (q_{ft}), large scale divergence rate, as well as cloud top height (z_i), can control the MSc structure (Wood, 2007; Chen et al., 2011).

Chapter 4

Satellite Estimate of Global Aerosol Indirect Forcing by Marine Warm Clouds

4.1 Abstract

The effect of anthropogenic atmospheric aerosols on global cloud radiative forcing is termed the aerosol indirect effect (AIE). Intergovernmental Panel on Climate Change (IPCC) estimates the AIE to be the single largest uncertainty in global radiative forcing. The AIE is divided into two components: the *intrinsic* effect of aerosol variations on cloud albedo and the *extrinsic* effect of aerosol variations on fractional cloud cover. Of the world's clouds, low-level marine clouds exert the largest impact on the planet's albedo. Here we perform a comprehensive analysis of multiple A-Train satellite measurements of co-located aerosols and clouds over the world's oceans for the period August 2006 to December 2009, comprising over 130 million pixels, of which ~ 3.7 million pixels pass screening for single-layer marine warm clouds. Using the local anthropogenic aerosol fraction estimated from GEMS (Global and regional Earth-system Monitoring using Satellite and in-situ data), we estimate the intrinsic component of global oceanic warm cloud AIE as -0.49 W m^{-2} . The corresponding estimate for the extrinsic AIE is -1.53 W m^{-2}. These results suggest that present-day aerosol indirect forcing is substantial, implying that, with aerosol levels expected to remain roughly at present levels, future warming will accelerate as greenhouse gas levels continue to rise.

4.2 Introduction

Since the preindustrial era, anthropogenic aerosols have increased and are known to alter the cloud microphysics (e.g., droplet size), cloud macrophysics (e.g., liquid water path (LWP), cloud thickness), cloud lifetime, etc., and thus affect the cloud albedo and Earth's climate. These effects, termed as aerosol indirect effects (AIE), remain one of the largest uncertainties in the quantification of anthropogenic radiative forcing of climate (IPCC, 2007). IPCC (2007) estimated the aerosol indirect radiative forcing to be -0.7 Wm^{-2}, with an uncertainty range between -1.8 and -0.3 Wm^{-2}. From previous modeling and/or satellite studies, the AIE evaluation is highly inconsistent as pointed out in Penner et al. (2011), limiting our ability to accurately predict climate response.

Marine warm clouds, generally abundant and optically thick, have an annual and global averaged net cooling effect of -15 W m^{-2} (Hartmann et al., 1992). It has been estimated that a 6% increase of the albedo of global marine stratocumulus (MSc) would offset the warming by atmospheric CO_2 doubling (Latham et al., 2008). As both aerosol levels and meteorology control cloud properties (Stevens and Brenguier, 2009), it is essential to understand globally how the clouds respond to

changes in the environmental conditions, including large-scale subsidence, free tropospheric humidity, sea surface temperature, etc. (e.g., Wood 2007; Chen et al., 2011). Some previous satellite studies (e.g., Matsui et al., 2006; Lebsock et al., 2008) have examined the dependence of marine low cloud responses on lower tropospheric stability (LTS) and aerosols. Yet, there is no systematic, global observation-based analysis on the aerosol-cloud interactions under various environmental conditions and raining/non-raining conditions.

In order to use satellite observations to calculate the aerosol indirect radiative forcing caused by anthropogenic activities, it is essential to estimate the anthropogenic fraction since the natural aerosols and anthropogenic aerosols cannot be directly distinguished by satellite measurements. In addition, anthropogenic aerosol can vary widely over spatial and temporal scales, therefore it is imperative to capture this variability when assessing the indirect forcing. Some assumed a globally averaged increase of 30% in aerosol number concentration since preindustrial era (Sekiguchi et al., 2003; Lebsock et al., 2008). As aerosols from urban/industrial pollution and smoke are dominated by fine aerosols, Kaufman et al. (2005) used fine aerosol fraction retrieved from Moderate Resolution Imaging Spectroradiometer (MODIS) to estimate anthropogenic composition, and it is estimated that 21 ± 7% of the aerosol optical depth (AOD) over the oceans has an anthropogenic origin. Bellouin et al. (2005) also determined the anthropogenic aerosol using accumulation-mode fraction from MODIS. Other than applying MODIS to compute anthropogenic aerosol, aerosol product from GEMS (Global and regional Earth-system Monitoring using Satellite and in-situ data; online information at http://gems.ecmwf.int/) aerosol modeling system can also be used, which is a near real-time system for assimilation and forecast of aerosols, greenhouse gases, and reactive gases. Aerosol species, including sea salt, dust, organic matter, black carbon, and sulfate aerosols, are accounted for in GEMS (Hollingsworth et al., 2008). These classified aerosol datasets can help identify the anthropogenic aerosol fraction and be utilized to estimate the aerosol indirect radiative forcing.

Despite decades of research, no consensus has made on establishing climatically meaningful interactions among aerosol, cloud, and precipitation (Stevens and Feingold, 2009). To untangle the interwoven effects of weather condition, raining/non-raining status, and aerosols on clouds, we perform a comprehensive investigation of the interplay between marine warm cloud microphysical/macrophysical properties, aerosol levels, and large scale dynamic/thermodynamic states using A-Train satellite observations. To improve our assessment, the anthropogenic aerosol

fraction is estimated using both the GEMS and MODIS. We further obtain a new estimate of aerosol indirect radiative forcing for marine warm clouds based on the anthropogenic aerosol fraction, with both shortwave and longwave components.

4.3 Data description

More than 40 months of observations from August, 2006 to December, 2009 from multiple sensors in A-Train satellite constellation are analyzed in this study. The dataset include CloudSat radar observations collocated with aerosol and cloud properties from Moderate Resolution Imaging Spectroradiometer (MODIS), Cloud-Aerosol Lidar and Infrared Pathfinder Satellite Observations (CALIPSO), the Advanced Microwave Scanning Radiometer (AMSR-E), and cloud albedo from the Clouds and Earth's Radiant Energy System (CERES). The European Center for Medium range Weather Forecast-AUXiliary analysis (ECMWF-AUX) products, interpolated in space and time to the CloudSat data, are available from the CloudSat data processing center and are included in the analysis to account for the environmental conditions. The National Centers for Environmental Prediction (NCEP) dataset are also added for the environmental variables not included in the ECMWF-AUX product.

Table 4.1 lists the sensors and derived parameters applied in this study. It is worth mentioning that the differences in spatial resolution between sensors are not considered in the analysis. The aerosol index (AI = aerosol optical depth (AOD) × Ångström exponent) derived from MODIS (Remer et al., 2005) is used as a proxy for column cloud condensation nuclei (CCN). The Ångström exponent is calculated based upon 0.55 μm and 0.867 μm AOD, providing information on the particle size; the larger the exponent, the smaller the particle. Cloud optical properties are obtained from the MODIS cloud product on the Aqua satellite (MYD06), including 3.7 μm cloud effective radius (R_e), cloud optical depth (τ), and the derived LWP ($LWP = \frac{2}{3} R_e \rho_l \tau$, where ρ_l is liquid water density). The AMSR-E also provides an independent estimate of LWP and the column water vapor (Wentz and Spencer, 1998). Cloud top height, number of cloud layers, and aerosol top/base heights are obtained from CALIPSO (5 km horizontal resolution level 2 product; version 3.01).

To remove ice and mixed phase clouds from the analysis, the cloud top pressure and temperature from the MYD06 product are used to identify warm liquid clouds as those with cloud top pressures greater than 500 hPa and cloud top temperatures greater than 270 K. In addition, cloud phase

retrieved by MODIS within the CERES footprint is applied to screen out pixels with occurrence of ice cloud. The single-layered cloud criterion from CALIPSO is also applied to minimize the uncertainty in the retrieved cloud optical properties from MODIS. AOD over cloud is required to be less than 0.1 using CALIPSO. This is the first observational study to use multiple active and passive satellite sensors to screen out overlying layers of cloud and aerosol, which have traditionally been an obstacle to isolating cloud responses to changing environmental conditions or aerosol concentrations (Wilcox et al., 2010; Christensen et al., 2013).

To distinguish between precipitating and non-precipitating clouds, the precipitation flag from CloudSat 2C-PRECIP-COLUMN product (Haynes et al. 2009) is applied to separate non-precipitating, drizzling (defined as possible or probable precipitation being detected), and precipitating clouds (with surface precipitation). Based on the warm oceanic cloud dataset, 83.5% of warm clouds are non-precipitating, 11.0% are defined as drizzling, and 5.5% are precipitating.

The LTS is derived based on the potential temperature difference between 700 hPa and the surface (LTS = $\theta_{700\text{hPa}} - \theta_{\text{surface}}$) using the ECMWF-AUX data from the CloudSat data processing center. The free tropospheric relative humidity (RH_{ft}) is averaged over the levels above the inversion layer. If there is no temperature inversion layer, it is assumed that the top of boundary layer is at 850 hPa. The wind speed and sea surface temperature are also obtained from ECMWF-AUX.

The cloud albedo is derived based on CERES TOA shortwave radiative flux acquired from the CALIPSO-CloudSat-CERES-MODIS (CCCM) product (Kato et al. 2010). First, the CERES clear sky albedo (the ratio of TOA upwelling flux to downwelling flux under cloud-free conditions) is calculated for its seasonal climatology following a methodology similar to that of Coakley et al. (2005). The albedo of the ocean is assumed to be constant over a seasonal cycle. The wind stress over the surface can cause roughening/brightening and contribute to a larger uncertainty in albedo. The cloudy sky albedo (A_{cld}) is derived using: $A_{cld} = [A_{all} - (1 - c_f)A_{clr}]/c_f$, where A_{all} is CERES all sky albedo, and c_f is the MODIS cloud fraction reported over the CERES footprint. To avoid the overestimation of MODIS retrieved cloud optical depth and cloudy sky albedo derived from CERES when the sun is near the horizon (due to scattering of solar radiation), data for which the solar zenith angle exceeds 60° are screened out.

GEMS is a framework developed by ECMWF Integrated Forecast System (IFS), and is the first aerosol model fully coupled to a numerical weather prediction model with data assimilation of satellite aerosol optical depth (Mangold et al., 2011). Different aerosol species (sea salt, dust, organic matter, black carbon, and sulfate) are included in GEMS, and is applied to calculate the anthropogenic aerosol fraction.

After screening by the previously mentioned strict criteria on marine warm clouds, ~3.7 million cloudy pixels are remained for analysis. Table 4.2 lists the screening methods and the percentage of data remaining after applying each criterion, providing some insight for data selection.

4.4 Results

4.4.1 Globally averaged aerosol-cloud responses

As aerosol index represents the CCN concentration, it is shown that AI well correlates with GEMS sulfate and black carbon AOD (Fig. 4.1A, 4.1B), demonstrating that AI is a good indicator of the anthropogenic activities. The global relationships between cloud properties and aerosol index are shown in Fig. 4.1C-H for precipitating, drizzling, and non-precipitating clouds. There are 98.2% of data lie within AI 0.01–1, and 60% of data has AI less than 0.1, sorted as the clean regime. Globally, the effective radius decreases with AI for all three cloud types (Fig. 4.1C), consistent with Lebsock et al. (2008). Based on the nonlinear relationship between R_e and AI, the larger change in R_e occurs between AI 0.1 and 0.2, where the magnitude of R_e-AI slope decreases the most. This shows that the sensitivity of R_e to AI is higher during the transition from clean to polluted condition. The decrease in R_e with AI is evident for non-precipitating clouds (Table 4.3). However, the R_e -AI relationships for drizzling/precipitating clouds are harder to translate directly as these clouds containing more larger droplets have bimodal droplet size distribution, also been discussed in Lebsock et al. (2008).

Using the LWP retrieved from AMSR-E, LWP-AI relationship is negative for non-precipitating clouds (Table 4.3), indicating the enhanced turbulence and entrainment drying caused by smaller and numerous cloud drops leads to lower LWP, as also shown in previous studies (e.g., Ackerman et al., 2004; Wood et al., 2007). For drizzling/ precipitating clouds, the inhibited collision-coalescence process and precipitation suppression from enhanced aerosol results in positive LWP response, as suggested by Albrecht (1989). As noted in Lebsock et al. (2008), the uncertainty from

algorithm assumptions affects the AMSR-E LWP retrieval for precipitating clouds, and thus needs to be considered with caution. Nevertheless, similar LWP-AI response is shown using MODIS derived LWP (Fig. 4.1E), both showing that the LWP enhances more for drizzling/precipitating clouds. The difference in these two derived LWP-AI relationships lies in the different sign of the linear slope for non-precipitating clouds (Table 4.3).

For the cloud top height (H) response, the mean cloud top becomes lower with increased AI for non-precipitating and drizzling clouds, whereas mean H gets higher with AI for precipitating clouds except under very polluted conditions (Fig. 4.1F; Table 4.3). This response is associated with the large scale dynamic state and thermodynamic condition, and will be discussed in detail in Section 4.4.2.

The cloud optical depth increases with AI for all cloud types, with larger slope for drizzling and precipitating clouds (Table 4.3). This shows that combining the effects from R_e and LWP responses (τ can be viewed as a function of R_e and LWP), the τ-AI relationship is stronger under raining condition, consistent with the trend in LWP-AI response. Also, the same tendency occurred for the slope between cloudy sky albedo and AI (Table 4.3), demonstrating the cloud albedo susceptibility is larger for drizzling/precipitating clouds. This shows that with precipitation suppression from increased aerosol, the enhanced LWP contributes significantly to the cloud albedo response.

4.4.2 Global map of aerosol-cloud interactions

The global maps of linear fitting slope between cloud properties and AI for warm clouds are shown in Fig. 4.2 (including non-precipitating, drizzling, and precipitating clouds), where the slopes are calculated over a 4°×4° segmented area, and grids with less than 300 contributing data points are excluded. Each grid is statistically significant at the 95% of confidence level. Figure 4.2A shows the slope of linear fit between R_e and $\log_{10}$(AI). In most oceanic regions, R_e decreases with increased AI, as suggested by Twomey (1974) and also shown in previous studies (e.g., Sekiguchi et al., 2003). However, in the remote ocean in South Pacific Ocean and certain regions in South Indian Ocean, R_e increases with AI, a feature opposite to the Twomey effect. The positive relationship between R_e and aerosol has also been observed in some previous studies (Sekiguchi et al., 2003; Storelvmo et al., 2006; Yuan et al., 2008). Yuan et al. (2008) attributed the response to environmental conditions, and indicated the slope is mainly driven by water vapor amount (as Twomey effect is established on the competition of available water). Based on the global map of

column water vapor from AMSR-E (Figure 4.3A), it is shown that the water vapor amount is higher in the regions north of the equator, as well as in the southern Pacific Ocean and Indian Ocean near equator. To certain extent, the regions with high water vapor correspond to regions with positive Re-AI slope, but not perfectly. It is noticed that the regions with positive R_e response are relatively clean. Based on the anthropogenic aerosol fraction (A_{frc}) estimated from GEMS (defined as the mass fraction of sulfate and black carbon), southern Pacific Ocean and Indian Ocean have low anthropogenic aerosol fraction (Fig. 4.3B), and the main composition is marine sea salt (not shown). Under the pristine background aerosol in remote oceans, an increase in aerosol under moist environment may not limit the droplet growth. However, it is found difficult to explain such positive correlation with further evidence. Further investigations are needed to clarify the observed phenomenon.

The global map of linear fitting between AMSR-E LWP and $\log_{10}$(AI) is illustrated in Fig. 4.2B (note that the LWP-AI response using AMSR-E LWP and MODIS derived LWP shows similar pattern). Globally, the sign of slope (positive or negative) is somewhat noisy, but overall the LWP increases with AI in most regions. Near the equator where the clouds have higher probability of precipitation (Figure 4.3C), the LWP enhanced more with aerosol, a result of precipitation suppression (as discussed in section 4.4.1). Also, the atmosphere is more unstable and moist in the tropics, under which the LWP tends to enhance with increased AI. However, in the regions of persistent MSc (South Atlantic Ocean, areas off the west coast of South/North America), LWP generally does not increase with increasing aerosol, and even decreases in certain cases. These MSc-dominant regions are characterized by low free tropospheric relative humidity (RH_{ft}) and enhanced lower tropospheric stability (LTS) (Fig. 4.3D, 4.3E) resulting from large scale subsidence. Cloud top entrainment facilitated by smaller and more numerous cloud drops brings the overlying dry air into the boundary layer, resulting in lower LWP in certain regions.

A similar global pattern as that for LWP occurs for the cloud top height (H) response to changes in AI (Fig. 4.2C). Under moist free troposphere and unstable environments, the boundary layer deepens with higher LWP in response to enhanced aerosol; this cloud deepening has also been observed in ship tracks in a relatively moist and unstable environment (Christensen and Stephens, 2011, 2012). On the contrary, under dry and stable conditions (where MSc are prevalent), the strong subsidence (Fig. 4.1F) prevents the cloud from deepening, even leading to lower cloud tops at

higher aerosol levels, as the enhanced evaporation near cloud top dries the cloud. This response has been shown in large-eddy simulations (Chen et al., 2011).

There might be other causes of the negative response between cloud top and AI. In regions off the coast of South Africa, layers of absorbing aerosol are commonly present. Aerosol over cloud tops increases the stability thereby inhibiting the cloud tops to grow (Wilcox et al., 2010). In our analysis, an aerosol layer (detected by CALIPSO) located above the cloud tops has been excluded, and thus it is less likely to be the cause of lower cloud tops. Nevertheless, more detailed studies are needed to understand the cloud top height response.

In the global map of fitting slope between cloud optical depth (τ) and $\log_{10}$(AI) (Fig. 4.2D), the tendency is also somewhat noisy, and overall it demonstrates a similar response as that of the LWP-AI relationship. Positive slope between τ and AI occurs in most regions, showing the clouds get brighter with enhanced aerosol. In regions dominated with MSc, near neutral to negative response of τ to AI is shown (light red to blue color). This indicates that the LWP and cloud top height response plays a significant role in affecting τ, even though in these regions the negative Re-AI response acts to enhance τ. Besides, in areas where R_e increases with AI (red regions as shown in Fig. 4.2A), the τ-AI relationship is diminished into neutral to negative response. As the slope of Re-AI and LWP-AI are largely determined by the environmental conditions, the response of τ-AI is as well influenced by the thermodynamic states, especially the free tropospheric humidity and lower tropospheric stability. Similar pattern is shown for the cloudy sky albedo response to AI. Further detailed investigation on meteorology will be carried out in Section 4.4.3.

4.4.3 Aerosol-cloud responses under different environmental regimes

As both LTS and RH_{ft}, controlled by large scale subsidence, play significant roles in affecting the cloud responses to aerosol, we separate the dataset into different environmental regimes using LTS and RH_{ft}. The data are binned into different meteorological conditions. The slopes of the linear fit between cloud properties and $\log_{10}$(AI) are calculated with 95% confidence level and the outliers of cloud properties have been removed from the analysis. Note that only non-precipitating clouds are included in the analysis to avoid complicacy in data interpretation, as the precipitating clouds have different reactions with non-precipitating clouds. It is worth mentioning that attempts have also been made to bin the data based on varied sea surface temperature, wind speed, etc. However there

is no clear discrepancy in aerosol-cloud interactions using these parameters. Therefore in the following analysis we focus on the effect of LTS and RH_{ft}.

For the non-precipitating clouds, the slope between LWP and AI is larger toward moist free troposphere and higher stability (Fig. 4.4A), showing that the entrainment effect does not result in cloud water loss under this environment, and therefore the LWP enhances with AI. On the other hand, under dry and unstable condition, the LWP decreases with AI as the entrainment and evaporation dominate the cloud water budget and lead to cloud water loss (e.g., Ackerman et al., 2004; Chen et al., 2011). In the regime with dry free troposphere and high stability, where stratiform clouds are prevalent, overall the LWP increase slightly with AI. The two environmental features in this regime, high LTS and low RH_{ft}, act to compete with each other on cloud water budget, as low RH_{ft} tends to cause negative LWP-AI response through entrainment effect yet high LTS favors positive LWP response.

Overall, it is shown that the co-variability of LTS and RH_{ft}, which are controlled by the large-scale subsidence, buffers the LWP responses to increasing aerosols, as suggested by Stevens and Feingold (2009) that aerosol-cloud response can be buffered by the environment and precipitation.

Based on the environmental separation, the response of cloud optical depth to AI is overall positive under all regimes, but with different strength (Fig. 4.4B). The linear fit between τ and AI is larger under moist free troposphere and lower stability, where the environmental conditions favor more convective-like clouds. And under dry and unstable condition, τ increases the least with AI, as the negative LWP response (Fig. 4.4B) buffers the aerosol-cloud response. Overall, the cloud optical depth enhances more under moist free troposphere.

As the precipitating clouds have different aerosol-cloud responses compared to non-precipitating clouds, the sensitivities of warm cloud properties to AI are separated into precipitating (note that drizzling clouds are also included in Fig. 4.5) and non-precipitating clouds, as well as four environmental regimes (based on free tropospheric humidity and stability). The overall aerosol-cloud responses are illustrated in Fig. 4.5 and are consistent with previous analysis.

The negative relationship between R_e and AI is shown in all conditions (Fig. 4.5A), and the sensitivity is larger for non-precipitating clouds, consistent with that in Table 4.3. Besides, R_e is more sensitive under unstable environments. The sensitivity of LWP-AI relationship is much higher

for precipitating clouds (Fig. 4.5B), as the precipitation suppression leads to LWP enhancement under higher aerosol level (except for dry/stable condition). For non-precipitating clouds, LWP increases more under wet/unstable conditions and decreases under dry/unstable conditions, as entrainment drying dominates the cloud water response.

Similar trend has been shown in τ-AI and A_{CLD} -AI response. As a brief overview, the sensitivity of τ and cloudy sky albedo to increased AI is positive for all regimes, and precipitating clouds have higher albedo susceptibility than non-raining clouds, showing that the LWP enhancement due to precipitation suppression acts to increase τ and A_{CLD}. Also, under moist/unstable environmental regime which favors stronger convection, τ and A_{CLD} increase more with aerosol a feature that is predominant throughout most of the tropics (see Fig. 4.2D). On the other hand, under dry/stable environment which is dominated by MSc, τ-AI and A_{CLD} -AI relationship are weaker.

The relative change in LWP versus change in R_e, in short, determines the cloud albedo susceptibility (i.e., change in A_{cld} with AI). Fig. 4.4 illustrates the cloud albedo susceptibility versus the LWP response (based on the 4°×4° grid). When LWP changes with increasing AI, the variation in LWP governs the sign and magnitude of the cloud albedo susceptibility. With enhanced LWP, the cloud albedo increases with AI (i.e., lifetime effect (Albrecht 1989)); by contrast, with significant decreases in LWP, the LWP reduction can completely cancel the Twomey effect and lead to lower cloud albedo. This effect is seen in some ship track observations (Chen et al., 2012). About 17% of the data analyzed here reveal a negative LWP response and corresponding negative albedo response. This indicates that the LWP response dominates the cloud albedo susceptibility, as now robustly demonstrated from ship tracks (smaller scale) to global marine warm cloud (large scale) observations.

4.5 Aerosol Indirect Radiative Forcing

4.5.1 Equations for intrinsic and extrinsic aerosol indirect effects

To estimate the indirect radiative effect at the top of the atmosphere (TOA), we quantify the sensitivity of the cloud radiative forcing, a measure of the effect of clouds on the reflected solar flux relative to the clear sky flux to change in AI. The formal definition of cloud radiative forcing from the top of the atmosphere (TOA) can be written as

$$C_{SW,LW} = F_{CLR} - F_{OBS} \tag{4.1}$$

where SW/LW represent the shortwave/longwave component, F_{CLR} is clear sky net radiative flux (i.e., $F_{CLR} = F_{CLR}^{\uparrow} - F_{CLR}^{\downarrow}$ for atmospheric columns containing no clouds, where $F_{CLR}^{\uparrow}$ is the TOA upward radiative flux, and $F_{CLR}^{\downarrow}$ is the TOA downward radiative flux), and F_{OBS} is the TOA net flux that is observed for all sky conditions (excluding ice clouds in this study). F_{OBS} can be decomposed into

$$F_{OBS} = (1 - c_f)F_{CLR} + c_f F_{CLD} \tag{4.2}$$

where, c_f is the cloud cover fraction over the CERES sensor footprint and F_{CLD} is the component of the radiative flux contributed by clouds. Note that this simple form ignores the surface contribution when cloud coverage is equal to 1. This is generally not true for thin clouds, but is a safe assumption over the ocean where the surface albedo is generally quite small (typically less than 0.15). F_{CLD} can be calculated using equation (4.2). Equations (4.1) and (4.2) can be combined to yield the following

$$C_{SW,LW} = c_f(F_{CLR} - F_{CLD}) \tag{4.3}$$

where the derivative of the shortwave (SW) component of the TOA cloud radiative forcing can be written as

$$\frac{dC_{SW}}{d\ln(AI)} = \left[\overline{c_f}\left(\frac{dA_{CLR}}{d\ln(AI)} - \frac{dA_{CLD}}{d\ln(AI)}\right) + \overline{(A_{CLR} - A_{CLD})}\frac{dc_f}{d\ln(AI)}\right]\overline{F}^{\downarrow} \tag{4.4}$$

where the first term represents the *intrinsic* (non-cloud cover effects) aerosol indirect effect and the second term is the extrinsic (cloud cover effects) indirect effect.

To determine the aerosol indirect radiative effect, we take the derived estimation from (4.4) and multiply it by the aerosol increase caused by anthropogenic activities, $\Delta a = \left[\log(AOD) - \log(AOD - AOD_{anth})\right] = \log\left(\frac{1}{1 - A_{frc}}\right)$, where A_{frc} is the anthropogenic fraction of aerosol in an optical depth retrieval.

4.5.2 Estimation of anthropogenic aerosol fraction

The anthropogenic aerosol fraction is estimated using two different methods. One is obtained from GEMS aerosol mass fraction of sulfate and black carbon (Fig. 4.3B). The GEMS global mean A_{frc} is 21%, consistent with the estimation using MODIS data by Kaufman et al. (2005), which shows 21 ± 7% of the AOD over the oceans has an anthropogenic origin. Another estimation is from the 'aerosol fine mode fraction' (FMF) retrieved from MODIS, defined as the ratio of small mode optical depth to the total AOD at 0.55 μm. Based on the assumption that 21 ± 7% of AOD has anthropogenic source, it is derived that anthropogenic aerosols are associated with FMF larger than 0.69±0.05. And the anthropogenic aerosol fraction in each grid is defined as the ratio of pixel number with FMF > 0.69.

CALIPSO was also examined based on aerosol species identification. Yet it is not included here since the contribution from polluted dust inexplicably resulted in unrealistically large anthropogenic aerosol fractions in the Southern Hemisphere. This suggests that improvements are needed in aerosol species identification in current CALIPSO algorithms.

4.5.3 Aerosol indirect radiative forcing estimation using the dataset

Using Equation (4.4) and estimated A_{frc} from GEMS and MODIS, the AIE radiative forcing is estimated using 4°×4° grid size. On a global average (60°S - 60°N), the estimated intrinsic AIE for oceanic warm clouds is -0.49 W m^{-2} and -0.37 W m^{-2} for GEMS and MODIS A_{frc}, respectively. The magnitudes are comparable to the first indirect effect estimation -0.42 Wm^{-2} by Lebsock et al. (2008, also on oceanic warm clouds). Based on Quaas et al. (2009), the cloud albedo effect estimation is -0.2 Wm^{-2} over oceans (for all type of clouds).

For the extrinsic (cloud-cover effect) indirect effect, the estimation is -1.53 Wm^{-2} (GEMS A_{frc}) and -1.45 Wm^{-2} (MODIS A_{frc}), more than three times higher than the estimated intrinsic AIE. It should be noticed that the observed positive relationship between cloud cover and aerosol may be caused by other processes or artifacts. Several potential mechanisms which may be relevant to the positive c_f-AI relationship have been discussed in previous studies (e.g., Quaas et al., 2010; Grandey et al., 2013), including regional scales larger than 4°×4°, cloud contamination of satellite-retrieved AOD,

covariation of cloud fraction and relative humidity, other meteorological factors, cloud processing of aerosols, etc. Since the focus of this study is not untangling the strong positive cf-AI response using satellite, further detailed analysis is out of the scope of this study. However, the magnitude of the extrinsic (cloud cover) indirect effect is likely to be over exaggerated and should not be viewed as the absolute bound.

The longwave (LW) component of TOA cloud radiative forcing can be written similarly as:

$$\frac{dC_{LW}}{d\ln(AI)} = \left[\overline{c_f} \left(\frac{dF_{CLR}}{d\ln(AI)} - \frac{dF_{CLD}}{d\ln(AI)} \right) + \overline{(F_{CLR} - F_{CLD})} \frac{dc_f}{d\ln(AI)} \right] \quad (4.5)$$

Using GEMS A_{frc}, the estimated longwave component of aerosol indirect radiative forcing is -0.018 W m^{-2} for intrinsic AIE, and 0.08 for extrinsic AIE (see Table 4.4 for the estimation using MODIS A_{frc}). Though the magnitude of extrinsic AIE may not reflect the real aerosol-cloud relationship, the total LW aerosol indirect forcing is slightly positive (0.062 W m^{-2}), showing the LW AIE is a warming effect to the climate as these clouds trap more LW radiation. However, the magnitude is smaller compared to SW AIE, and thus the LW aerosol indirect effect does not contribute significantly to the total effect.

The previous analysis focused on the aerosol indirect forcing for the TOA. At the surface, direct measurements cannot be acquired from space and radiative fluxes can only be determined through a radiative transfer scheme. Fluxes are provided in both CERES and FLXHR-LIDAR product from CloudSat data processing center. Due to larger biases in the SW radiation between these products (Henderson et al. 2013), only the surface LW aerosol indirect forcing is evaluated using equation 4.5. With fluxes from FLXHR-LIDAR, the surface LW component is -0.04 Wm^{-2} for intrinsic AIE, and 0.24 Wm^{-2} for extrinsic AIE (GEMS A_{frc}). As a whole, it indicates LW leads to warming effect at the surface.

4.6 Conclusion

The interactions among aerosol, cloud, precipitation, and environmental conditions are complex and intertwined with each other. In this study, the detailed analysis on the relationship between cloud properties and aerosol index has been carried out, with a focus on the differences between

precipitating/non-precipitating clouds as well as cloud responses under varied meteorological conditions. The up-to-dated A-Train satellite data for more than 40 months are utilized to analyze the aerosol indirect effects. It is shown that the precipitating clouds have higher cloud albedo susceptibility as LWP enhances more with suppressed precipitation under higher aerosol level. In contrast, non-precipitating clouds experience cloud water loss as aerosol enhances the entrainment drying.

The unprecedented available satellite capabilities unravel the buffering processes inherent in the aerosol-cloud system. The thermodynamic conditions, LTS and RH_{ft}, act to buffer the LWP responses through precipitation and entrainment, governing the sign and strength of the cloud albedo susceptibility.

The Earth's climate sensitivity is inferred from the observed global temperature increase and the estimated net positive radiative forcing. Greenhouse gas forcing is well constrained, so the uncertainty in net global radiative forcing is attributable to aerosols; the larger present-day aerosol cooling is, the larger is the Earth's climate sensitivity that is consistent with the observed global temperature change. In the face of relentless future increase in greenhouse gas emissions and approximately steady aerosol levels, the unavoidable question is–just how warm will the planet become?

4.7 Bibliography

Ackerman, A. S., Kirkpatrick, M. P., Stevens, D. E., and Toon, O. B.: The impact of humidity above stratiform clouds on indirect aerosol climate forcing, Nature, 432, 1014-1017, 2004.

Albrecht, B.: Aerosols, cloud microphysics, and fractional cloudiness, Science, 245, 1227-1230, 1989.

Bellouin, N., Boucher, O., Haywood, J., and Reddy, M. S.: Global estimate of aerosol direct radiative forcing from satellite measurements, Nature, 438, 1138–1141, 2005.

Chen, Y.-C., Xue, L., Lebo, Z. J., Wang, H., Rasmussen, R. M., and Seinfeld, J. H.: A comprehensive numerical study of aerosol-cloud-precipitation interactions in marine stratocumulus, Atmos. Chem. Phys., 11, 9749–9769, doi:10.5194/acp-11-9749-2011, 2011.

Chen, Y.-C., Christensen, M. W., Xue, L., Sorooshian, A., Stephens, G. L., Rasmussen, R. M., and Seinfeld, J. H.: Occurrence of lower cloud albedo in ship tracks, Atmos. Chem. Phys., 12, 8223–8235, doi:10.5194/acp-12-8223-2012, 2012

Christensen, M. W. and Stephens, G. L.: Microphysical and macrophysical responses of marine stratocumulus polluted by underlying ships: Evidence of cloud deepening, J. Geophys. Res., 116, D03201, doi:10.1029/2010JD014638, 2011.

Christensen, M. W. and Stephens, G. L.: Microphysical and macrophysical responses of marine stratocumulus polluted by underlying ships. Part 2: Impacts of haze on precipitating clouds, J. Geophys. Res., 117, D11203, doi:10.1029/2011JD017125, 2012.

Christensen, M. W., G. Carrio, G. Stephens, W. Cotton, Radiative impact of cirrus on the properties of marine stratocumulus, J. Atmos. Sci, (in press), 2013.

Coakley, J. A. Jr., M. A. Friedman, and W. R. Tahnk: Retrievals of cloud properties for partly cloudy imager pixels. J. Atmos. Oceanic Technol., 22, 3–17, 2005.

Grandey, B. S., Stier, P., and Wagner, T. M.: Investigating relationships between aerosol optical depth and cloud fraction using satellite, aerosol reanalysis and general circulation model data, Atmos. Chem. Phys., 13, 3177-3184, doi:10.5194/acp-13-3177-2013, 2013.

Hartmann, D. L., Ockert-Bell, M. E. and Michelsen, M. L.: The effect of cloud type on earth's energy balance—Global analysis. J. Climate, 5, 1281–1304, 1992.

Haynes, J. M., T. S. L'Ecuyer, G. L. Stephens, S. D. Miller, C. Mitrescu, N. B. Wood, and S. Tanelli: Rainfall retrieval over the ocean with spaceborne W-band radar. J. Geophys. Res., 114, D00A22, doi:10.1029/2008JD009973, 2009.

Henderson, David S., Tristan L'Ecuyer, Graeme Stephens, Phil Partain, Miho Sekiguchi, 2013: A multisensor perspective on the radiative impacts of clouds and aerosols. J. Appl. Meteor. Climatol., 52, 853–871, doi: http://dx.doi.org/10.1175/JAMC-D-12-025.1, 2013.

IPCC: Summary for policymakers, in: Climate Change 2007: The Physical Science Basis, Contribution of Working Group I to the Fourth Assessment Report of the Intergovernmental Panel on Climate Change, edited by: Solomon, S., Qin, D., Manning, M., Chen, Z., Marquis, M., Averyt, K. B., Tignor, M., and Miller, H. L., Cambridge University Press, 2007.

Kato, S., and coauthors : Relation of cloud occurrence frequency, overlap, and effective thickness derived from CALIPSO and CloudSat merged cloud vertical profiles. J. Geophys. Res., 115, D00H28, doi:10.1029/2009JD012234, 2010.

Kaufman, Y. J., Koren, I., Remer, L., Rosenfeld, D., and Rudich, I.: The effect of smoke, dust, and pollution aerosol on shallow cloud development over the Atlantic Ocean, P. Natl. Acad. Sci., 102, 11207–11212, 2005.

Latham, J., Rasch, P., Chen, C.-C., Kettles, L., Gadian, A., Gettelman, A., Morrison, H., Bower, K., and Choularton, T.: Global temperature stabilization via controlled albedo enhancement of low-level maritime clouds, Philos. Trans. Roy. Soc. London, 366, 3969-3987, doi:10.1098/rsta.2008.0137, 2008.

Lebsock, M. D., Stephens, G. L., and Kummerow, C.: Multisensor satellite observations of aerosol effects on warm clouds, J. Geophys. Res., 113, doi:10.1029/2008JD009876, d15205, 2008.

Mangold, A., De Backer, H., De Paepe, B., Dewitte, S., Chiapello, I., Derimian, Y., Kacenelenbogen, M., Leon, J.-F., Huneeus, N., Schulz, M., Ceburnis, D., O'Dowd, C., Flentje, H., Kinne, S., Benedetti, A., Morcrette, J.-J., Boucher, O.: Aerosol analysis and forecast in the European Centre for Medium-Range Weather Forecasts Integrated Forecast System: 3. Evaluation by means of case studies, J. Geophys. Res., 116, D03302, doi:10.1029/2010JD014864, 2011.

Matsui, T., Masunaga, H., Kreidenweis, S. M., Pielke Sr., R. A., Tao, W.-K., Chin, M., and Kaufman, Y. J.: Satellite-based assessment of marine low cloud variability associated with aerosol, atmospheric stability, and the diurnal cycle, J. Geophys. Res., 111, D17204, doi:10.1029/2005JD006097, 2006.

Penner, J. E., Xu, L., and Wang, M.: Satellite methods underestimate indirect climate forcing by aerosols, P. Natl. Acad. Sci., 108, 13404–13408, doi/10.1073/pnas.1018526108, 2011.

Quaas, J., Ming, Y., Menon, S., Takemura, T., Wang, M., Penner, J. E., Gettelman, A., Lohmann, U., Bellouin, N., Boucher, O., Sayer, A. M., Thomas, G. E., McComiskey, A., Feingold, G., Hoose, C., Kristjansson, J. E., Liu, X., Balkanski, Y., Donner, L. J., Ginoux, P. A., Stier, P., Grandey, B., Feichter, J., Sednev, I., Bauer, S. E., Koch, D., Grainger, R. G., Kirkevag, A., Iversen, T., Seland, Ø., Easter, R., Ghan, S. J., Rasch, P. J., Morrison, H., Lamarque, J.-F., Iacono, M. J., Kinne, S., and Schulz, M.: Aerosol indirect effects general circulation model intercomparison and evaluation with satellite data, Atmos. Chem. Phys., 9, 8697–8717, 2009.

Remer, L. A., Kaufman, Y. J., Tanr´e, D., Mattoo, S., Chu, D. A., Martins, J. V., Li, R. R., Ichoku, C., Levy, R. C., Kleidman, R. G., Eck, T. F., Vermote, E., and Holben, B. N.: The MODIS algorithm, products, and validation, J. Atmos. Sci., 62, 947–973, doi:10.1175/JAS3385.1, 2005.

Sekiguchi, M., Nakajima, T., Suzuki, K., Kawamoto, K., Higurashi, A., Rosenfeld, D., Sano, I., and Mukai, S.: A study of the direct and indirect effects of aerosols using global satellite data sets of aerosol and cloud parameters, J. Geophys. Res., 108(D22), 4699, doi:10.1029/2002JD003359, 2003.

Stevens, B. and Brenguier, J.-L.: Cloud controlling factors: low clouds. Clouds in the perturbed climate system, Heintzenberg, J. and Charlson, R. J., The MIT Press, Cambridge, Massachusetts, 173-196, 2009.

Storelvmo, T., Kristj´ansson, J. E., Myhre, G., Johnsrud, M., and Stordal, F.: Combined observational and modeling based study of the aerosol indirect effect, Atmos. Chem. Phys., 6, 3583–3601, 2006.

Wentz, F. J. and R. W. Spencer: SSMI rain retrievals within a unified all-weather ocean algorithm. J. Atmos. Sci., 55, 1613-1627, 1998.

Wilcox, E. M.: Stratocumulus cloud thickening beneath layers of absorbing smoke aerosol. Atmos. Chem. Phys., 10, 11769–11777, doi:10.5194/acp-10-11769-2010, 2010.

Wood, R.: Cancellation of aerosol indirect effects in marine stratocumulus through cloud thinning, J. Atmos. Sci., 64, 2657-2669, 2007.

Yuan T., Li, Z., Zhang, R., and Fan, J.: Increase of cloud droplet size with aerosol optical depth: an observational and modeling study, J. Geophys. Res., 113, D04201, doi:10.1029/2007JD008632, 2008.

Table 4.1 Sensors and corresponding parameters used in the analysis, along with the spatial resolution. All sensors were matched to the nearest CloudSat footprint.

Sensor	Parameter	Spatial Resolution
CloudSat	Precipitation flag	1.4 × 2.5 km
MODIS	3.7μm cloud effective radius, cloud optical depth Cloud top pressure/ temperature Aerosol index, aerosol fine mode fraction, cloud fraction	1 × 1 km 5 × 5 km 1° × 1°
CALIPSO	Cloud top height, cloud layer flag, aerosol top/base heights	5 × 5 km (30 m vertically)
ECMWF	Pressure, temperature, humidity, SST, surface wind speed	2.5° × 2.5°
GEMS	Aerosol species, AOD	120 × 120 km
CERES	Clear/cloudy sky albedo, cloud fraction, cold/warm cloud number	20 × 20 km
AMSR-E	Cloud liquid water path, column water vapor	13 km / 21 km
NCEP	Omega	2.5° × 2.5°

Table 4.2 Screening procedures and resultant data reductions

Criteria	Percent
Warm ocean clouds (MODIS cloud top pressure/temperature), valid MODIS cloud parameter (R_e, $\tau > 0$), and valid CERES radiation	100%
Above and single cloud layer (CALIPSO)	69.1%
Above and CERES criteria for no cold cloud and $c_f > 0$	49.5%
Above and valid aerosol index (AI)	28.4%
Above and valid derived CERES cloudy sky albedo	20.5% (~3.7 million)

Table 4.3 Slope of linear fit between cloud properties and $\log_{10}$(AI), for non-precipitating, drizzling, and precipitating clouds.

	R_e [micron]	LWP [g m^{-2}] (AMSR-E)	LWP [g m^{-2}] (MODIS)	H [m]	τ	A_{CLD}
Non-precipitating	-2.83	-3.34	6.08	-185.2	2.57	0.057
Drizzling	-1.03	2.84	30.08	-163.8	4.60	0.072
Precipitating	-1.39	17.49	20.96	40.0	4.81	0.084

Table 4.4 The estimated aerosol indirect radiative forcing using Eq. (4.4) and (4.5) for shortwave (SW) and longwave (LW) component, respectively. The anthropogenic aerosol fraction (A_{frc}) is estimated using GEMS and MODIS. (TOA stands for 'top of atmosphere'.)

	Intrinsic AIE (W m^{-2})		Extrinsic AIE (W m^{-2})	
	GEMS A_{frc}	MODIS A_{frc}	GEMS A_{frc}	MODIS A_{frc}
SW TOA	-0.49	-0.37	-1.53	-1.45
LW TOA	-0.018	-0.026	0.081	0.079
LW surface	-0.04	-0.04	0.24	0.26

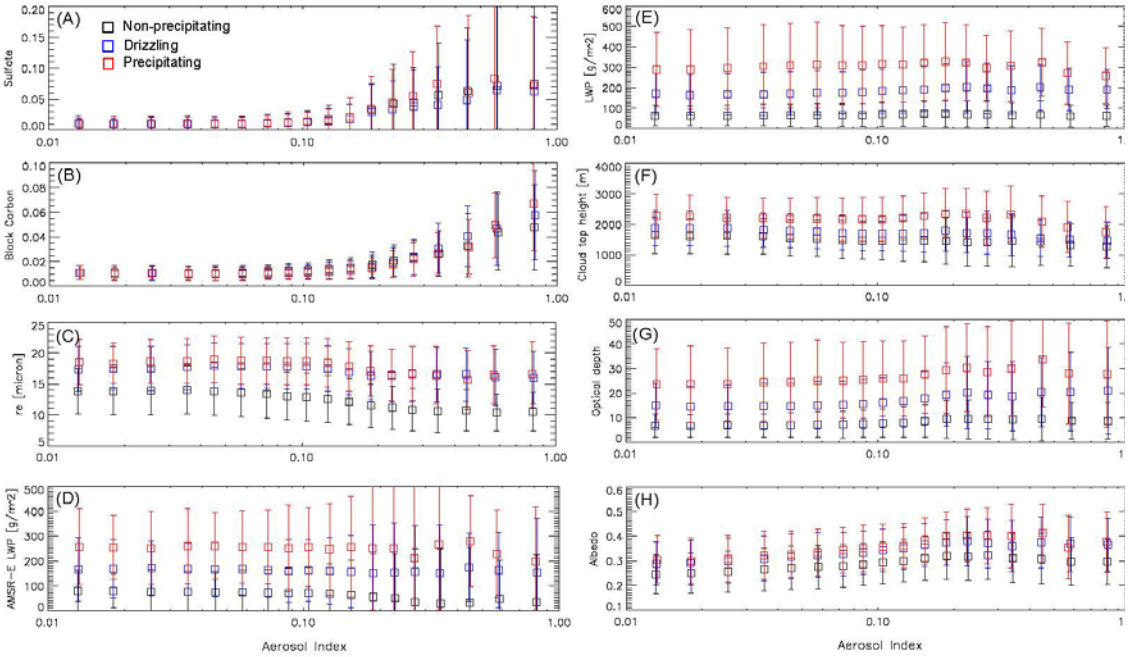

Figure 4.1 Global relationships between AI and aerosol/cloud parameters for non-precipitating, drizzling, and precipitating clouds. Squares represent the mean values and error bars show the standard deviation.

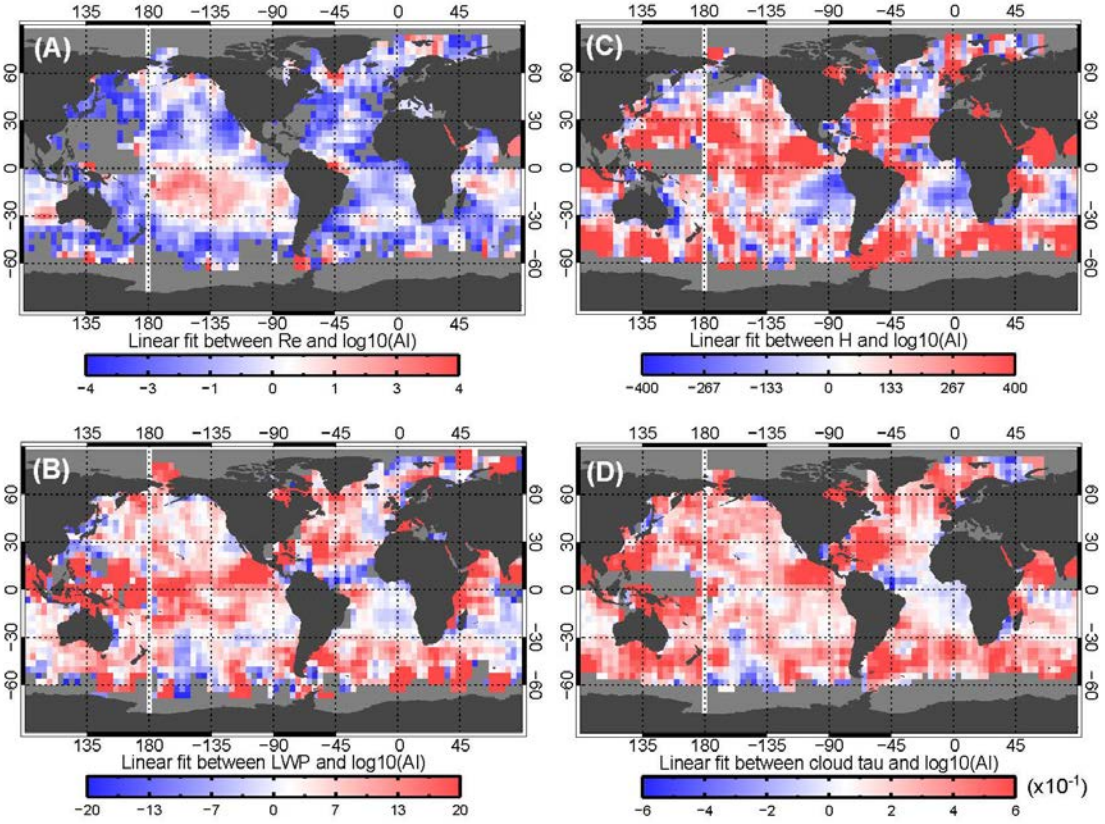

Figure 4.2 Distribution of the least square fitting slope between cloud parameters and $\log_{10}$(AI) with 4°×4° gridded regions. The cloud parameters are: (A) Cloud effective radius, (B) LWP, (C) Cloud thickness, and (D) cloud optical depth.

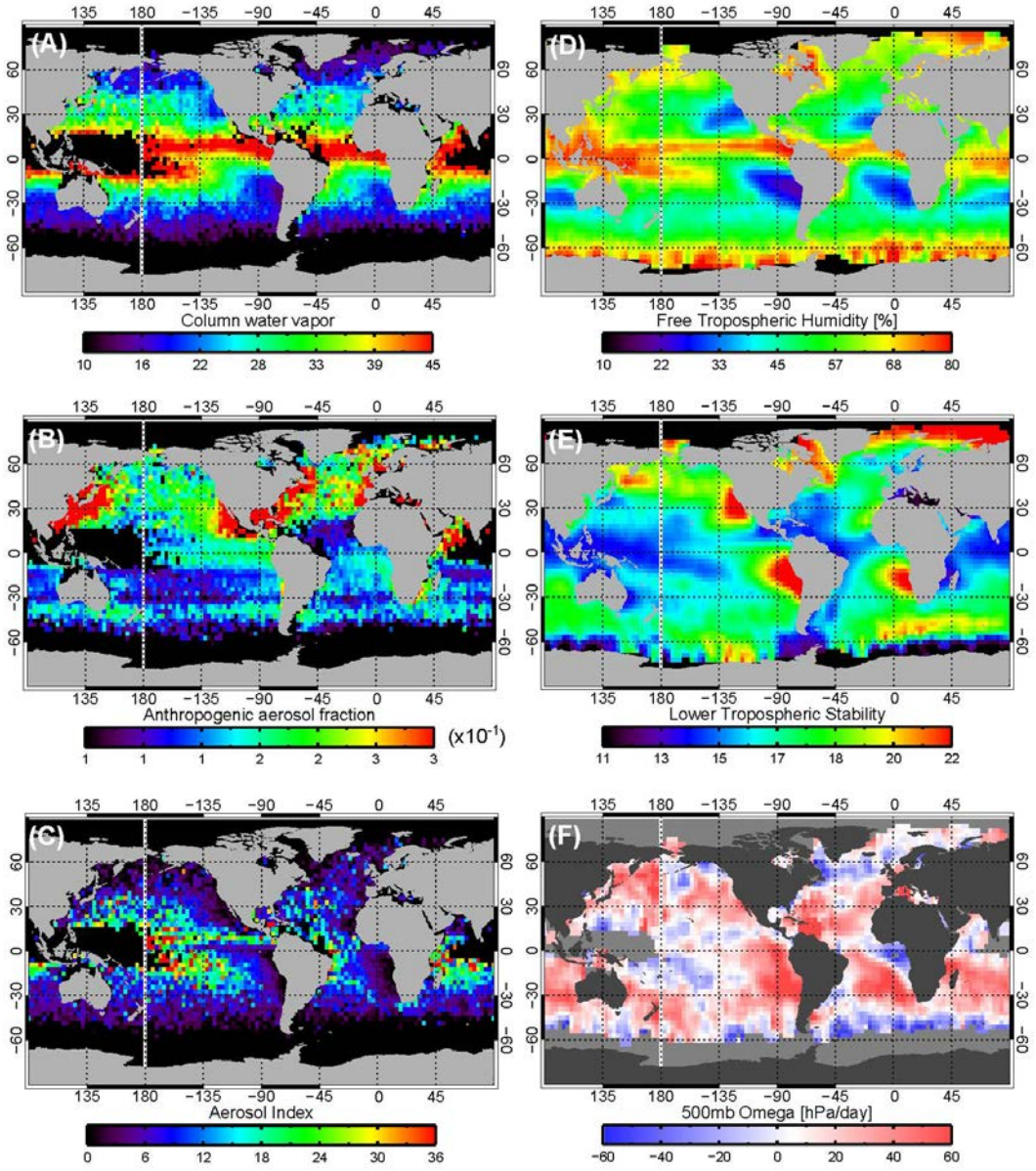

Figure 4.3 Distribution of environmental conditions and GEMS anthropogenic aerosol fraction. The environmental variables include: (A) AMSR-E column water vapor, (C) Probability of precipitation, (D) Free tropospheric humidity, (E) Lower tropospheric stability, and (F) 500 mb vertical velocity (represented as omega). GEMS anthropogenic aerosol fraction is shown in (B).

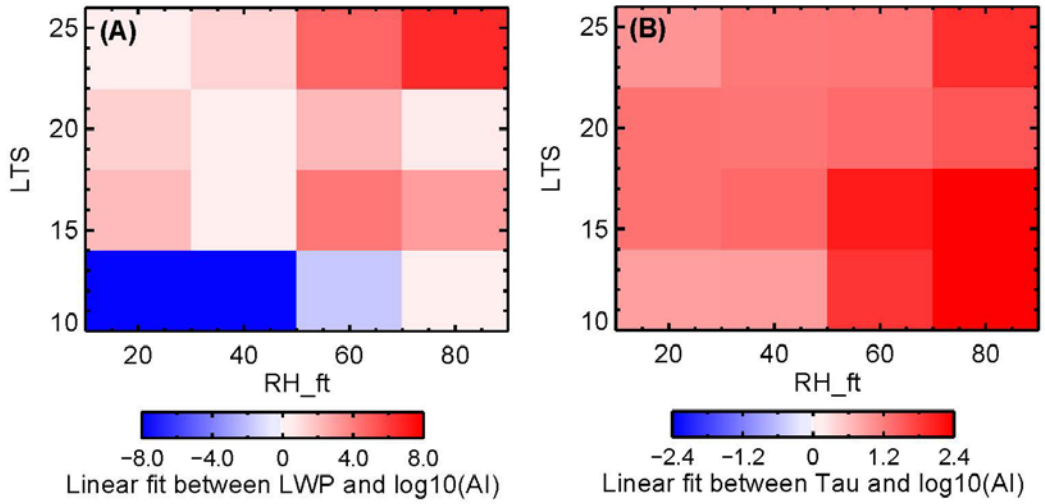

Figure 4.4 Slope of (A) LWP versus $\log_{10}$(AI) and (B) Cloud optical depth (τ) versus $\log_{10}$(AI) under different environmental conditions for non-precipitating clouds. The x-/y-axis correspond to different free tropospheric relative humidity/lower tropospheric stability, respectively. Each colored pixel represents the slope that is statistically significant at the 95% confidence interval.

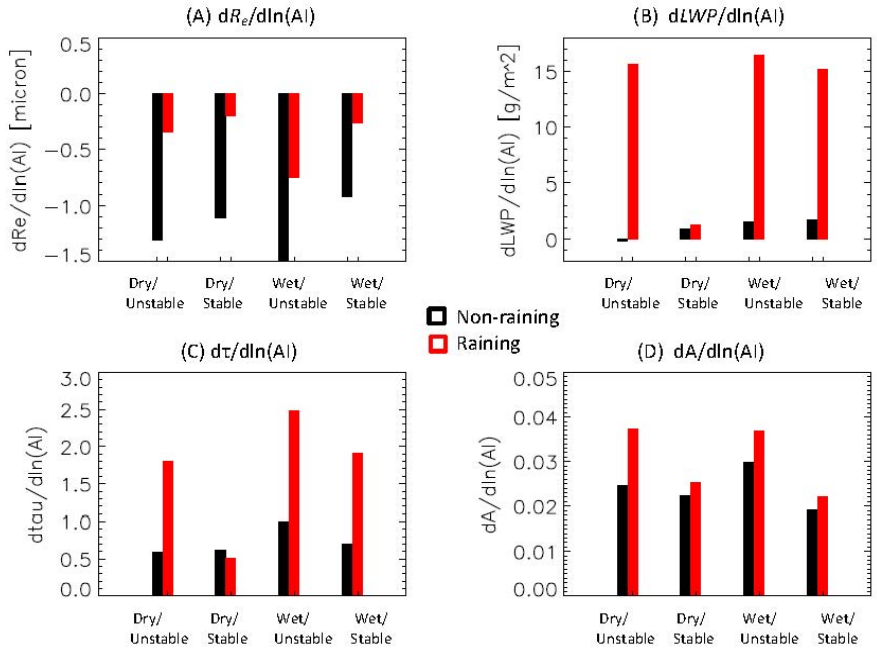

Figure 4.5 Slope of (A) R_e versus $\log_{10}$(AI), (B) LWP versus $\log_{10}$(AI), (C) Cloud optical depth versus $\log_{10}$(AI), and (D) Cloud albedo versus $\log_{10}$(AI), under different environmental conditions for precipitating (red) and non-precipitating clouds (black).

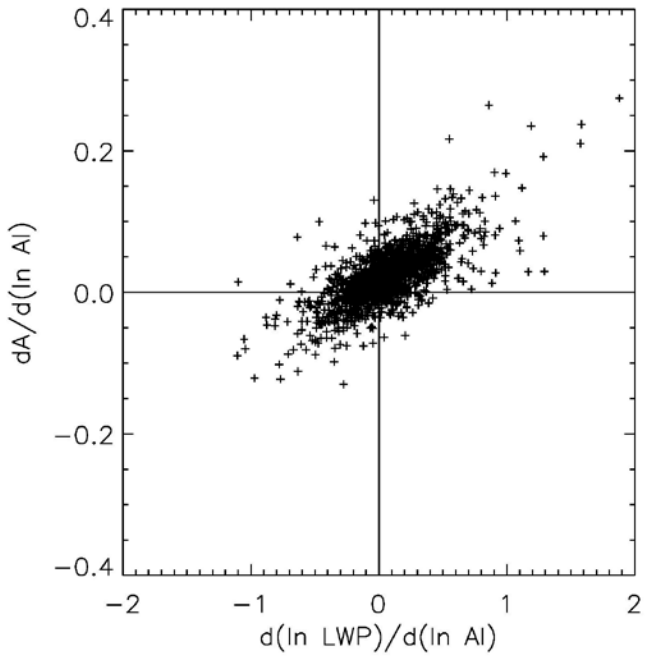

Figure 4.6 Cloud albedo susceptibility (i.e., change in cloud albedo to change in logarithm AI) versus LWP susceptibility. Each data point corresponds to each 4°×4° gridded region.